



**HAL**  
open science

# Microfluidic fabrication of metamaterials out of colloidal dispersions

Sara de Cicco

► **To cite this version:**

Sara de Cicco. Microfluidic fabrication of metamaterials out of colloidal dispersions. Other. Université de Bordeaux, 2020. English. NNT : 2020BORD0050 . tel-03001087

**HAL Id: tel-03001087**

**<https://theses.hal.science/tel-03001087>**

Submitted on 12 Nov 2020

**HAL** is a multi-disciplinary open access archive for the deposit and dissemination of scientific research documents, whether they are published or not. The documents may come from teaching and research institutions in France or abroad, or from public or private research centers.

L'archive ouverte pluridisciplinaire **HAL**, est destinée au dépôt et à la diffusion de documents scientifiques de niveau recherche, publiés ou non, émanant des établissements d'enseignement et de recherche français ou étrangers, des laboratoires publics ou privés.

THÈSE PRÉSENTÉ POUR OBTENIR LE GRADE DE  
**DOCTEUR DE L'UNIVERSITÉ DE BORDEAUX**

ÉCOLE DOCTORALE DES SCIENCES CHIMIQUES

Spécialité : PHYSICO-CHIMIE DE LA MATIÈRE CONDENSÉE

Par Sara De Cicco

---

**Microfluidic fabrication of metamaterials  
out of colloidal dispersions**

---

Sous la direction de Jacques Leng et Jean-Baptiste Salmon  
Soutenue le 15 juin 2020

**Membres du jury :**

Virginie Ponsinet	Président du jury	Chercheur	CRPP, Bordeaux
Pierre Joseph	Rapporteur	Chargé de recherche	LAAS, Toulouse
Michele Giocondo	Rapporteur	Chercheur	LiCryL, Rende
Brigitte Pansu	Examineur	Professeur	LPS, Orsay
Jacques Leng	Examineur	Chargé de recherche	LOF, Bordeaux
Jean-Baptiste Salmon	Examineur	Directeur de recherche	LOF, Bordeaux



# Table of Contents

<b>Abstract</b> .....	<b>x</b>
<b>Résumé</b> .....	<b>xi</b>
<b>Introduction</b> .....	<b>13</b>
<b>Chapter 1 – Self-assembled metamaterials</b> .....	<b>15</b>
1.1 Metamaterials.....	15
1.2 Fabrication of metamaterials .....	17
1.2.1 Bottom-up approach.....	21
1.3 Assembly.....	22
1.3.2 Template assembly .....	25
1.3.3 Sedimentation and filtration .....	26
1.3.5 Evaporation .....	27
1.3.5 Layer by layer deposition .....	28
1.3.6 Microfluidic self-assembly.....	29
<b>Chapter 2 – Materials and methods</b> .....	<b>31</b>
2.1 Introduction .....	31
2.2 Experimental challenges .....	31
2.2.1 Stability and Sedimentation .....	32
2.2.2 Pervaporation.....	32
2.2.2.1 Induced flow.....	34
2.2.2.2 Colloidal concentration .....	36
2.2.3 Microevaporators geometries .....	39
2.3.4 Chip 1: Membrane microevaporator .....	40
2.3.5 Chip 2: Unidirectional evaporator.....	41
2.3.6 Chip 3: Decoupled microevaporator .....	42
2.4 Nanoparticles .....	43
2.4.1 Silicon nanoparticles .....	43
2.4.2 N-podes .....	44
2.4.2.1 Hexapodes.....	44
2.4.2.2 Dodecapodes.....	45

2.4.3 Latex .....	46
2.7 Microfabrication techniques.....	47
2.7.1- Mask design .....	47
2.7.2- SU8 lithography.....	48
2.8 PDMS molding.....	49
2.8.1 Chip 1: Membrane microevaporator .....	50
2.8.2 Chip 2: unidirectional evaporator .....	51
2.8.3 Chip 3: decoupled microevaporator .....	52
<b>Chapter 3 – Material assembling.....</b>	<b>54</b>
3.1 Introduction .....	54
3.2 Silicon small scale assembly .....	54
3.2 Unidirectional evaporator.....	58
3.2.1 Holes evaporator.....	58
3.2.1.1 Material characterization.....	59
3.2.2 Multichannel evaporator .....	61
3.3 Chip 3: Decoupled microevaporator .....	64
3.3.1 Characterization .....	68
3.3.1.1 Silicon dense material .....	69
3.3.1.2 Optical microscopy and SEM.....	73
3.3.3 Large scale N-podes .....	74
3.3.3.1 Profilometry, SEM .....	76
3.4 Infiltration .....	80
3.4.1 PVA .....	82
3.4.2 PVP .....	85
3.6 Reproduction of the decoupled system.....	90
3.5.1 Latex infiltration with PEG-DA.....	92
3.5.1.1 Latex dense material .....	92
3.5.1.2 Latex infiltrated with PEG-DA.....	93
3.5.1.3 Latex infiltrated with PEG-DA+In .....	94
3.5.3 Silica infiltration .....	96
3.5.4 Silicon infiltration .....	98

3.5.5 Decapodes infiltration..... 100

**Bibliography ..... 106**



# Table of figures

Figure 1 Examples of different metamaterials: 1) Ultrasonic metamaterials [15] 2) Thermal metamaterials [16] 3) Mechanical metamaterials [17] , 4) optical metamaterials and 5) application of the latter for cloaking [18, 19].	15
Figure 2 Illustration of the electromagnetic metamaterials classified on $\epsilon$ and $\mu$ values [21]	17
Figure 3 a) Double split-ring resonator as a building block in metamaterials at microwave frequencies; b) schematic circuit of a split-ring resonator.	18
Figure 4 Part of the left-handed metamaterial array configuration, which was constructed of copper split-ring resonators SRRs and wires mounted on interlocking sheets of fiberglass circuit board. The total array consists of 3 by 20 by 20 unit cells with overall dimension [21]	19
Figure 5 a) Raspberries synthesis; b) microfluidic assembly; c) 3D metamaterial [24]	20
Figure 6 Schematic representation of top-down and bottom-up methods [27]	21
Figure 7 X-Ray top-down fabrication (left) and nanowires fabricated via bottom-up method (right) [28]	22
Figure 8 How to assemble nanoparticles	23
Figure 9 Self-assembly of lipids (a), proteins (b), and (c) SDS-cyclodextrin complexes. SDS is a surfactant with a hydrocarbon tail (yellow) and a SO <sub>4</sub> head (blue and red), while cyclodextrin is a saccharide ring (green C and red O atoms) [31]	24
Figure 10 Colloidal phase diagram in function of the particles volume fraction ( $\phi$ ) [33]	24
Figure 11 Template self-assembly schematization; a) resin deposition on a substrate; b) template fabrication by lithography; c) particles assembly; d) template removal; e) final dense material	25
Figure 12 Schematic sedimentation process.	26
If the particles are large, the sedimentation is faster than the crystal formation rate and often leads at a poor periodicity in the crystal lattice organization. On the other hand, slow sedimentation to a better crystallinity [34]. Pusey <i>et al.</i> [35] have used sedimentation of colloids to obtain a crystal structure from hard colloidal spheres ( <b>Error! Reference source not found.</b> 13). The Final result was a mostly face centered cubic crystals after sedimentation over several months.	26
Figure 14 Silica crystal formation by sedimentation process [35].	26
Figure 15 Schematization of the filtration process in presence of different particle sizes	27
<b>Figure 16 Solvent evaporation process for particles assembly</b>	27
Figure 17 SEM images of a single layer obtain by vertical deposition with an oven-setup (A). Different arrangements cubes: a square-like (B) and a hexagonal-like (C) [37]	28
<b>Figure 18 layer by layer deposition via solvent evaporation</b> [38]	28
Figure 19 Schematic view of “microfluidic self-assembly” of nanoparticles to obtain dense 3D materials.	29
Figure 20 specifications and general sketch of this thesis work	31
Figure 21 illustration of the pervaporation process of a solvent through a dense membrane. The solvent 1) solubilizes inside the membrane, 2) diffuses across the membrane, 3) evaporates in contact with air. ....	33
Figure 22 Representation of the pervaporation flow across a PDMS membrane of thickness $e$ . The membrane divides a pure water solution from a three different cases of humidity air.	33
Figure 23 Microfluidic membrane device in PDMS. The red arrows show the side of the pervaporation	

process [47]..... 35

Figure 24 a) microevaporator side view, made by a single channel with height $h$ and width $w$ , sealed by a PDMS membrane and deposited on a glass slide. Evaporation length is defined by $L_0$ , where the water pervaporates through the membrane with a velocity $V_e$ ; b) velocity flow profile along the microfluidic channel; c) water flow crossing the microevaporation section at the $x$ position. ....	35
Figure 25 Representation of the balance between convection and diffusion. The red line represents the convective contribution, which it is the velocity profile of the pervaporation- induced flow and the blue line represents the solute concentration profile resulting from a balance between convection and diffusion [47] .....	37
Figure 26 pervaporation influenced by the dense state. a) the colloidal assembly doesn't influence at all the pervaporation; b) polymer dense state influence the pervaporation process [48].....	38
Figure 27 a) colloidal assembly along a single channel in time; b) front displacement of particles covered with a polymer; c) front displacement of particles covered with silica [48] .....	39
Figure 28 Membrane microchannel. a) Side view of the microfluidic channel; b) top view of the microfluidic channel; c) nanoparticle assembly process driven by the pervaporation-induced flow across the membrane. ....	40
Figure 29 Unidirectional evaporator: a) Side view of the microfluidic channel; b) top view of the microfluidic channel; c) nanoparticle assembly process starting from the only opened point of the channel. ....	41
Figure 30 Decoupled microevaporator: a) Side view of the microfluidic channel; b) top view of the microfluidic channel; c) in red filter assembly process and in green assembly of the particles of interest. ....	42
Figure 31 Silicon nanoparticles TEM images (left), silicon nanoparticles dispersed in water (right). Images V. Ponsinet, P Barois and A. Baron from CRPP .....	43
Figure 32 Schematization of the thin oxidation layer formation in time (left); HRTEM image of three different SiNP surface modification (right) [49]. ....	44
Figure 33 synthesis schematization for the nanoparticles with patches [50] .....	45
Figure 34 Hexapode nanoparticles TEM images (left), hexapodes nanoparticles dispersed in water (right) [50] .....	45
Figure 35 Synthesis schematization for the nanoparticles with patches [50].....	46
Figure 36 Dodecapodes nanoparticles TEM images (left), dodecapodes nanoparticles dispersed in water (right) [50] .....	46
Figure 37 Designs developed during the thesis; 1) membrane microevaporator; 2) unidirection evaporator; 3) decoupled microevaporator .....	47
Figure 38 Schematic representation of the fabrication steps of a mold .....	48
Figure 39 final molds obtained after the lithography process; a) chip 1: membrane microdevice; b) chip 2: unidirectional evaporator; c) chip 3: decoupled microevaporator. ....	49
Figure 40 Fabrication protocol of the "Membrane microevaporator" .....	51
Figure 41 unidirectional evaporator fabrication steps. ....	52
Figure 42 decoupled microevaporator fabrication steps. ....	53
Figure 43 3D Membrane microevaporator Chip 1 (top); channel perspective view of the microevaporation during the accumulation of colloids (bottom). ....	54

Figure 44 Capture of a single channel during the assembling process in different time after the injection of the silicon nanoparticles. The channel becomes darker in time which is due to the concentration of particles during their assembly. ....	56
Figure 45 SEM images of the silicon dense material after the recovering from the PDMS device.....	57
Figure 46 3D unidirectional evaporator device .....	58
Figure 47 Capture of the channel during the evaporation process and the silicon nanoparticles assembly. The front between the liquid and crystal phase is sharp (in black the dense phase in gray the liquid phase; scale bar 100 $\mu\text{m}$ ).....	59
Figure 48 Optical profilometry acquisition of the silicon assembled material.....	59
Figure 49 Height profile (left) and 3D topography image of the dense material .....	60
Figure 50 Ellipsometry results. Transmittance (left); Reflectance (right).....	60
Figure 51 frame capture of the material front direction (scale bar 300 $\mu\text{m}$ ).....	61
Figure 52 optical profilometry. A)top view of the final material; b) 3D structure of the material; c) height profile .....	62
Figure 53 ellipsometry measurements, on the left the transmittance values in function of the wavelength; on the right the reflectance values obtain in function of the wavelength at different angle degrees. ....	63
Figure 54 Total Absorbance in function of the wavelength for the silicon multi-channels and holes dense materials .....	63
Figure 55 On the top the microfluidic device used for the nanoparticles assembling with the two different zones (pump and assembling chamber); above the schematic side view of the decoupled microdevice....	64
Figure 56 working setup; on left a photo of all the instruments used during the experiments with the chip3; on the right a zoom of the tubing connection between the chip3 and the pressure controller.....	66
Figure 57 Capture of the channel during the evaporation process and the latex nanoparticles assembly. The front (green lines) between the liquid and crystal phase is sharp (in black the liquid phase in gray the solid phase). Scale bar 500 $\mu\text{m}$ .....	67
Figure 58 Capture of the channel during the silicon nanoparticles assembly. The red line shows the front between the liquid and dense phase inside the channel.....	68
Figure 59 Material recover after the assembled process (left); optical microscopy acquisition of the material after it has been recovered full of cracks appears during the drying step. ....	69
Figure 60 Profilometry acquisition.....	70
Figure 61 SEM images of the PDMS mold cross section. ....	71
Figure 62 ellipsometry characterization. ....	72
Figure 63 Images acquired by optical microscope .....	73
Figure 64 SEM images at different magnifications.....	74
Figure 65 images acquired during the hexapodes particles assembly. The grey zone (left) next to the black front is the latex particle filter already assembled. The green line shows the particles growth front during the pervaporation process inside the microfluidic channel.....	75
Figure 66 Images of the dense material a) inside the microchannel after the assembly and the drying step; b) final material recovered after the PDMS block removing. After the recovery material many failure appears in the material bulk (scale bar 500 $\mu\text{m}$ ). ....	76
Figure 67 Profilometry acquisition. a) Real image of the dense material; b) height acquisition and c) 3D representation on a portion of the material.....	77

Figure 68 SEM images acquired for the hexapode dense material.....	78
Figure 69 Acquisition of a single channel captured during the assembling process. With the red line it is define the front between the solid phase and the liquid phase .....	79
Figure 70 SEM images of the dodecapodes dense material after been recovered .....	80
Figure 71 3D reproduction of the membrane microevaporator (top); channel side view of the microevaporation during the pervaporation (bottom).....	81
Figure 72 sketch of the assembly phase of the latex nanoparticles and the later step of polymer infiltration .....	82
Figure 73 Single channel zoomed in to follow the particles assembly and the infiltration process (scale bar 100 $\mu\text{m}$ ) .....	83
Figure 74 Images acquired at the end of the experiments. All the channels are filled with the latex assembled particles (in white) and infiltrated with the PVA solution.....	84
Figure 75 SEM images of the channels cross section. ....	85
Figure 76 sketch of the assembling and infiltration process inside the microchannel .....	86
Figure 77 Single channel zoomed in to follow the particles assembly and the infiltration process (scale bar 100 $\mu\text{m}$ ). ....	87
Figure 78 Capture of the endo of the infiltration experiment. The white part is the latex material assembled and the dark part represents the filling of the channels by PVP.....	88
Figure 79 SEM imagies acquired for each channel after the cross section ofthe microdevice. ....	88
Figure 80 Capture of the latex assembly and the PEG-DA infiltration through the latex lattice. The blue circle shows the moment when the PEG-DA enters the microchannel. ....	89
Figure 81(a) diagram of the decoupled microevaporator functioning; (b) single channel magnified and observed during the formation of the latex filter in black and white the dense material composed of silica nanoparticles. Over time the channel changes its refractive index after being infiltrated with the polymer solution (bottom). Scale bar 100 $\mu\text{m}$ . ....	90
Figure 82 Single channel during the assembling process. Filter growth to form the pumping zone, silicon nanoparticles assembly and PVP infiltration trough the dense material. The infiltration is visible by the refractive index changing .....	91
Figure 83 SEM images of the latex dense material at the end of the assembling process.....	93
Figure 84 SEM images of the latex dense material infiltrated with the pure PEG-DA.....	94
Figure 85 SEM images of the latex dense material infiltrate with PEG-DA+HMP and reticulated .....	95
Figure 86 SEM images of the pure PEG-DA+HMP reticulated.....	96
Figure 87 Silica dense material infiltrated with PAG-DA+HMP1% before (top) and after (bottom) the photopolymerization. The red line indicates the front between the latex dense material and the silica dense material. ....	97
Figure 88 SEM images of the dense material. a) silica nanoparticles covered with the PEG-DA reticulated; b) latex nanoparticles covered with the PEG-DA reticulated; c) PEG-DA reticulated .....	98
Figure 89 Silicon dense material recovered after been infiltrate with PEG-DA+HMP1%and reticulated....	99
Figure 90 Optical profilometry acquisition. The height profilometry scan of a dense silicon material section (left); image acquired by optical profilometry (right) .....	99
Figure 91 SEM images of the infiltrated silicon dense material after the photopolymerization process ...	100
Figure 92 four different moments of the infiltration process after the dodecapodes assembling.....	101

Figure 93 Images captured before and after the reticulation by the UV light (scale bar 500 $\mu\text{m}$ ).....	102
Figure 94 SEM images of the infiltrated dense dodecapodes dense material. ....	103

## Abstract

In the last decades, the scientific community focused its attention on the study of new materials, referred to as metamaterials, displaying unusual features, making for instance possible the control of the effective optical refractive index and thus foreseeing extraordinary optical applications such as perfect lenses or cloaking.

Bottom-up approaches making use of self-assembly of resonant nanoparticles (meta-atoms) of sub-wavelength size into close-packed materials offer many interesting opportunities. In the present work, we report on the bottom-up fabrication of materials starting from dilute colloidal dispersions using a microfluidic technique referred to as *microfluidic pervaporation*. This original technique makes use of water pervaporation through dense poly-dimethylsiloxane membranes to concentrate dilute colloidal dispersions up to the formation and growth of close-packed colloidal structures in well-defined microfluidic channels. Previous works proved the successful fabrication, using this technique, of a metamaterial exhibiting a strong isotropic artificial optical magnetism at visible light frequencies, starting from dispersions of raspberry-like resonant nanoparticles. In the present work, we extend this microfluidic technique to the fabrication of large-scale thick metamaterials, with typical dimensions 5 mm x 3 mm x 30  $\mu\text{m}$ , for further optical characterization by using standard ellipsometry. We demonstrate the successful fabrication of such large and thick coatings using different kinds of nanoparticles: mono-disperse silica nanospheres, silicon nanoparticles, and custom-made “dodecapodes”. We also improved our microfluidic technique to be able to infiltrate such close-packed colloidal materials using photo-curable polymers to get free-standing and crack-free materials.

**Keywords:** Metamaterials, microfluidic, pervaporation

## Résumé

Dans les dernières décennies, la communauté scientifique a concentré son attention sur l'étude de nouveaux matériaux, appelés métamatériaux, présentant des caractéristiques inhabituelles et permettant par exemple le contrôle de l'indice de réfraction effectif pour des applications optiques extraordinaires telles que les lentilles parfaites ou le camouflage.

Les approches bottom-up utilisant l'auto-assemblage de nanoparticules résonantes de taille inférieure à la longueur d'onde (méta-atomes) offrent de nombreuses possibilités intéressantes. Dans ce travail, nous faisons état de la fabrication de métamatériaux à partir de dispersions colloïdales diluées, en utilisant une technique microfluidique appelée pervaporation microfluidique. Cette technique originale utilise la pervaporation de l'eau à travers des membranes denses en poly-diméthylsiloxane pour concentrer des dispersions colloïdales diluées jusqu'à la formation et la croissance de structures colloïdales très compactes dans des canaux microfluidiques bien définis. Des travaux précédents ont prouvé la fabrication, à l'aide de cette technique, d'un métamatériau présentant un fort magnétisme optique artificiel isotrope aux fréquences de la lumière visible, à partir de dispersions de nanoparticules résonantes de type framboise plasmonique. Dans le présent travail, nous étendons cette technique microfluidique à la fabrication de métamatériaux épais, avec des dimensions typiques de 5 mm x 3 mm x 30  $\mu\text{m}$ , pour une caractérisation optique en utilisant l'ellipsométrie. Nous démontrons la fabrication de matériaux épais en utilisant différents types de nanoparticules : des nanosphères de silice mono-disperses, des nanoparticules de silicium et des "dodécapodes" faits sur mesure. Nous avons également amélioré notre technique microfluidique afin de pouvoir infiltrer des matériaux colloïdaux en utilisant des polymères photodurcissables pour obtenir des matériaux sans fissures.

**Mots-clés** : Métamatériaux, microfluidique, pervaporation



# Introduction

Metamaterials are a particular class of artificial materials capable of showing specific electromagnetic properties that do not exist in nature, such as for instance a negative refractive index. The first theoretical idea about the possibility of obtaining a negative refractive index material was described in 1967 by the physicist Victor Veselago [1]. This theoretical approach was somehow forgotten until physicists found the way around 2000 to fabricate the first material exhibiting a negative refraction index, in the field of microwaves (J. Pendry [2] and D. Smith [3] respectively). This was the beginning of the metamaterial adventure which is still very active: the key point was the introduction of structures much smaller than the wave-length of the excitation (here electromagnetic) and which exhibit resonances at some frequency. A metamaterial is built with a multitude of unitary cells made up of these individual resonating elements, referred to as meta-atoms; each meta-atom must have a size smaller than the wavelength interacting with, a specific shape and geometry (whereas the spatial organization is not of prime importance) in such a way to create unusual macroscopic effects. In the case of an electromagnetic wave, the specific behaviors of the meta-atoms upon the excitation the effect results from a non-usual behavior to the macroscopic permittivity and permeability, the material parameters that affect the propagation of the wave.

In order to achieve the realization of these unusual materials, a project has been realized in collaboration with the various laboratories of the University of Bordeaux. Importantly, the goal is to have a physical-chemistry approach based on soft chemistry and self-assembly, and which is quite different from the hard approaches used most of the time to fabricate metamaterials (e.g., lithography, sputtering, etc.). The project funded by the cluster of excellence AMADEus, which has permitted this multidisciplinary approach, issued from the collaboration between physicists, chemists and chemical engineers. The project foresees the realization of meta-structures using particular meta-atoms synthesized at the ICMCB-*Institut de Chimie de la Matière Condensée de Bordeaux*, the optical characterization at the CRPP-*Centre de Recherche Paul Pascal*, and the final assembly phase of the meta-structures by microfluidics at the LOF-*Laboratoire du Futur*. In this thesis work will be described the method of bottom-up assembly (realization of a dense material through the assembly of individual units) using a microfluidic device.

The thesis is organized as follows:

**Chapter1** is an introductory chapter, where we will present the state of the art in the field of metamaterials and then the state of the art in the self-assembly of colloidal particles.

In **Chapter 2** will be presented the bottom-up microfluidic technique used during this thesis work. It will also present the difficulties and the related solutions encountered using different types of possible meta-atoms and the different micro devices developed to achieve aim the of the project. In **Chapter3**, we will show the results obtained (dense assembled materials and their characterizations)

using the different micro-devices developed during the thesis work. This thesis work attempts to demonstrate that it is possible to fabricate dense materials using different types of nanoparticles using specially developed microfluidic devices to reduce fractures in the final material.

# Chapter 1 – Self-assembled metamaterials

## 1.1 Metamaterials

Over the recent years, the scientific community has focused on the study and the fabrication of artificial materials, which display "unusual" features regarding wave propagation. Those materials are referred to as metamaterials, from the prefix "meta" which means "beyond" from ancient Greek. The extraordinary properties of metamaterials offer different fields of application over the entire frequency range. For instance, acoustic metamaterials could manipulate and control the sonic, ultrasonic and infrasonic wave propagation, in liquids or solid phases [4, 5]. Thermal metamaterials could manipulate the heat flux through materials [6, 7]. Mechanical metamaterials are materials that depend on their structure rather than their composition, and possess a large range and tunable Poisson's ratio [8, 9]. Optical metamaterials [10] could display highly unusual light propagation properties like negative refractive index, with possibly striking applications: perfect lens [11, 12], cloaking [13, 14], etc. A common feature for such materials is the fact that they are composed of sub-units, much smaller than the wavelength considered from a few tens of nm for optical application to a few millimeters for sound propagation. Figure 1 shows some examples of different types of metamaterials.

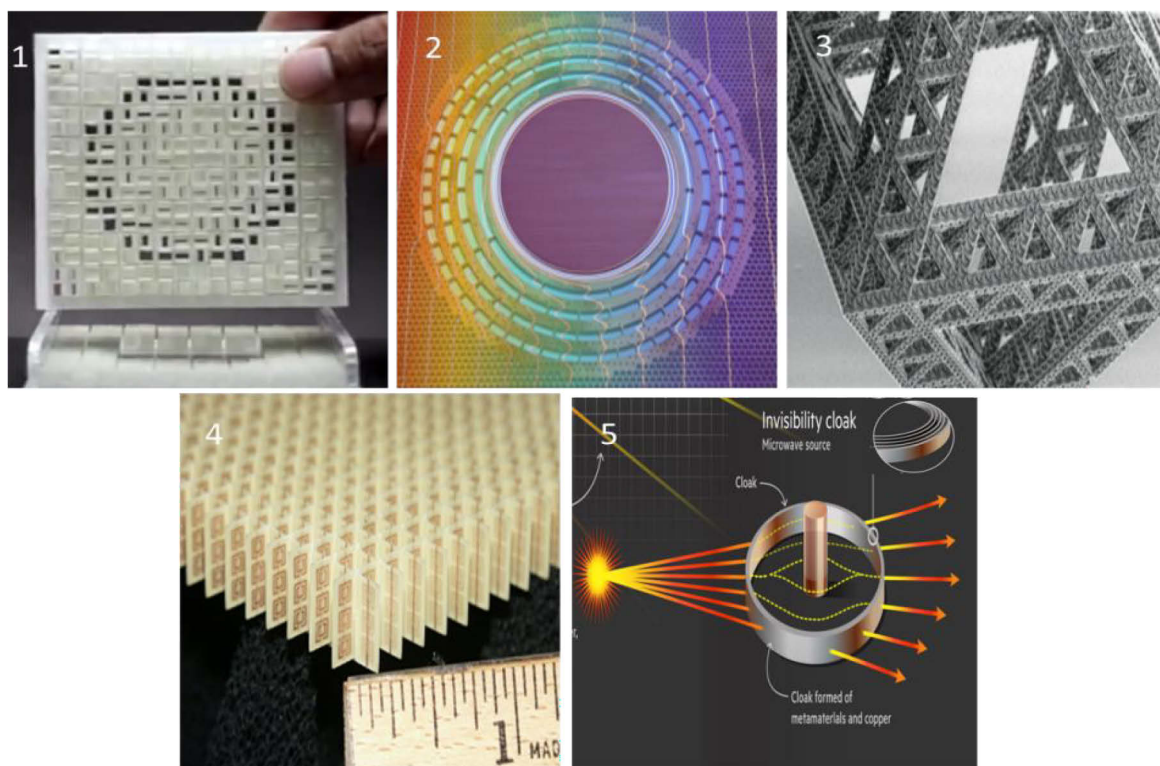


Figure 1 Examples of different metamaterials: 1) Ultrasonic metamaterials [15] 2) Thermal metamaterials [16] 3) Mechanical metamaterials [17] , 4) optical metamaterials and 5) application of the latter for cloaking [18, 19].

In the present work, we will mainly focus on metamaterials for applications in the visible range. For any material, the electromagnetic wave propagation is governed by Maxwell's equations. These equations describe the relationships between fields, sources and material properties, and make use of two parameters which depend on the material properties: the dielectric constant  $\epsilon$  and magnetic constant  $\mu$ . These two parameters ( $\epsilon$  and  $\mu$ ) are essentially “macroscopic” parameters used to describe the average response of a material that interacts with an incident electromagnetic wave.

In the visible range, the wavelength ranges typically from about 380 to 740 nm, and optical metamaterials are expected to be fabricated by nanostructures with sizes ranging from a few nanometers to a few hundred of nanometers. In this way, the electromagnetic wave that propagates through the material sees the structure as a completely homogeneous medium [20]. Optical metamaterials are therefore made up of the arrangement of single elements, with size smaller than the wavelength ( $\lambda$ ), able to modify locally the interaction with light, leading macroscopically to unusual electrical permittivity ( $\epsilon$ ) and magnetic permeability ( $\mu$ ).

Figure 2 classifies materials according to their macroscopic values of  $\epsilon$  and  $\mu$ . In the optical domain, all non-metamaterials are confined along a straight horizontal line with  $\mu_r = 1$  values. Classical materials are confined in the first quadrant for values of  $Re(\epsilon) > 0$  and  $Re(\mu) > 0$  and are for example insulators.

The second and third quadrants admit only values of  $Re(\epsilon) < 0$  and  $Re(\mu) > 0$  or  $Re(\epsilon) > 0$  and  $Re(\mu) < 0$ . For  $Re(\epsilon) < 0$  (II quadrant) most metallic materials at high frequencies are present and they are referred to as “Single Negative Medium (SNG)” or “ $\epsilon - NG$ ”. In the other quadrant (IV quadrant), the materials are “artificial magnetic materials” (AMMs with  $Re(\mu) < 0$ ) and they are called “single negative medium” or  $\mu - NG$ . The last quadrant contains all the materials made by the combination of AMMs and are referred to as “double negative medium” (DNG) or “left-handed materials” and they should be able to show at the same time  $Re(\epsilon) < 0$  and  $Re(\mu) < 0$ .

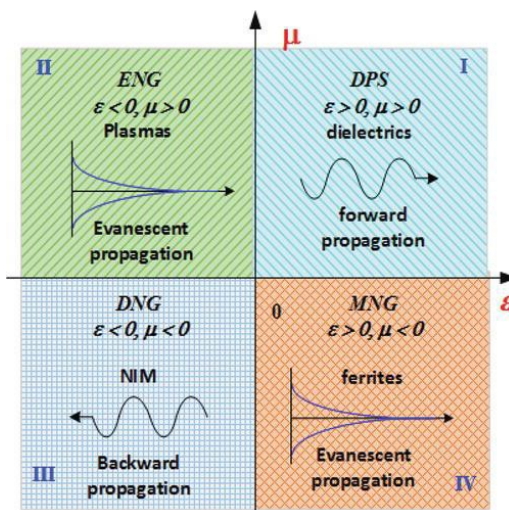


Figure 2 Illustration of the electromagnetic metamaterials classified on  $\epsilon$  and  $\mu$  values [21]

Obtaining unusual properties are possible thanks to specific nano-structures, through which it is possible to modify the macroscopic components properties such as the refraction index ( $n$ ), the permittivity ( $\mu$ ) and the dielectric constant ( $\epsilon$ ) of the macroscopic material. The idea of fabricating a metamaterial is to be able to achieve a negative permittivity ( $\epsilon < 0$ ) and permeability ( $\mu < 0$ ) values or at least it might be possible to even get one of the two parameters different from zero ( $\epsilon \neq 0$  or  $\mu \neq 1$ ).

In 1967, the Russian physicist Veselago published the first paper [1] "*The Electrodynamics of Substances with Simultaneously Negative Values of  $\epsilon$  and  $\mu$* ", where he described the surprising and unusual phenomena that should be observed in a hypothetical left-handed medium, in which the vectors of the electric field ( $E$ ), magnetic field ( $H$ ) and the wave vector ( $k$ ) form a left-handed system. "Left" in this case indicates a material in which the triad formed by the electric field, the magnetic field and the wave vector propagates in the opposite direction to conventional materials.

Veselago used Maxwell's equations to study the behavior of an electromagnetic wave in the presence of materials possessing  $\epsilon$  and negative  $\mu$  and the Snell-Descartes law to demonstrate that it is possible to obtain a material with a negative refractive index.

He also estimated the parameters necessary for obtaining such unusual materials: negative permittivity and permeability values, which would lead to a material with an effective negative refractive index. When  $\epsilon$  and  $\mu$  have negative values, the correct solution of Maxwell's equations requires that the negative value must be chosen as the solution of the square root of the refractive index. So, it leads to:

$$n = -\sqrt{\epsilon\mu} \quad (1)$$

As demonstrated by Veselago, this condition can only be achieved in left-handed materials.

## 1.2 Fabrication of metamaterials

The ideal metamaterial has to be able to modify the phase and amplitude of the incident light.

One of the main feature is the fact that these metamaterials are obtained by the assembly of subunits with sizes smaller than the wavelength. These subunits should have specific interactions with electromagnetic waves. In the field of optical frequencies, different artificial electromagnetic media were studied over the past years, some of them being based on metallic nanostructures.

In the footsteps of Veselago at the end of 1990s, the physicist John Pendry [2] extended Veselago's theory and proposed a theoretical way to obtain a material with  $\mu < 1$ . His idea is to fabricate materials starting from smaller components so-called Split-Ring Resonator (*SRR*), with dimensions smaller than the incident wavelength and composed of a metallic open-ring combined with a metallic wire. With appropriate dimensions, specific material properties, and distance

between the elements, the arrangement of such *SRR* should lead, close a resonant frequency, to a medium that has an effective negative permeability value, associated to the metallic wire medium, and a negative permittivity value at the same time, associated to the open ring.

A schematic Pendry's *SRR* is showed in Figure 3 [22]. Pendry used two open concentric metallic rings (capacitance) to generate a current and had an accumulation of charges across the gap. Introducing an inductance the *SRR* is a resonant element. This resonance happens when the electric dipole moment, generated from the two opposite gaps, tends to cancel each other and the magnetic dipole moment dominates.

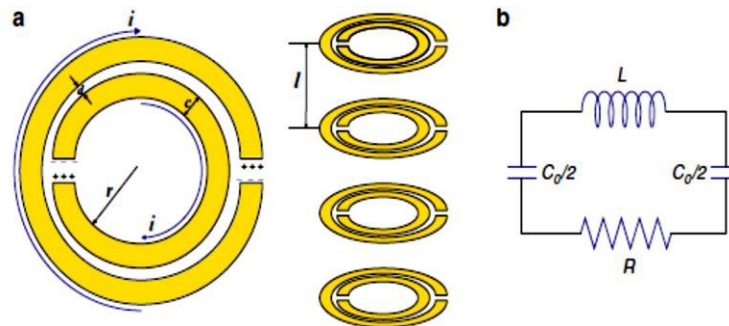
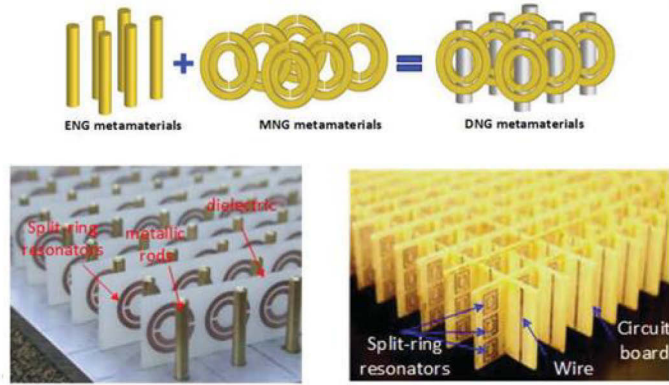


Figure 3 a) Double split-ring resonator as a building block in metamaterials at microwave frequencies; b) schematic circuit of a split-ring resonator.

After almost ten years, based on Pendry's work, Smith *et al.* succeeded in the fabrication of such a double negative metamaterial in the microwave range,  $1\text{ mm}$  to  $1\text{ m}$ . They combined two different materials one of which showed only a negative permittivity and the other only a negative permeability. The system was made of wire/split-rings resonators in series with a millimeter size. They also give demonstration of a negative refracted index in such double negative metamaterials [23].



**Figure 4** Part of the left-handed metamaterial array configuration, which was constructed of copper split-ring resonators *SRRs* and wires mounted on interlocking sheets of fiberglass circuit board. The total array consists of 3 by 20 by 20 unit cells with overall dimension [21]

Pendry's and Smith's works opened the possibility to reproduce the same results but in the visible range. The idea is to combine a structure with  $\epsilon < 0$  with a second one with  $\mu < 0$ , but with reduced sizes of the components, at a sub-wavelength length, typically in the range  $10\text{ nm} - 100\text{ nm}$ . And this is a challenge as we enter the realm of nanotechnology.

Recently, nanoresonators have been considered as good candidates for controlling light, and for many other applications. Nanoresonators are typically nano-structures, for example nanoparticles, thin films, nanofabricated structures, etc., made of specific metallic and dielectric materials, sometimes with a very high dielectric constant.

Coupling the metallic and dielectric properties led to high energy dissipations (losses), possibly reducing the device efficiency. Therefore, the final material cannot have a large thickness in order to avoid massive optical losses, so nowadays researchers are more and more targeting very thin materials, that is *metasurfaces*.

Tailor nanoparticles can support strong electric and magnetic resonances originating from the oscillation of the polarization charge and of the circular displacement current that are excited by the incident light inside the structure. The electromagnetic resonance in this structures can lead to optical magnetism different from 1 ( $\mu \neq 1$ ), negative index ( $\epsilon < 0, \mu < 0$ ) and zero index ( $\epsilon \approx 0, \mu \approx 0$ ) responses.

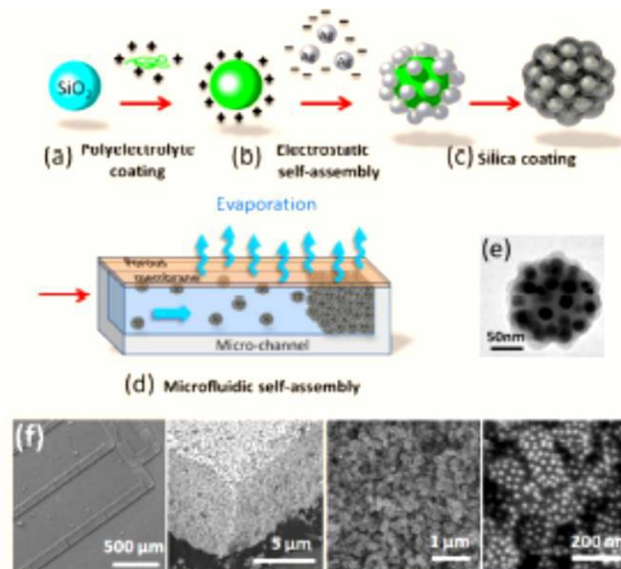


Figure 5 a) Raspberries synthesis; b) microfluidic assembly; c) 3D metamaterial [24]

In 2016 Gomez-Graña *et al.* [24], obtained a strong isotropic optical magnetism response using magnetic nanoclusters of nanoparticles subsequently synthesized and assembled by bottom-up techniques. The magnetic nanocluster referred to as raspberries is made by a dielectric core (silica) covered by many metallic nanosatellites (silver nanoparticles) which behave like in Pendry's SRR. The artificial magnetic response is generated by resonant loops of plasmonic currents induced by the light wave [25]. To be able to reproduce such *SRRs* in the visible range, two steps are important:

- *SRR* fabrication reducing the size to 10 *nm* up to 100 *nm* to be able to work at visible frequencies;
- Assembly the *SRRs* by top down or bottom up approaches. Top-down assembly (e.g. lithography techniques) makes it possible to achieve surface assembly. In bottom-up fabrication it is a priori possible to obtain dense materials starting from powders/solutions/dispersions at different length scales.

Recently, another route based on the interaction between electromagnetic waves and dielectric particles was proposed to achieve the electric or magnetic resonances. The Mie resonances of dielectric inclusions provide a novel mechanism for the creation of magnetic or electric resonance based on displacement currents, and offer a simpler and more versatile route for the fabrication of isotropic metamaterials operating at higher frequencies [24]. Dielectrics particles exhibit electric and magnetic dipole and higher-order multipole Mie resonances.

For dielectric particles, the generation and interference of multipolar modes becomes important, and begins to enable nanoscale manipulation of light and control of the scattering direction. For this kind of particles, the incident light brings both electric and magnetic responses of comparable strengths. The magnetic resonance occurs when the wavelength inside the particle becomes

comparable to its spatial dimension, when  $2R \approx \lambda/n$ . The field enhancement observed during a Mie resonance, is due to the displacement currents induced within the particle by the external electric field, which, in turn, generate an oscillating electromagnetic field inside and outside the particle. In dielectrics, these displacement currents are due to the polarization of the bounded electrons, and are therefore free from ohmic losses, which hamper the scattering efficiency of metals in the optical range.

### 1.2.1 Bottom-up approach

The European Commission defines nanotechnology as: “...the understanding and control of matter at dimensions between approximately 1 and 100 nanometers, where unique phenomena enable novel application. Encompassing nanoscale science, engineering, and technology, nanotechnology involves imaging, measuring, modeling, and manipulating matter at this length scale.” [26].

By reducing sizes down to a few nanometers, chemical-physical properties of materials could differ strongly from those at larger macroscopic scales. For example, chemical reactivity, material strength, and electromagnetic properties can be enhanced.

Over the last decades, the scientific community has been looking for different approaches to reduce material’s scales. Nanostructured materials can generally be fabricated using two different methods. The first one, the *top-down* approach, starts from macroscopic aggregates and proceeds downwards with a reduction in size and subsequent rearrangements. Common techniques for top-down fabrication are lithography techniques, for instance UV lithography, X-Ray lithography, nanolithography, which can reach nano-structures with sizes down to 50 nm.

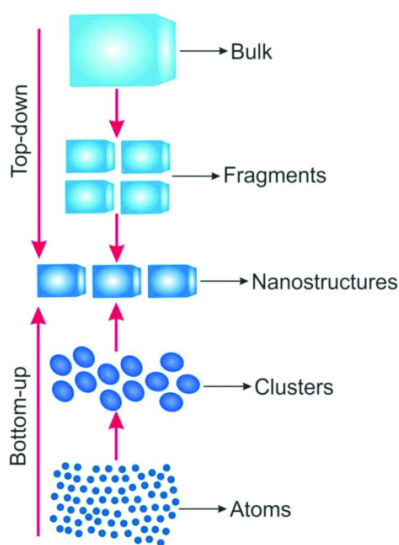


Figure 6 Schematic representation of top-down and bottom-up methods [27]

In the second approach, the so-called *bottom-up* approach, the nano-structured material is built gradually, by assembling individual atoms, molecules, or larger nano-scale clusters (e.g. nanoparticles, micelles, etc.). Bottom-up fabrications are typically based on chemical reactions, atomic manipulations, or any other colloidal interactions. Numerous methods can be associated to the bottom-up approach, like chemical vapor deposition, physical vapor deposition, sol-gel chemistry, etc.

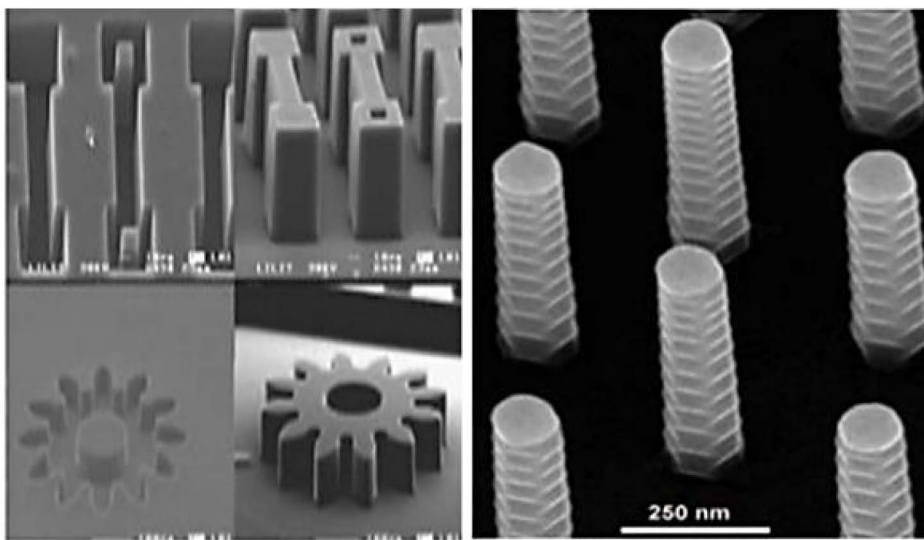


Figure 7 X-Ray top-down fabrication (left) and nanowires fabricated via bottom-up method (right) [28]

The bottom-up technique has been used in this work for the fabrication of complex structures referred to as “metamaterials”, with unusual properties regarding propagation of electromagnetic waves in the visible range. In the following chapter, the main features of such metamaterials, and the possibility of manufacturing them will be discussed.

In the present work, we mainly focus on the fabrication of bulk metamaterials, for the visible light range, starting from dilute dispersion of nanoparticles in a solvent (water, ethanol, etc.) and ending up with a dense solid of nanoparticles; so far, the question of the local organization of nanoresonators is still an open question but in a first approximation, we assume that the final properties of the material result mostly from the ones of the nanoparticles themselves and of course their interaction, but we assume that the local order is not of prime importance. We review in the following paragraph, the different approaches leading to dense materials starting from such dispersion of nanoparticles.

### 1.3 Assembly

In the following, we mainly focus on the fabrication of metamaterials for optical application with wavelengths 380 – 740 *nm* and more precisely bulk metamaterials as opposed to metasurfaces, and so with minimal dimensions 10 – 100 times the size of a nanoparticle, and so 10 – 100 *nm* in

terms of particles diameter size . There are not so many experiments reported so far regarding bulk materials made out of nanoparticles for metamaterial applications. Most works are devoted to metasurfaces, but also top down approaches etc.

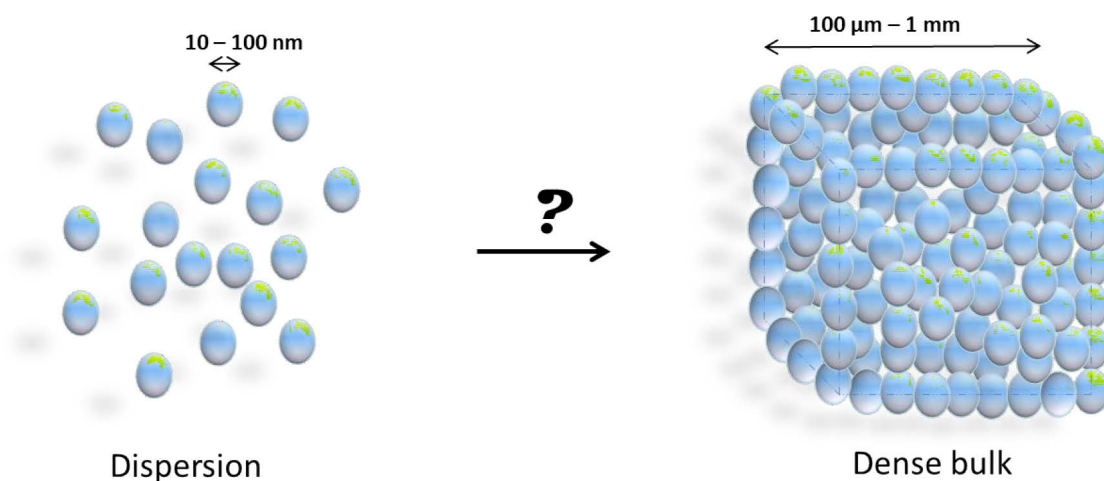


Figure 8 How to assemble nanoparticiles

In the following, I briefly review the commons techniques to assemble nanoparticles, possibly nano-resonators in bulk materials, onto organized or not.

### 1.3.1 Self-assembly

Whitesides *et al.* [29], define self-assembly as a spontaneous and reversible process when a disordered system, in presence of different components, can form ordered structures by non-covalent interactions. Non-covalent interactions refer to weak interactions such as Van der Waals, capillary,  $\pi - \pi$  interactions, electrostatics, etc. He also divided self-assembly in two main categories: dynamic and static self-assembly. In the present PhD work, we will focus our attention on the static self-assembly which mainly refers to the self-assembly used for colloidal dispersions.

An example of self-assembly comes from biology, for example in the formation of protein folding, liposomes, and SDS-cyclodextrin complexes. The formation of these systems depends on the multiple and weak interactions between the molecules. They can form ordered structures at different scales and each of them displays different features [30].

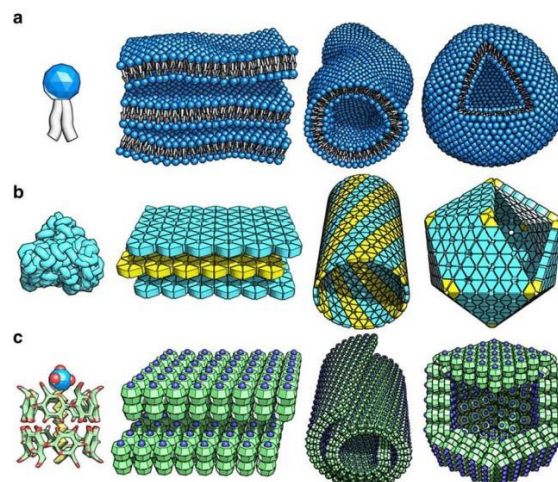


Figure 9 Self-assembly of lipids (a), proteins (b), and (c) SDS-cyclodextrin complexes. SDS is a surfactant with a hydrocarbon tail (yellow) and a  $\text{SO}_4$  head (blue and red), while cyclodextrin is a saccharide ring (green C and red O atoms) [31]

Colloids also self-assemble and may form spontaneously and reversibly, ordered structures. Even for hard-spheres system, defined as impenetrable colloids with no specific interactions, two phases do exist: a fluid phase and a crystal phase as a function of concentration [32]; in this kind of system, the stable phase depends only on the volume fraction of the solid phase. At low volume fraction, particles are in the disorganized state, referred to as the fluid phase. At high volume fraction, particles get organized in a crystal structure, see Figure 10. Fluid and crystal phases can co-exist in a narrow range of concentration.

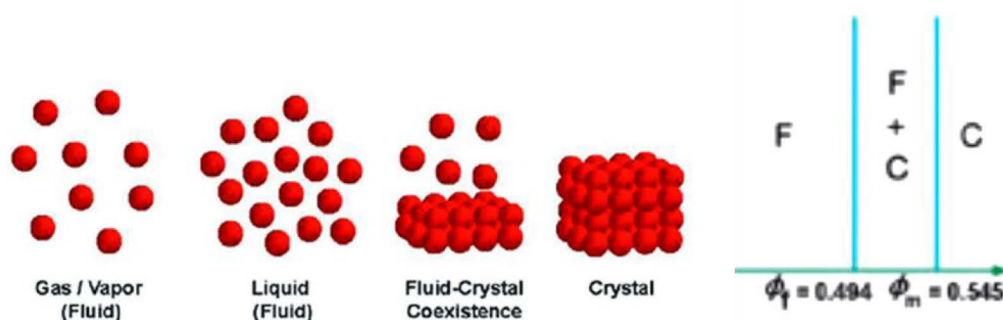


Figure 10 Colloidal phase diagram in function of the particles volume fraction ( $\phi$ ) [33]

In most cases, self-assembly occurs in bulk, leading to organized materials with no defined “shapes”, for example many crystals of colloids floating in a dispersion, etc. “Template” self-assembly combines top-down (lithography) and bottom-up self-assembly (small components 1 nm to 100  $\mu\text{m}$ ) techniques for fabricating materials organized both at the scale of the small components, but also at larger scales.

However, self-assembly in colloidal systems requires: (1) specific interactions between colloids not always applicable for a given particle, (2) narrow range of parameters leading to ordered

materials, (3) complex kinetics for the formation of the self-assembled phases, (4) small size, uncontrolled ordered structures.

One way to overcome the point (4) is template self-assembly. Start by a template, make self-assembly, remove template. It is generally a process that works for dilute systems with specific colloidal interactions. Whereas the self-assembly process does not work easily for systems which have to be very concentrated, up to volume fraction higher than 0.6 (too viscous, or even solid phases, self-assembly is kinetically hindered). One way to overcome those issues is to concentrate the colloids in the dispersion by guiding the assembly process. Common examples of guided assembly are: sedimentation, filtration, evaporation.

### 1.3.2 Template assembly

Template assembly involves four different steps. Deposition of a photo resin on a substrate, creation of a template, by lithography for instance, assembly in the template (e.g. by capillarity or solvent evaporation); and finally, template removal after all the building blocks have been assembled. Template can be removed either mechanically or using organic solvents to dissolve them.

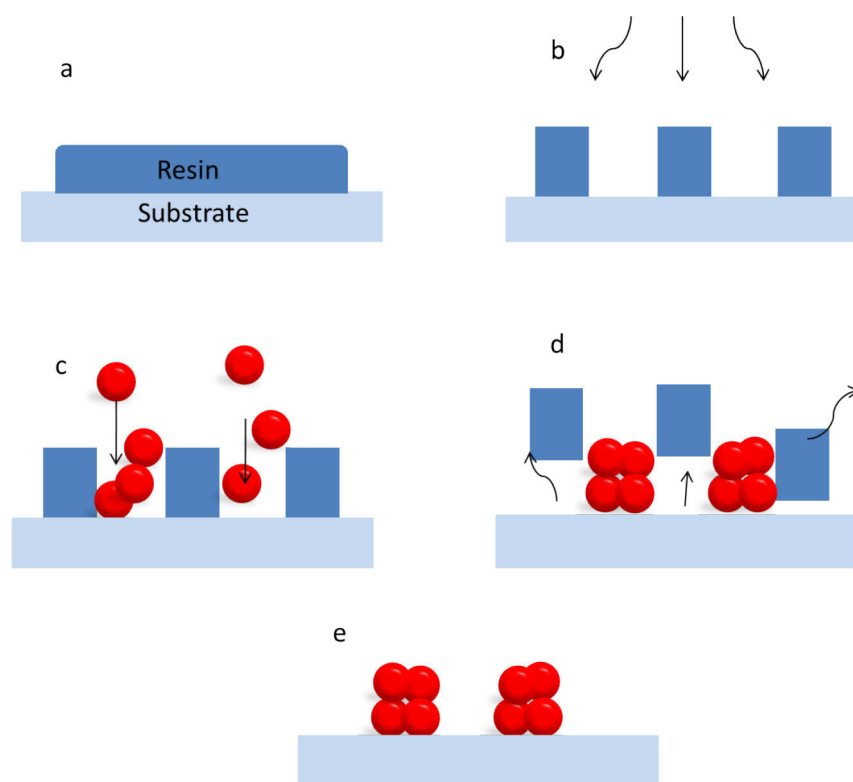


Figure 11 Template self-assembly schematization; a) resin deposition on a substrate; b) template fabrication by lithography; c) particles assembly; d) template removal; e) final dense material

### 1.3.3 Sedimentation and filtration

The sedimentation method consists in dispersing the nanoparticles in a solvent and letting them settle by gravity. The process-time depends on the particle size, on the density difference between the particles and that of the solvent, and on the solvent viscosity.

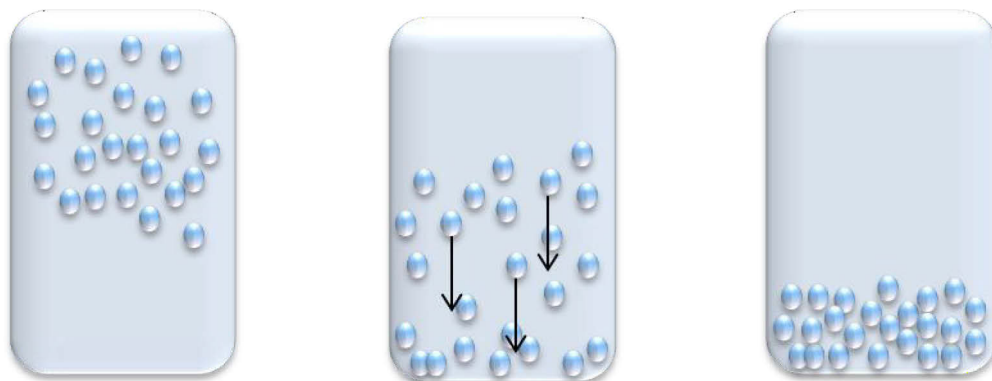


Figure 12 Schematic sedimentation process

If the particles are large, the sedimentation is faster than the crystal formation rate and often leads to a poor periodicity in the crystal lattice organization. On the other hand, slow sedimentation leads to a better crystallinity [34]. Pusey *et al.* [35] have used sedimentation of colloids to obtain a crystal structure from hard colloidal spheres. The final result was a mostly face centered cubic crystal after sedimentation over several months.

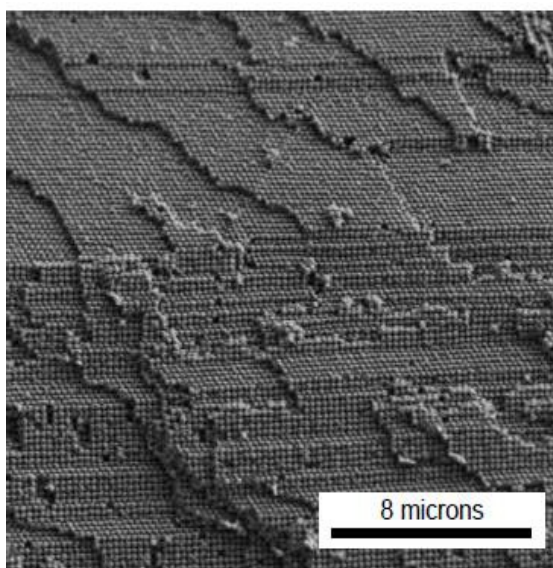


Figure 13 Silica crystal formation by sedimentation process [35]

The filtration process is used for separating suspended particles in a solvent. The suspension is flowed through a membrane. The membrane filter consists of pores that have sizes smaller than that of the particles. The particles cannot pass through the pores, and at the end of the process the residue of the filtration is collected, the so-called filtration cake.

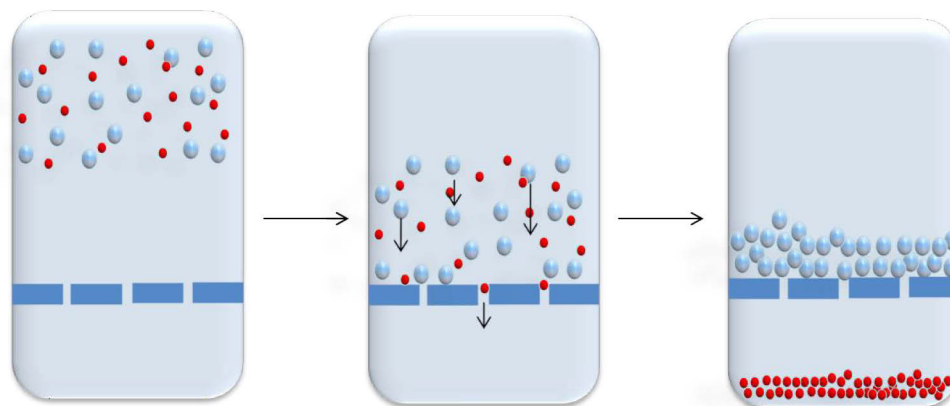


Figure 14 Schematization of the filtration process in presence of different particle sizes

### 1.3.5 Evaporation

Deposition self-assembly is a technique based on the absorption of the particles on a substrate. This process is used for the fabrication of single or multiple layers.

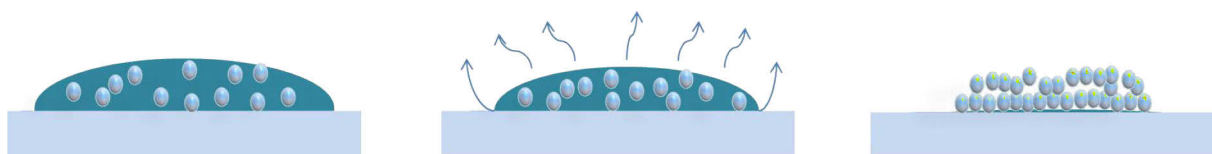


Figure 15 Solvent evaporation process for particles assembly

One of the most used techniques in the particles assembly is the evaporation of the solvent. Solvent evaporation is widely used in assembled structures formation using different kinds of particles. The most common methods are horizontal deposition [36] where a drop is left to evaporate on a substrate, solvent evaporation using confined geometries or vertical deposition where [37] Meijer *et al.*, got a thin film by depositing silica cubes of about 500 nm in diameter. The final result (Figure 16) is an organized crystalline structure with two different kinds of particle organization (cubic and hexagonal).

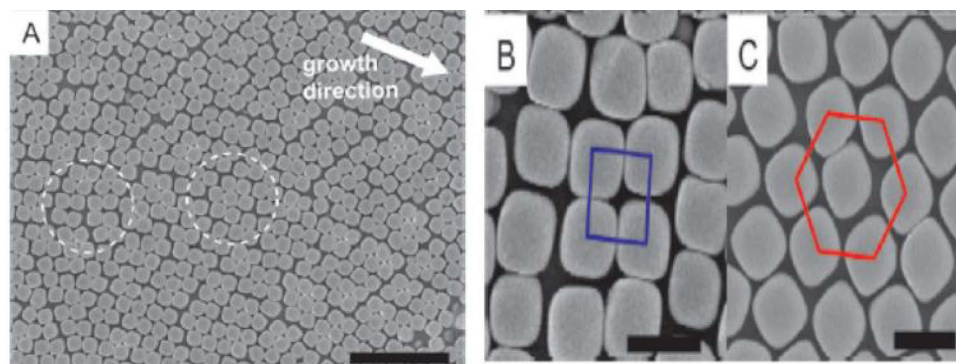


Figure 16 SEM images of a single layer obtain by vertical deposition with an oven-setup (A). Different arrangements cubes: a square-like (B) and a hexagonal-like (C) [37]

In the next chapter we will talk about the assembly of our nanoparticles via microfluidic pervaporation. We will give a brief explanation how it works and how we improved the device to have a better control during the particles assembly.

### 1.3.5 Layer by layer deposition

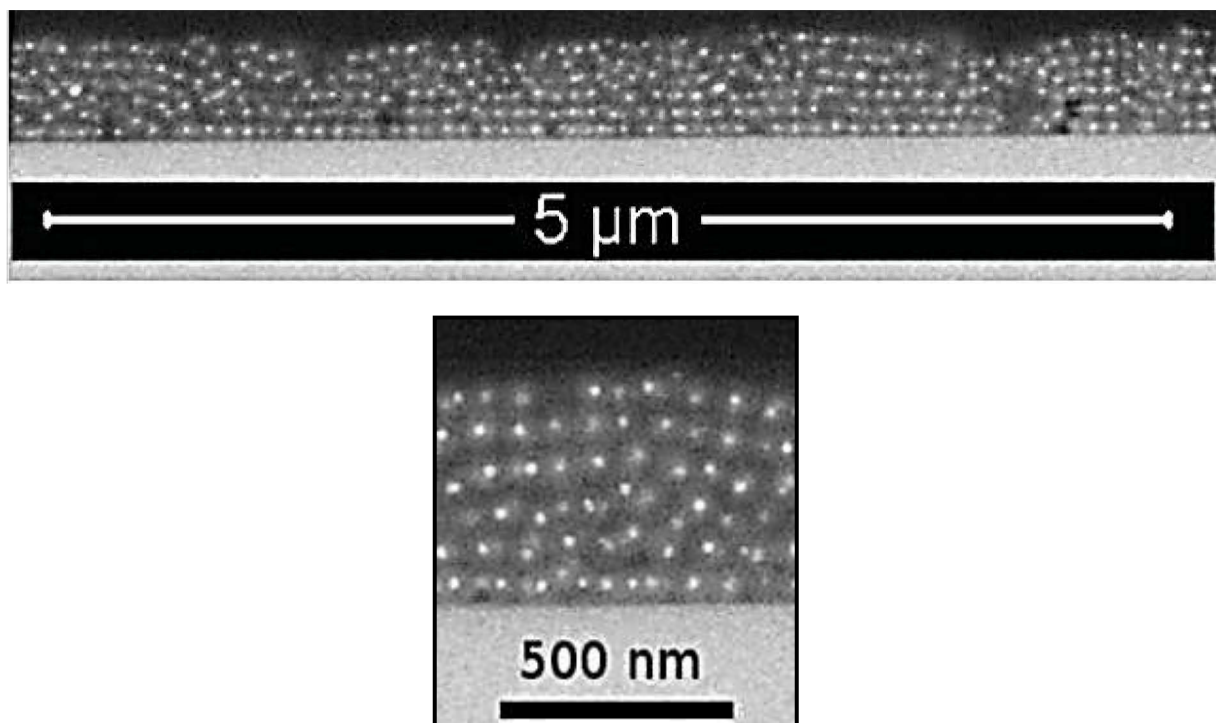


Figure 17 layer by layer deposition via solvent evaporation [38]

In 1920, Langmuir published a study concerning two-dimensional films at gas/liquid interfaces. Using this technique, it was possible to obtain well-organized amphiphilic monomolecular films [39].

Latter, the same technique was applied to particles to make a dense film of particles which can eventually be transferred onto a substrate (Langmuir-Schaefer technique).

Barois *et al.* [38] assembled silica-coated silver or gold nanoparticles by a Langmuir–Schaefer technique into thin films of large area and well-controlled thickness. The silica shells ensure a constant distance between the metal cores, hence providing a constant coupling of the plasmon resonance of the nanoparticles in the assembled composite material. The results suggest a practical way of achieving high phase sensitivity in plasmonic metamaterials.

### 1.3.6 Microfluidic self-assembly

Figure 18 shows the generic fabrication of materials by “microfluidic self-assembly”. It entails an understanding of the physical-chemistry and processes that induce a change in state of a dispersion or a solution in link with specific transport phenomena.

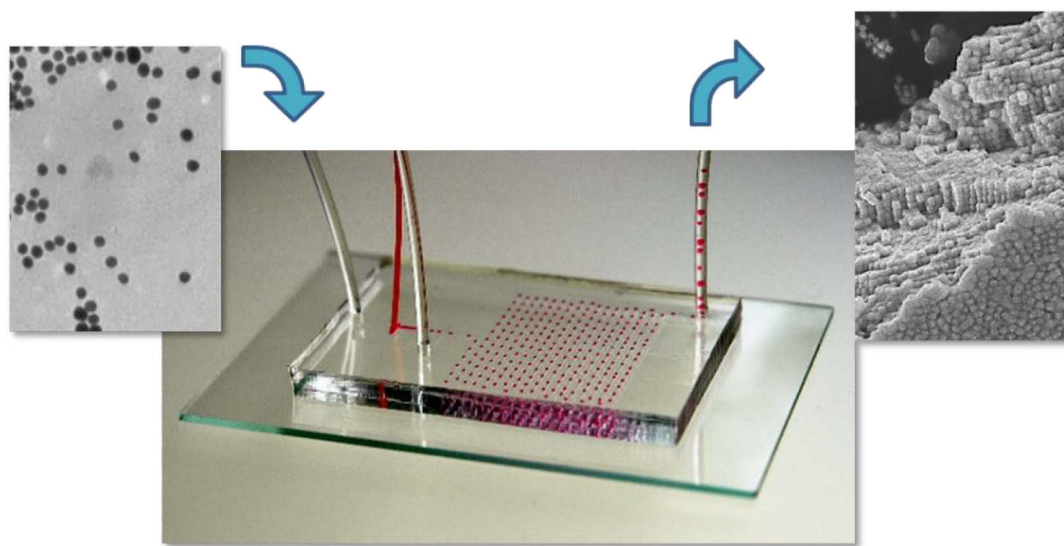


Figure 18 Schematic view of “microfluidic self-assembly” of nanoparticles to obtain dense 3D materials.

Indeed, the underlying phase diagram depends a lot on the system we consider (e.g., colloids, polymers, nanoparticles, graphene sheets, nanotubes, etc.) and the process may also vary a lot and it implies different ways to change the concentration: e.g. dialysis, drying and filtration are good examples of similar yet different processes which are relevant to self-assembly. In the following, we will use only tools based on evaporation or pervaporation (evaporation across a dense membrane).

To build metamaterials working in the visible range (typically 380 – 740 nm) and based on the properties of single resonators, we chose to assemble specific nanoparticles either purchased commercially or fabricated by colleagues from our different collaborations. Particles must have a diameter of about 100 nm maximum in order to lead to an effective medium for the propagation of electromagnetic waves in the visible range. In the fabrication process we will more precisely use a

bottom-up approach using microfluidic devices based on solvent pervaporation, i.e. evaporation across a permeable membrane, in order to fabricate a dense material starting from the particles dispersed in a solvent.

The microfluidic device is designed in order to permit us to guide the (self) assembly of different kinds of solutes from small molecules to macromolecules, including, polymers, colloids, etc. Specifically, our main tools are based on pervaporation which takes advantage of the permeability of PDMS to many solvents [40] and which leads to an increase of the concentration of solute, possibly up to their solidification in a microfluidic channel. We will describe below the many generations of devices we developed in order to reach the ultimate tool to fabricate “large-scale”, defect free metamaterials.

# Chapter 2 – Materials and methods

## 2.1 Introduction

In this chapter, we show the bottom-up microfluidic technique used during this thesis work, the difficulties and the related solutions encountered using different types of micro devices developed to achieve aim of the project.

## 2.2 Experimental challenges

Figure 19 displays schematically the different steps of this thesis work: the use microfluidic self-assembly to make bulk 3D materials made of dielectric particles and suitable for further optical characterization using ellipsometry. For this, we faced several technical and scientific challenges:

- The materials we wish to fabricate with microfluidics are dedicated to further ellipsometric characterizations. As a matter of fact, microfluidics is so far the only tool that leads to materials with a smooth surface and with dimensions which are compatible with micro-spot ellipsometric characterizations (beam spot typically in a range of 75  $\mu\text{m}$  to 500  $\mu\text{m}$ ). Measurement of the refractive index were done on a dense material made by raspberries-like nanoparticles assembled as already mentioned in chapter 1 [24]. Our colleagues now require larger samples for large-spot ellipsometry. This requires to make smooth samples (and possibly defect free) with the corresponding typical size: 10-50  $\mu\text{m}$  thickness, width x length  $\sim$  3 mm x 5 mm;
- The surface must be of optical quality, and the bulk defect free. However, it is well known that upon drying, colloidal assemblies tend to develop cracks and defects. We will need to find a way to prevent these catastrophic events;
- The dispersions provided by our colleagues are dilute (0.1 – 1% volume fraction) which makes them long to assemble up to dense solids (volume fraction of about 60-70%), especially on very large scales. We therefore expect issues regarding the colloidal stability of the dispersion, the sedimentation of the nanoparticles, etc.

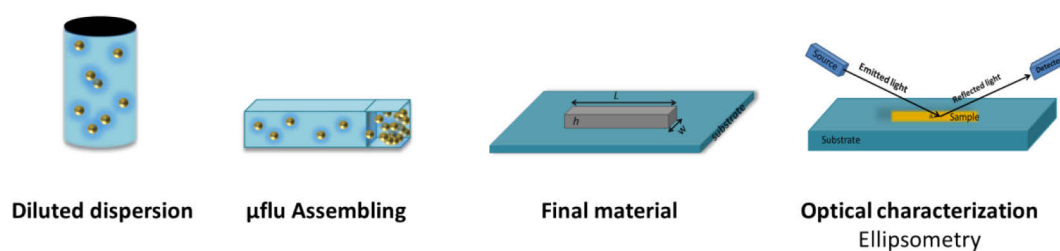


Figure 19 specifications and general sketch of this thesis work

### 2.2.1 Stability and Sedimentation

Using micro-pervaporation assembling techniques requires the use of solutions or dispersions that are stable for sufficiently long times or at least on time scales similar to the time of the assembly inside the microchannel. D.J. McClements define the stability of a dispersion as: “*the ability of a dispersion to resist change in its properties over time*” [41].

To be functional, a dispersion must be capable of suspending the dispersed phase for a long time (the assembly time in our case) or it must be easily re-dispersed after sedimentation. Several factors can influence the particle stability such as thermodynamic or kinetic contributions. For example, particles can be stabilized by steric or electrostatic interactions or by high solvent viscosity in order to slow down the particle sedimentation and their aggregation.

For sub-micrometer colloids, particles are strongly influenced by the Brownian motion, but sedimentation may also become significant especially for large particles (>100 nm), and if there is a substantial difference in density between the dispersed phase and the continuous phase.

To get an idea of the sedimentation time of the nanoparticles it is possible to estimate the sedimentation speed. The latter is directly proportional to the particles size ( $R$ ) and inversely proportional to the solvent viscosity ( $\eta$ ). The particles settling velocity is given by balancing the gravity force (pulling down) and the drag viscous force, leading to:

$$v = \frac{2 \Delta\rho R^2 g}{9 \eta}$$

With  $\eta$  the fluid viscosity, and  $\Delta\rho$  the difference of density of the solid and liquid components.

Knowing the sedimentation speed, it is now possible to calculate whether the sedimentation time is smaller than the assembling process time. Knowing the parameters of our system it is possible to calculate the sedimentation times for each species of nanoparticles using the following formula:

$$t_s = \frac{9 \eta h_t}{2 \Delta\rho R^2 g}$$

where  $h_t$  is the length of the tube used to fill the microfluidic channel with the dispersion of nanoparticles.

### 2.2.2 Pervaporation

In the present work, we use microdevices based on pervaporation in order to extract the solvent from a dispersion and to concentrate this dispersion in a microchannel. The process was studied in details in 1990 for PDMS membranes by Fevre *et al.* and after by Watson *et al.* [42, 43]. This process relies on the solubility of water inside PDMS along with the diffusion of the water molecules inside

the PDMS matrix. Altogether, it permits the transport of water across a PDMS membrane exposed on one side to an aqueous system and on the other side to (more or less) dry air.

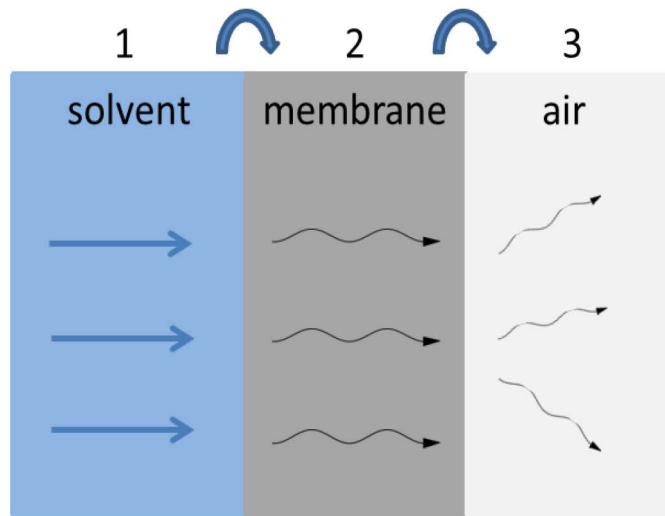


Figure 20 illustration of the pervaporation process of a solvent through a dense membrane. The solvent 1) solubilizes inside the membrane, 2) diffuses across the membrane, 3) evaporates in contact with air.

More generally, pervaporation corresponds to the transport of solvent through a dense membrane following three specific mechanisms (Figure 20): 1) solvent solubility inside the membrane; 2) solvent diffusion across the dense membrane; 3) solvent evaporation in the outside environment. Figure 21 represents a membrane with a thickness  $e$  dividing a compartment containing pure water and another compartment with humid air. From the Fick's law, the water volume flux  $v_e$  across the membrane is:

$$v_e = -D_w V_{mol} \nabla C \quad (2)$$

with  $D_w$  the water diffusion coefficient inside the membrane ( $\text{m}^2/\text{s}$ ),  $V_{mol}$  the molar volume of liquid water ( $\text{m}^3/\text{mol}$ ) and  $\nabla C$  the water molecule gradient inside the membrane ( $\text{mol}/\text{m}^4$ ).

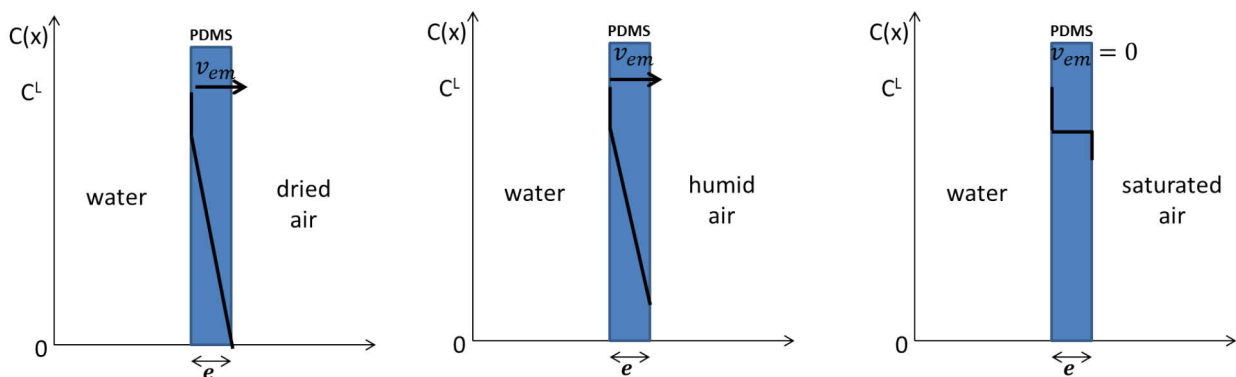


Figure 21 Representation of the pervaporation flow across a PDMS membrane of thickness  $e$ . The membrane divides a pure water solution from a three different cases of humidity air.

The two main parameters influencing pervaporation are thus the diffusion coefficient and the solubility of water in PDMS. In fact in Figure 21, it is shown that the air humidity level also influences the water flow induced by pervaporation across the PDMS membrane. When the air is totally dry ( $RH = 0$ ) the flow in the membrane  $v_e$  is maximum  $v_{e\ max}$ . When air is saturated ( $RH = 1$ ) the flow across the membrane is 0. In between, the flow is also controlled by humidity  $= (1 - RH) v_{e\ max}$ , as shown experimentally by Nobin *et al.* in Ref. [44] and thus  $0 < v_{e_m} < v_{e\ max}$ . To estimate the water flow pervaporating through the PDMS membrane, one needs the value of the diffusivity of the water in the PDMS and the solubility of water in PDMS. Randall *et al.* showed that  $D_w = 8 \times 10^{-10} \text{ m}^2/\text{s}$  and  $C_0 = 40 \text{ mol/m}^3$ . So if we consider a membrane of thickness  $e$ , one can estimate roughly the volume flux of water molecules through a PDMS membrane as shown in Figure 21b by:

$$v_{e\ max} = \frac{V_{mol} D_w C_0}{e}$$

where  $V_{mol}$  is the molar volume of liquid water equal to  $V_{mol} = 18 \times 10^{-6} \text{ m}^3/\text{mol}$ .

For example, if we consider a membrane thickness  $e = 10 \text{ }\mu\text{m}$ , then  $v_{e\ max} = 60 \text{ nm/s}$ . The pervaporation rate is thus proportional to both the diffusivity of water in PDMS ( $D_w$ ) and its solubility ( $C_0$ ).

More recently, the pervaporation process has been adapted to the microfluidic scale [45] where it is shown that in micro-channels, the large surface-to-volume ratio makes pervaporation efficient to extract solvent out of micro-channels.

### 2.2.2.1 Induced flow

Verneuil *et al.* [45] studied the flows in a microfluidic channel molded in PDMS induced by the spontaneous pervaporation of water through the polymeric matrix. Typically they added tracers in their microfluidic channels (typical height 2-125  $\mu\text{m}$  and width 25-477  $\mu\text{m}$ ), and they measured their displacement leading to measured velocities ranging from 0.1 to 20  $\mu\text{m/s}$ . To have a better control and a faster evaporation, Leng *et al.* [46] integrated a thin PDMS membrane, see Figure 22.

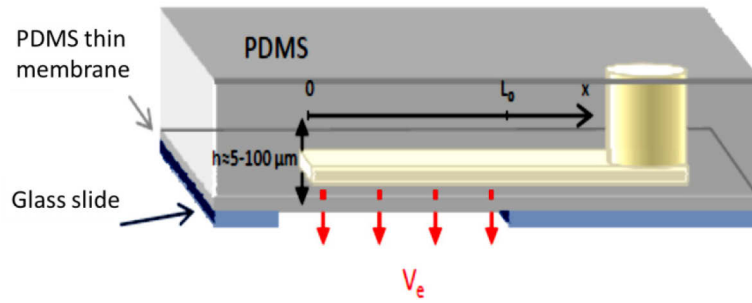


Figure 22 Microfluidic membrane device in PDMS. The red arrows show the side of the pervaporation process [47].

More precisely, a microfluidic channel is molded inside a PDMS matrix with an evaporative length  $L_0$ , a width  $w$  and height  $h$ . The microfluidic channel is sealed by a thin membrane of thickness  $e$ . Typical dimensions of the microfluidic device are  $h \approx 5 - 50 \mu\text{m}$ ;  $w \approx 20 - 500 \mu\text{m}$ ;  $L_0 \approx 0.5 - 10 \text{ cm}$  and membrane thickness  $10\text{-}30 \mu\text{m}$ . One part of the device is closed by a glass slide. The distance between the glass slide and the end of the channel is defined as the evaporative length  $L_0$ . It is therefore possible to define two different areas in the device. The first one is the area closed by the glass slide without pervaporation and referred to as the “reservoir” and the second one, the “evaporative area”, sealed by the membrane.

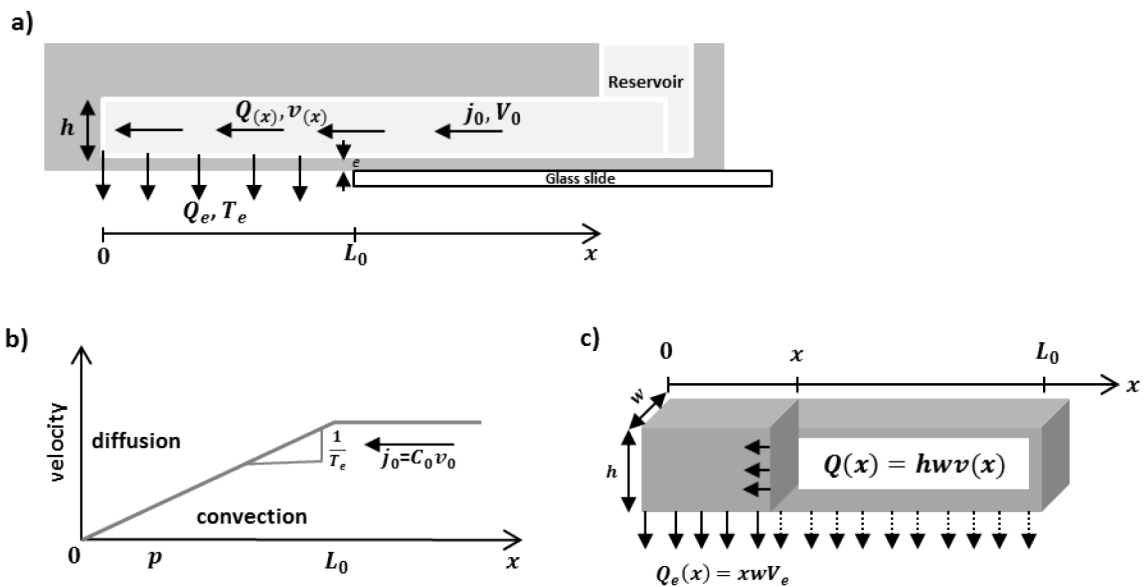


Figure 23 a) microevaporator side view, made by a single channel with height  $h$  and width  $w$ , sealed by a PDMS membrane and deposited on a glass slide. Evaporation length is defined by  $L_0$ , where the water pervaporates through the membrane with a velocity  $V_e$ ; b) velocity flow profile along the microfluidic channel; c) water flow crossing the microevaporation section at the  $x$  position.

It is also possible to define the total pervaporative flux across the membrane  $Q_e$  ( $n\text{L/s}$ ) defined as the pervaporation flux  $V_e$  ( $\text{m/s}$ ) through the membrane surface  $S_e = wL_0$ :

$$Q_e = wL_0V_e. \quad (3)$$

As already shown previously, the water flux crossing the membrane depends on the membrane thickness  $e$  and also on the air humidity outside the membrane. From Figure 23 c the water flux inside the channel at the  $x$  position induced by pervaporation is  $v(x) = h(x)$  and is equal to the water pervaporation flux through the membrane for the channel length up to the  $x$  position [ $Q_e(x) = xwV_e$ , see equation above]. It is thus possible to calculate the flux inside the channel induced by evaporation for a specific position  $x$ :

$$v(x) = \frac{V_e x}{h}.$$

Inside the reservoir ( $x \geq L_0$ ), the liquid flow rate is constant as there is no additional pervaporation and we can write:

$$v(x \geq L_0) = V_0 = \frac{V_e L_0}{h}$$

The evaporation velocity  $V_e$  leads to an induced flow velocity in the channel; the latter is thus obviously controlled by  $V_e$  (and thus by the membrane thickness) but also by the geometry which acts as an amplifier with the factor  $L_0/h$ . This is basically the surface-to-volume transcription: for macroscopic bodies ( $L_0 \approx h$ ) the induced flow in the channel vanishes as  $V_e$  is very small (10-100 nm/s).

We can also define a typical time, the evaporation time:  $T_e = \frac{h}{V_e} = \frac{L_0}{V_0}$  defined as the time needed to empty the microchannel volume once.  $V_0$  is a macroscopic quantity we can measure experimentally, while  $T_e$  is more useful in terms of concentration kinetics, see next.

Typically, the orders of magnitude are:

- Evaporation velocity  $V_e \approx 10 - 100$  nm/s [47]
- $h = 10 - 100$   $\mu$ m
- $L_0 = 1$  mm – 1 cm

As a consequence

- velocity inside the channel  $V_0 \approx 0.1 - 100$   $\mu$ m/s
- Evaporation time  $T_e \approx 10^2 - 10^4$  s.

### 2.2.2.2 Colloidal concentration

Microevaporator allows us to concentrate different species such as: electrolytes, polymers, surfactants but also colloids and nanoparticles. In the microfluidic evaporator developed by Leng *et*

a). the solutes in the channel are convected from the reservoir creating a constant supply of particles at the tip of the channel according to a convective flux,  $j_c$ .

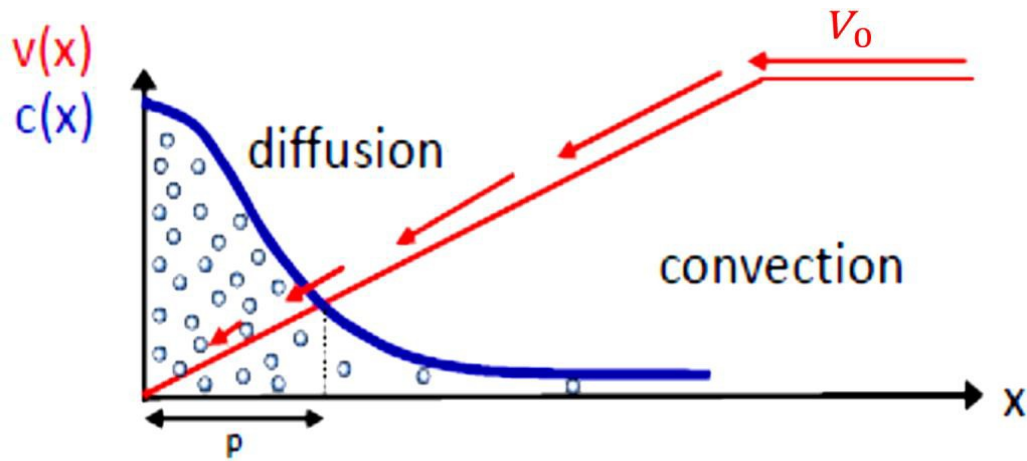


Figure 24 Representation of the balance between convection and diffusion. The red line represents the convective contribution, which is the velocity profile of the pervaporation-induced flow and the blue line represents the solute concentration profile resulting from a balance between convection and diffusion [47].

The flux of particles inside the microchannel is controlled everywhere by a balance of diffusion and convection. However, at the channel entrance the convection flux  $j_c$  is believed to be high and predominant. At the opposite side, at the tip of the channel, the flow rate is weak (vanishing): the diffusion flux  $j_d$  is predominant. It is therefore possible to define a length scale  $p$  where the two effects [ $j_c = \varphi v \equiv j_d = D \nabla \varphi$ ] balance exactly:

$$j_c(x = p) \approx \varphi(p) \frac{p}{T_e}$$

$$j_d(x = p) \approx D \frac{\varphi(p)}{p}$$

leading to  $p = \sqrt{DT_e}$ . The solute will accumulate inside a box of size  $p$  which depends on the characteristic evaporation time of the micro-pervaporator and on the diffusion coefficient  $D$  of the solute.

For  $p < L_0$  it is possible to estimate the increase of concentration  $\Delta\varphi$  into the volume  $pwh$  for a given time  $\Delta t$ . According to the solute mass conservation, the variation in the concentration is equal to the solute flux entering the channel with the concentration  $\varphi_0$  during the time  $\Delta t$ :

$$pwh\Delta \approx \varphi_0 V_0 wh \Delta t$$

so, we obtain:

$$\frac{\Delta\varphi}{\Delta t} = \frac{\varphi_0 V_0}{p} = \frac{\varphi_0 L_0}{p T_e}$$

This formula enables one to estimate the concentration at the tip of the channel as a function of time.

Let us now consider practical cases such as colloidal accumulation. In this case, the concentration process from a dilute dispersion continues up to reaching the formation of a dense colloidal assembly at the tip of the channel. A. Merlin [47] studied the case of large latex particles (1  $\mu\text{m}$  diameter); upon concentration of the particles, Merlin observed the formation of a colloidal crystal (most of the time) with a packing density of about 60-70%, as shown schematically in Figure 25a below. Water can thus still flow through the dense colloidal phase and the solvent can still pervaporate across the membrane. In this way the dispersion flow rate  $V_0$  at the channel entrance is constant during the colloidal accumulation.

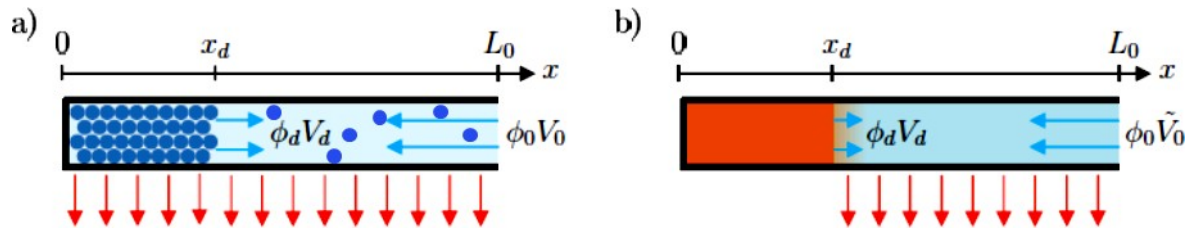


Figure 25 pervaporation influenced by the dense state. a) the colloidal assembly doesn't influence at all the pervaporation; b) polymer dense state influence the pervaporation process [48]

In Merlin's works [47], a constant growth rate of the dense colloidal state was reported and explained on the basis of solute mass conservation, see equation below, and a constant evaporation velocity:

$$\varphi_0 \approx (\varphi_d - \varphi_0) V_d \quad (4)$$

where  $\varphi_d$  is the concentration at the dense phase and  $V_d$  the growth speed front. So:

$$V_d = \frac{\varphi_0 L_0}{(\varphi_d - \varphi_0) T_e} = \mathbf{const} \quad (5)$$

Angly *et al.* [48] went a step further by comparing the growth rate of two different nanocolloids: the nanoparticles have the same hard core (gold or silver) but two different stabilizations, either steric with a polymer corona (PEG), or electrostatic with a silica shell. Figure 26 shows a) the typical time sequence concerning the growth of a solid of nanocolloids inside a microchannel and b) the front position of the solid of nanoparticles covered with a polymer or c) stabilized with a silica shell.

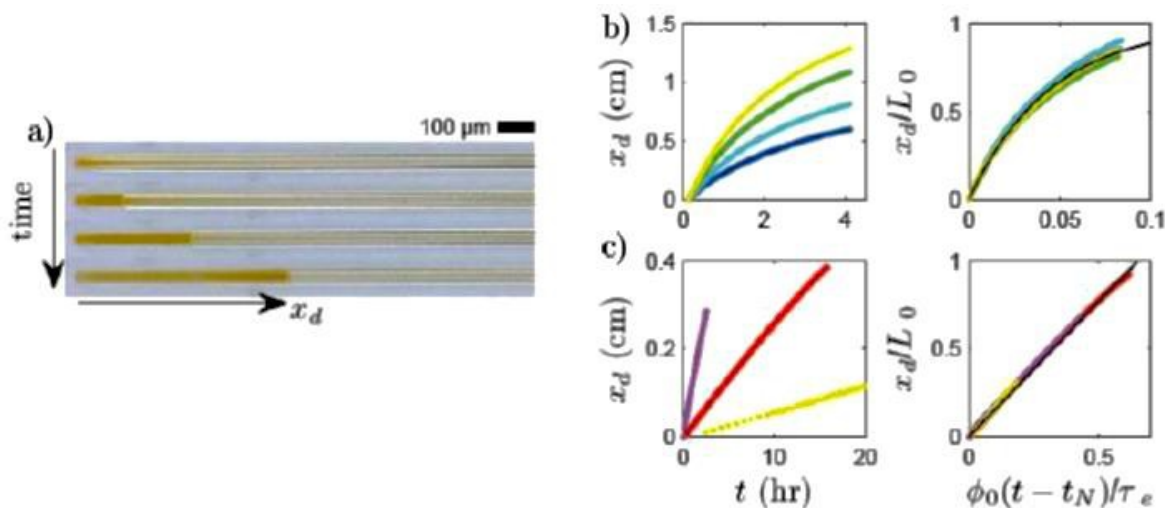


Figure 26 a) colloidal assembly along a single channel in time; b) front displacement of particles covered with a polymer; c) front displacement of particles covered with silica [48]

The difference is striking. In the case of particles covered with a silica shell, the solid that results is porous and solvent pervaporation is not influenced by the formation of the dense state. We recover Merlin's results concerning the constant growth rate and this is because the solvent continues to flow through the dense array of colloids and to pervaporate over time without seeing any kind of obstruction in the channel, see Figure 25a.

In the case of small particles covered by a large polymer brush, however, the solvent pervaporation is perturbed, see Figure 25b. During the particles accumulation the effective length of the "pump" actually decreases because water cannot evaporate anymore from the dense state. It is possible to define the flow velocity,  $\tilde{V}$  at  $x = L_0$  for a reduced evaporative length  $\tilde{l}_0 = (L_0 - x_d)$  by:

$$\tilde{V} = \frac{L_0 - x_d}{T_e}$$

So, the evaporation flow rate is slowed down by the presence of the polymers grafted on the particles surface due to the reduced evaporation length ( $l_0 \rightarrow L_0 - x_d$ ). This leads to an exponential slowing-down mechanism of growth. Indeed, the growth kinetics leads to the packing fraction of the growing solid  $\Phi X_d \approx (1 - X_d) L_0 / t e$ , which admits an exponential solution fitting the data shown in Figure 26b.

### 2.2.3 Microevaporators geometries

For the particles assembly we used three different geometries, increasing each time the microevaporator complexity.

We used the so-called “membrane microevaporator” (see below, Chip 1) to screen different dispersions of nanoparticles and to have an idea about the evaporation time during the accumulation process. But with this device, it is not possible to recover the micro-materials once assembled as the PDMS membrane is sealed on the PDMS device.

We also developed a “unidirectional evaporator” (see below, Chip 2) to recover the material (by removing the PDMS block) and also to have a large surface area for further optical characterization using ellipsometry. We obtained many interesting results but we also faced many issues to control the position of the meniscus which is the only evaporating interface located at the tip of the channel.

So, we also developed a new geometry where we decoupled the “evaporative” area from the “growth” area using again pervaporation (Chip 3). We obtained with this device large scale micro-materials useful for the optical characterization. Below are explained in details these different geometries.

### 2.3.4 Chip 1: Membrane microevaporator

The first microfluidic device is made by a channel, molded inside a PDMS block and sealed by a thin permeable membrane made of PDMS.

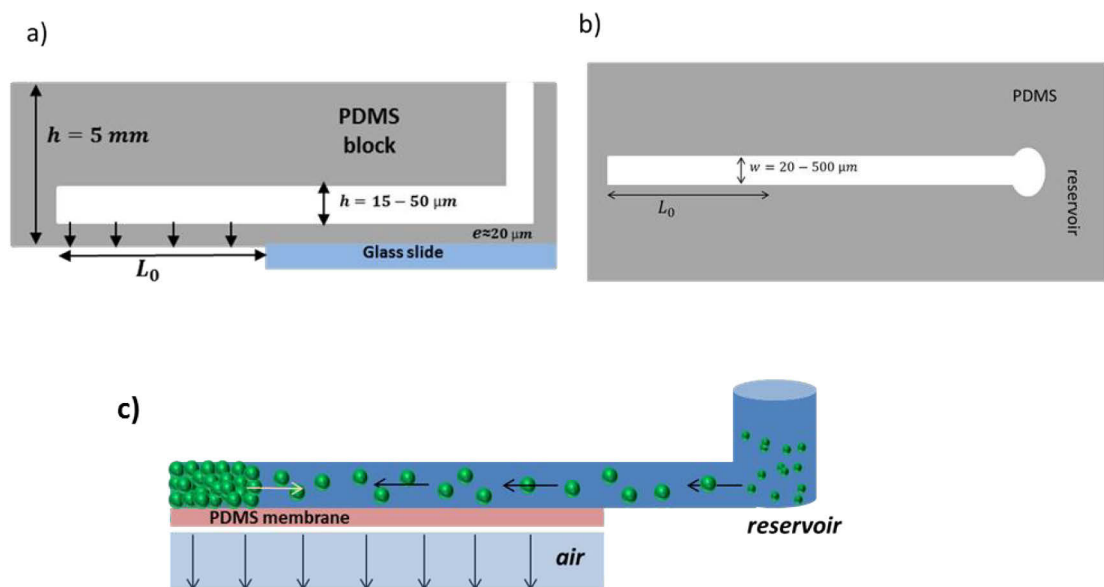


Figure 27 Membrane microchannel. a) Side view of the microfluidic channel; b) top view of the microfluidic channel; c) nanoparticle assembly process driven by the pervaporation-induced flow across the membrane.

Figure 27a represents a side view of the membrane microevaporator developed by Leng *et al.* and used in the different works that we already referred in the previous paragraphs.

With this device, we assembled different kinds of dielectric nanoparticles by obtaining dense materials, but with a small surface for further optical characterization, typically a maximal width of

500  $\mu\text{m}$ , see Chapter 3. Moreover, it is very difficult to peel off the PDMS membrane and to recover safely the material using such chips.

### 2.3.5 Chip 2: Unidirectional evaporator

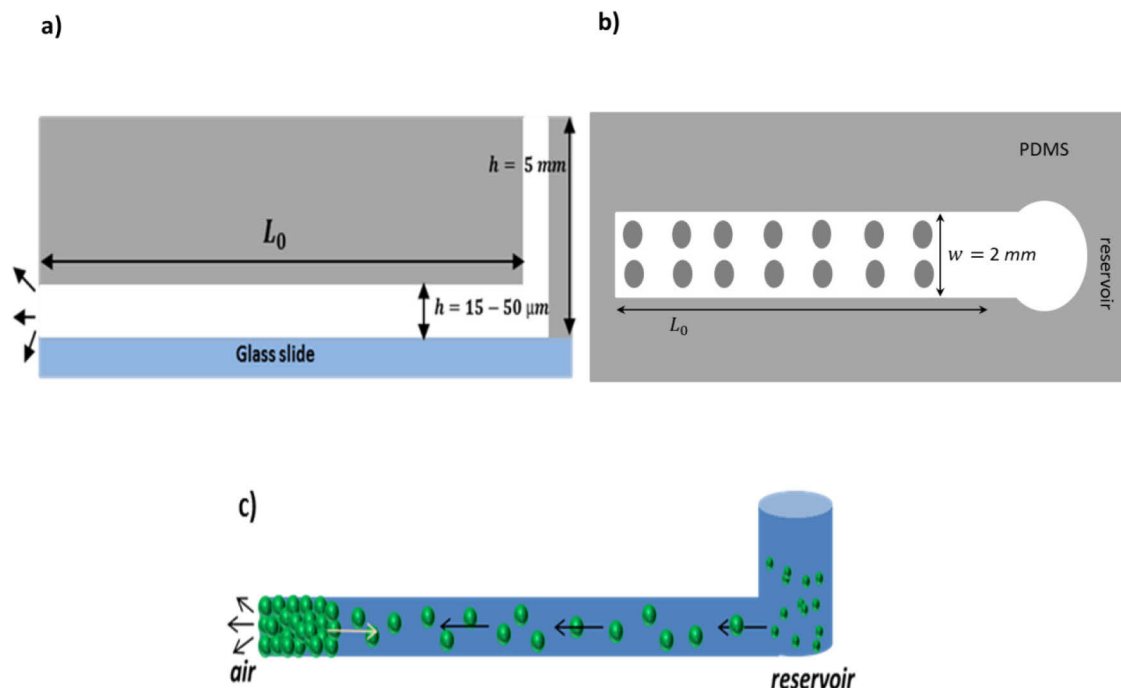


Figure 28 Unidirectional evaporator: a) Side view of the microfluidic channel; b) top view of the microfluidic channel; c) nanoparticle assembly process starting from the only opened point of the channel.

To overcome the difficulties mentioned above, we developed a different device with a larger surface and with the possibility to recover the assembled material from the PDMS mold. The microevaporator, shown in Figure 28, is made by a single channel molded into a PDMS block, with a single evaporative area at the end of the channel (air/dispersion meniscus). The PDMS block is just placed on a glass slide (not sealed using plasma treatment). Using this “unidirectional evaporator”, we obtained different interesting materials starting from dielectric nanoparticles in solution. But we also faced many difficulties especially for controlling the position of the meniscus to start the accumulation of the nanoparticles at a given and fixed position. Also, we needed to include a series of holes inside the PDMS structure to avoid the collapse of the structure due to its large dimensions. The holes were made by including a series of pillars during the lithography process. So, with the inclusion of pillars, the surface area for the optical investigations has been reduced. So, for this reason we decided to design a new geometry that was able to obtain a larger surface for the optical characterization. In chapter 3 we will present a full discussion about this geometry concerning the nanoparticles assembly.

### 2.3.6 Chip 3: Decoupled microevaporator

With this new geometry, we were able to decouple the evaporative area (that “pumps” the liquid) from the growth area where a micro-material is fabricated. As shown in Figure 29, the pumping area is made by a series of small parallel channels to improve the solvent flow induced by pervaporation during the nanoparticles accumulation. As explained later in chapter 3, a “filter” is first formed by using larger particles than the dielectric nanoresonators, around 500 nm – 1 μm in diameter, see Figure 29c. In this way, the large particles accumulate up to forming a porous lattice in this “pump”, leading to a constant and large solvent flow induced by pervaporation, see Figure 29c.

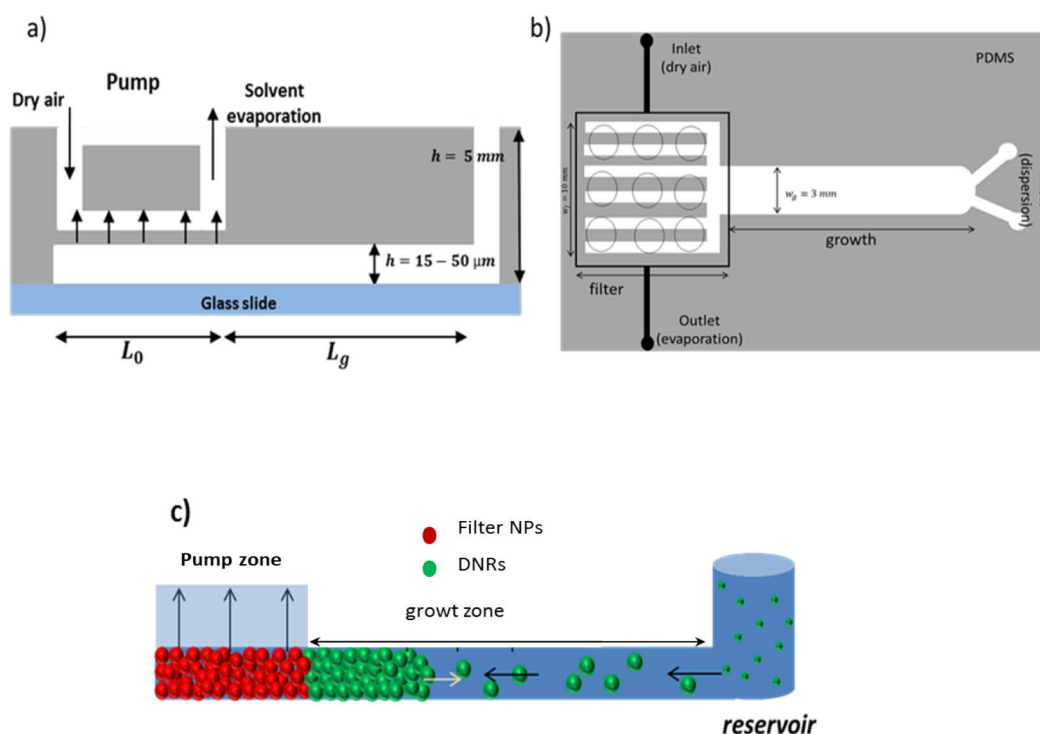


Figure 29 Decoupled microevaporator: a) Side view of the microfluidic channel; b) top view of the microfluidic channel; c) in red filter assembly process and in green assembly of the particles of interest.

Once this filter is formed, it is then possible to change the dispersion containing the nanoparticles of interest at the entrance of the channel. The nanoparticles begin to accumulate at the exact point where the filter ended and the particles can't flow across the filter matrix, but only the solvent can. With this system, we can fabricate in the “growth area” assembled micro-materials with dimensions around  $h = 10 - 50 \mu\text{m}$ ,  $w = 3 \text{ mm}$ ,  $L_0 = 3 \text{ mm}$ . We were also able to recover the final dense material and explore their optical properties as the PDMS device is not covalently bonded on the glass slide. See Chapter 3 for a full discussion.

During the drying process or during the PDMS removal, the material may display fractures or mechanical deformations. To avoid fractures into the material, we also tried to infiltrate the material with different kinds of polymer, see Chapter 3 for a full discussion.

## 2.4 Nanoparticles

During this thesis work, two types of nanoparticles were used. The first ones display the optical properties mentioned in Chapter 1 (Silicon and N-podes), while the second ones, which do not have any optical properties like the previous ones, have been used to test and improve the different microdevices we developed.

### 2.4.1 Silicon nanoparticles

The first type of nanoparticles (dielectric components) we used during this thesis work was a commercial silicon nano-powder purchased from American Elements Company. The powder appears in a yellow brown coloration. Once they are dispersed in a solvent, typically water or ethanol, the nanoparticles, since the very beginning, look as aggregated with a size around 200 nm (estimated by TEM) instead of the 100 nm reported on the company data sheet (Figure 30).

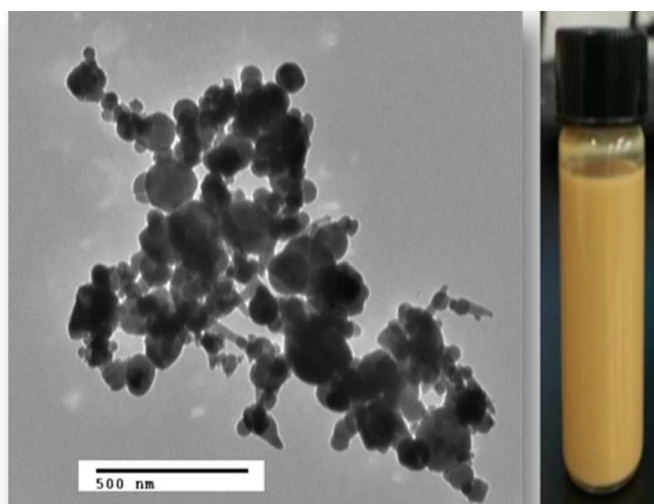


**Figure 30** Silicon nanoparticles TEM images (left), silicon nanoparticles dispersed in water (right). Images V. Ponsinet, P Barois and A. Baron from CRPP

One of the difficulties encountered at the beginning of this work, was the poor stability of these nanoparticles made of silicon: we indeed always observed a rapid sedimentation, in less than 24 h. Different techniques were used, such as using a polymer to prevent the aggregation of the small nanoparticles into large clusters which would sediment rapidly. The polymer used to cover the nanoparticles surface was polyvinylpyrrolidone at 1% wt. The PVP was initially dissolved in water and then added drop by drop keeping the dispersion under stirring. The dispersion was left overnight under stirring. But these trials did not induce any improvement of the sedimentation particles process.

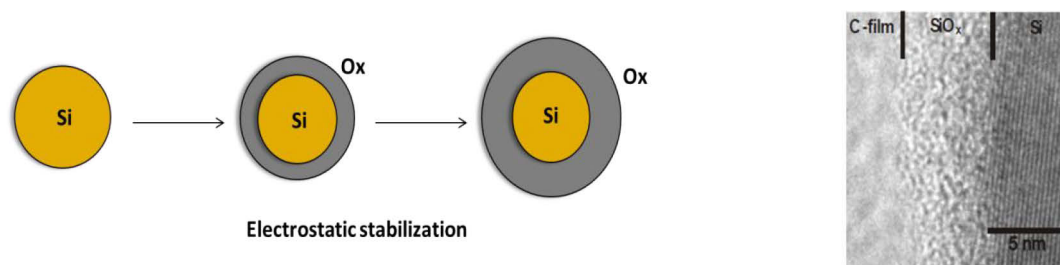


**Figure 31** Schematization of the thin oxidation layer formation in time (left); HRTEM image of three different SiNP surface modification (right) [49].

Over time, typically 1 month, we observed that the dispersions were much more stable. We believe that it is due to a thin oxidative layer that appears on the nanoparticle surfaces making them more stable, and thus slowing down the sedimentation speed (as the formation of large clusters was prevented). Research carried out in the literature confirmed this scenario (formation of an oxidation layer on the surface of silicon nanoparticles) [49]. As shown in Figure 31 (image in the right), high resolution TEM images (on nanoparticles deposited on a surface) indeed confirm the presence of a thin oxidation layer on the surface of the Si crystalline particles.

## 2.4.2 N-podes

The N-podes particles are custom-made metal-dielectric resonators particles. They are made from a silica core (dielectric) with a specific numbers of “patches” (metal) or “satellites”. Satellites are placed symmetrically along the core surface. Previous works have demonstrated, using raspberries-like configuration, that such systems show a strong magnetic response because the light waves induce a resonant loop of plasmonic currents [24].

### 2.4.2.1 Hexapodes

Hexapod nanoparticles have been synthesized by the ICMCB group in Bordeaux using a specific synthesis method able to obtain a given number of “patches” (made of gold or silver) on the surface. As shown in Figure 32 synthesis schematization for the nanoparticles with patches, it is possible to see a schematic view of the nanoresonators fabrication. The synthesis begins from a silica core decorated with 6 polystyrene nodules successively dissolved for the absorption and the consecutively growth of the gold seeds. The gold seeds will form the satellites around the particles [50].

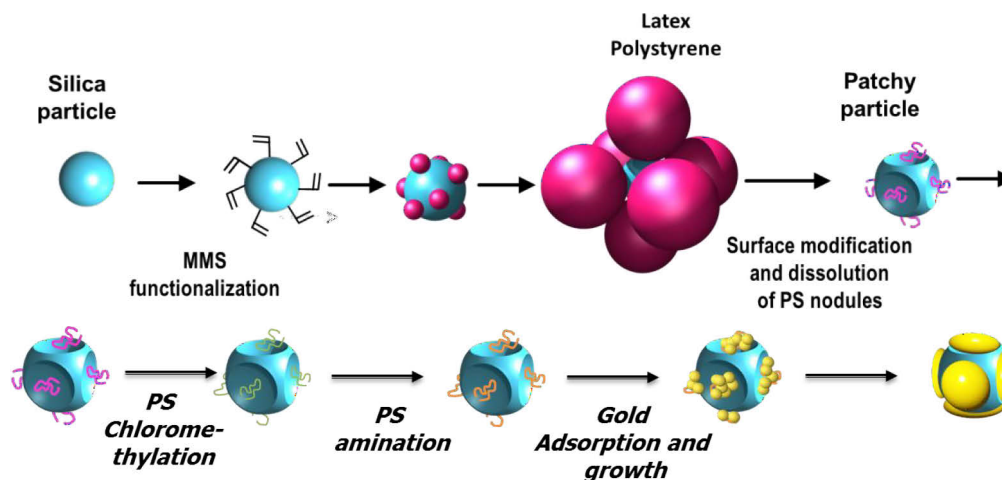


Figure 32 synthesis schematization for the nanoparticles with patches [50]

The final nanoparticles dimension is about 120 nm, respectively given by the silica core diameter of 100 nm and the patches dimension around 20 nm in diameter (Figure 33).

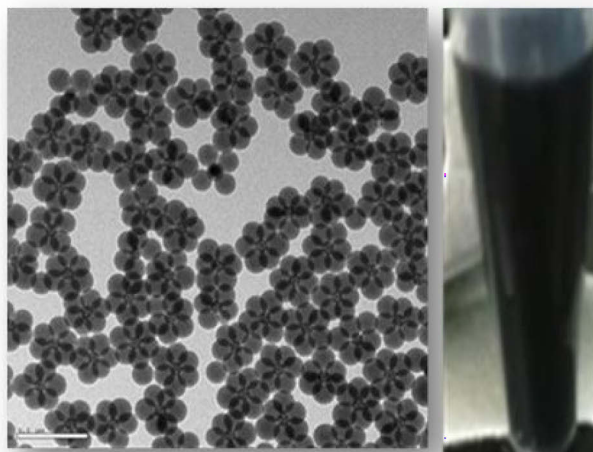


Figure 33 Hexapode nanoparticles TEM images (left), hexapodes nanoparticles dispersed in water (right) [50]

### 2.4.2.2 Dodecapodes

Dodecapode nanoparticles have been synthesized again by the ICMCB group using a specific synthesis method able to obtain a given number of patches (in gold or in silver) on the surface. As displayed in Figure 34, it is possible to see a schematization of the dodecapodes cluster formation. The structure is made by a silica core decorated by 12 polystyrene nodules. Those nodules are successively dissolved leaving polystyrene residues to let the gold seeds to be absorbed and grown until the satellite formation



Figure 34 Synthesis schematization for the nanoparticles with patches [50]

The final nanoparticles dimension is about 120 nm, respectively given by a silica core diameter of 100 nm and patches diameter around 20 nm in (Figure 35).

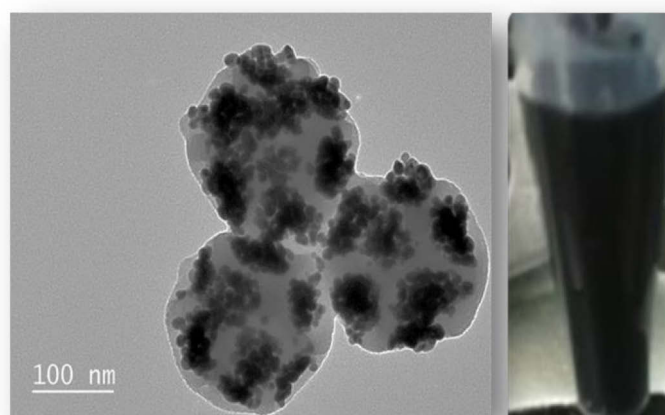


Figure 35 Dodecapodes nanoparticles TEM images (left), dodecapodes nanoparticles dispersed in water (right) [50]

### 2.4.3 Latex

Latex beads are formed from an amorphous polymer, usually polystyrene.

Latex suspensions have been used for their small sedimentation time and their high weight fraction (8% wt.) to obtain fast growth rates of dense materials using our microfluidic assembling techniques, see equations (4) and (5) at page 38. To prevent the latex beads aggregation, they are stabilized by charged carboxyl groups. The carboxyl groups create an electrostatic repulsive barrier between the particles avoiding their aggregation.

Latex beads were used as a model dispersion of particles to design our experiments and test our chips, but also as a “filter” in a second phase of this work, see figure 31 above and Chapter 3.

## 2.7 Microfabrication techniques

The fabrication of our microdevices is divided in many steps: mask design, photolithography, and PDMS molding, see below for details.

### 2.7.1- Mask design

The first step is the fabrication of the 2D microevaporator design choosing the length  $L_0$ , the width  $w$  and the final shape. The design is imprinted on a mask and used for the UV reticulation of a photoresin. Figure 36 below displays three different masks made during this thesis

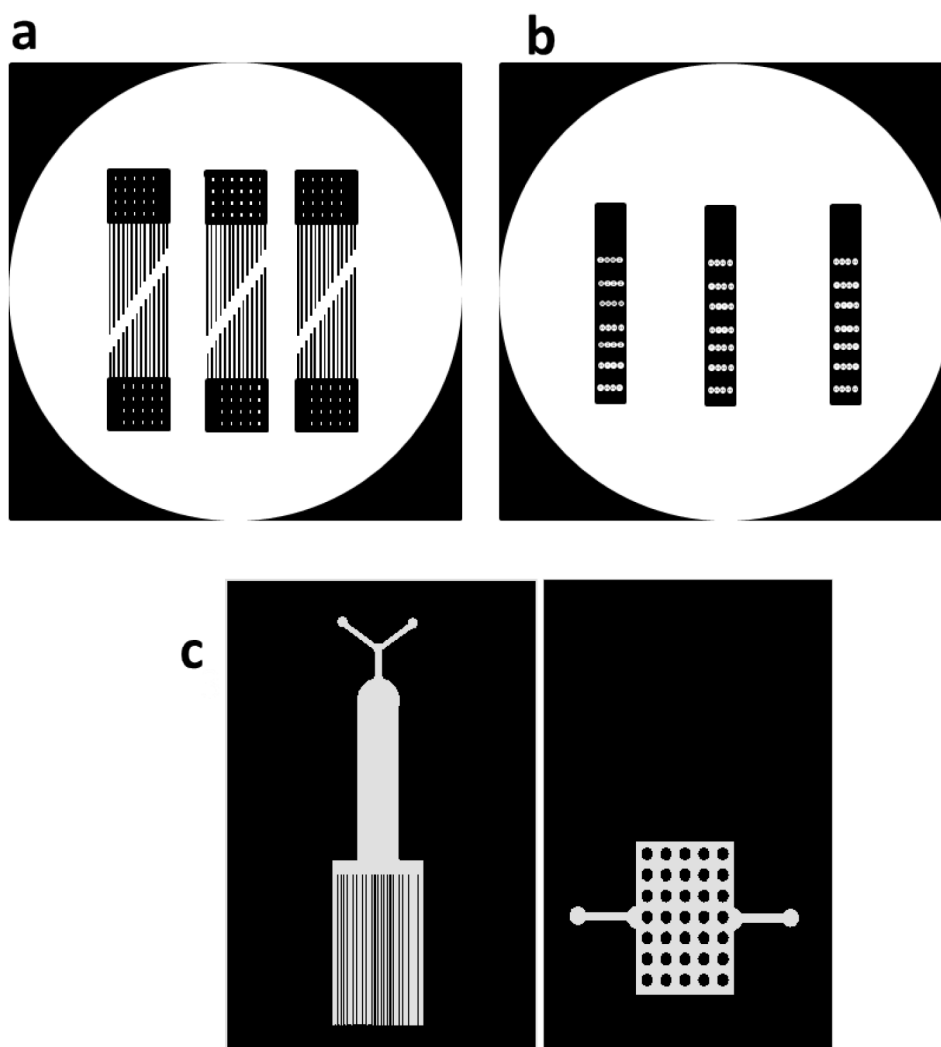


Figure 36 Designs developed during the thesis; 1) membrane microevaporator; 2) unidirection evaporator; 3) decoupled microevaporator

## 2.7.2- SU8 lithography

The pattern on the mask is imprinted on a silicon wafer. The wafer is first coated with a photo sensitive negative resin, SU-8 (MicroChem), and left on a hot plate at 95° (soft baking step), see **Error! Reference source not found.a**. The baking time depends on the height of the desired microchannel. After the soft baking step, the wafer is insolated by the UV light through the mask by a classical photolithography process, see Figure 37b.

Once the pattern is imprinted on the wafer the resin is left to reticulate on the hot plate at 95°C. When the residue solvent is evaporated, we proceed with a “development step” to eliminate the un-reticulated resin and obtain the 3D pattern, see Figure 37c. Typically the entire lithography process lasts one day. Using this technique it is possible to obtain a set of 8 different patterns that can be used to make the PDMS mold for each chip.

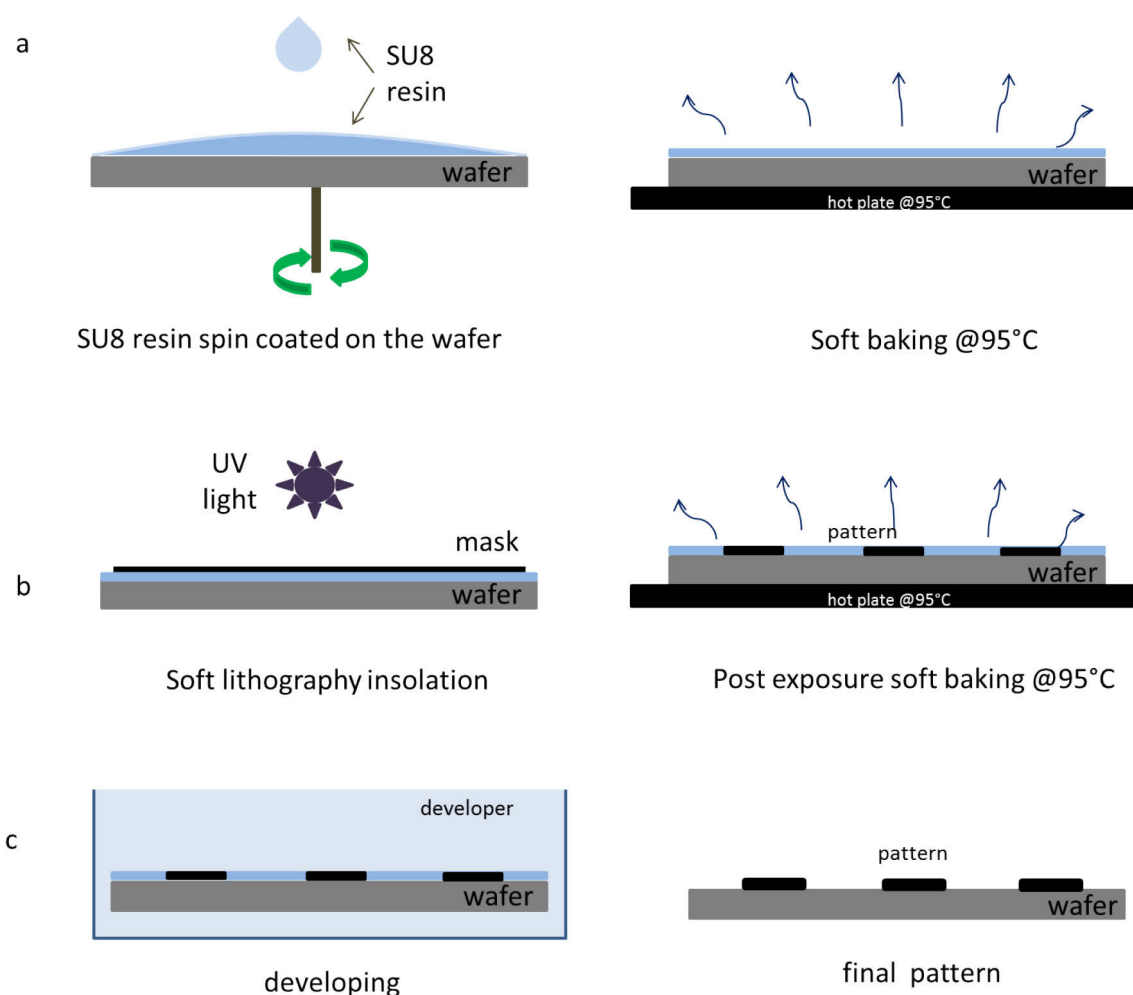


Figure 37 Schematic representation of the fabrication steps of a mold

Figure 38 shows a typical picture of several SU8 molds made during this thesis.

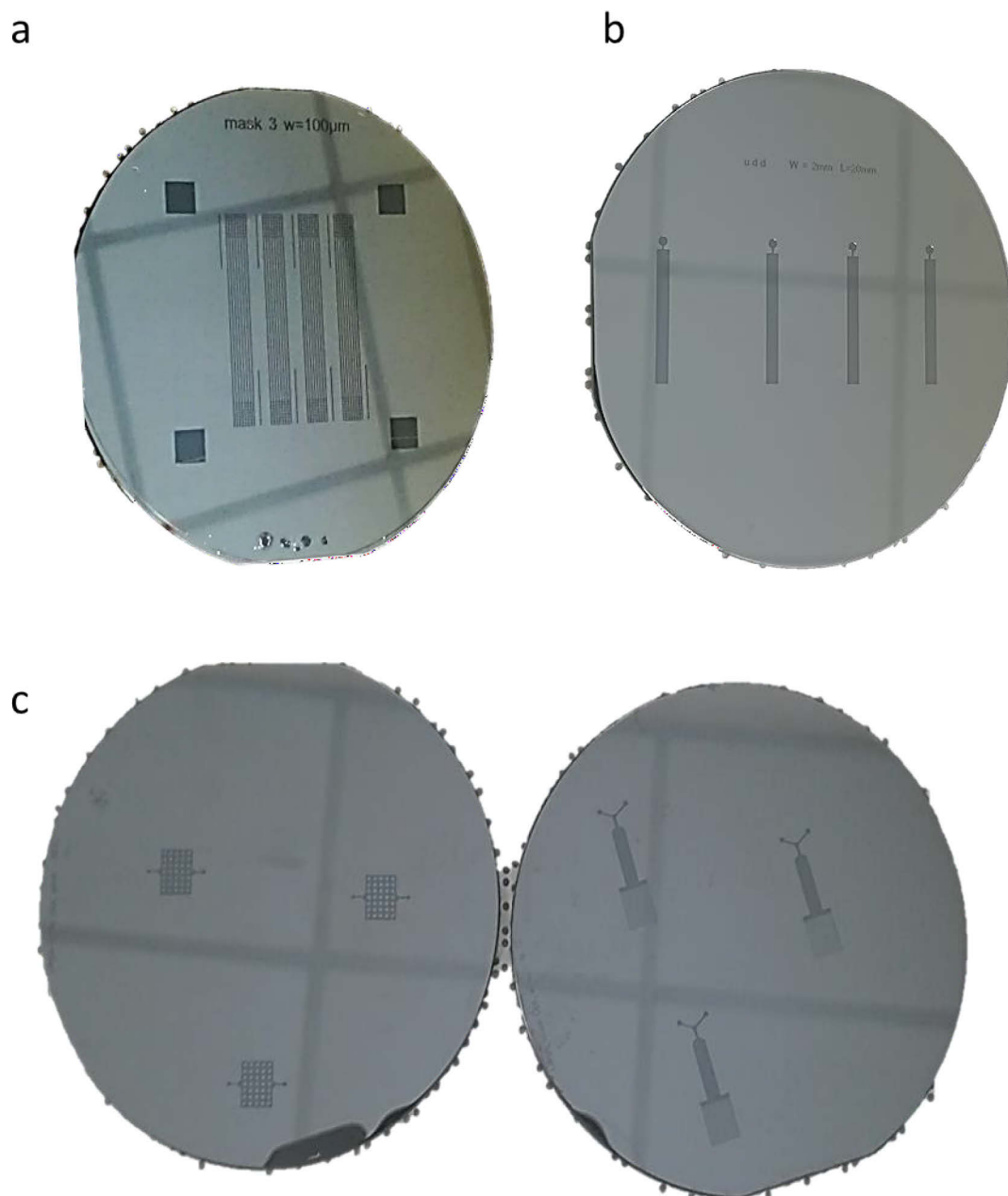


Figure 38 final molds obtained after the lithography process; a) chip 1: membrane microdevice; b) chip 2: unidirectional evaporator; c) chip 3: decoupled microevaporator.

## 2.8 PDMS molding

This step depends on the type of design, see the 3 designs explained above in [2.2.3 Microevaporators geometries](#) section.

### 2.8.1 Chip 1: Membrane microevaporator

The targeted chip is illustrated in Figure 27a above. To obtain this microdevice, we proceed as follows, see also Figure 39.

The PDMS is obtained by mixing silicon oil with its corresponding cross linker. The silicon/cross linker mass ratio is 10:1. After they are mixed together, they are placed into a vacuum bell to extract air bubbles formed during the mixing step. Once the bubbles disappeared the PDMS is poured on the wafer substrate, and left for about 1h in oven at 65°C to make a block of PDMS.

In Figure 39 are shown the different steps of the membrane device manufacturing. The device consists of two levels: level 1 formed by the PDMS block enclosing the channels and level 2 formed by the thin PDMS membrane. In (a), after printing the pattern by lithography, the PDMS is poured on the wafer inside a petri dish in order to form the mold. At the same time, PDMS is spin-coated onto a wafer to make the membrane. The two levels are then placed in the oven for 2 h at 65°C to accelerate the cross-linking process of the PDMS. Once the PDMS layers are cross-linked, level 1 (block) is cut off from the wafer (Figure 39 b).

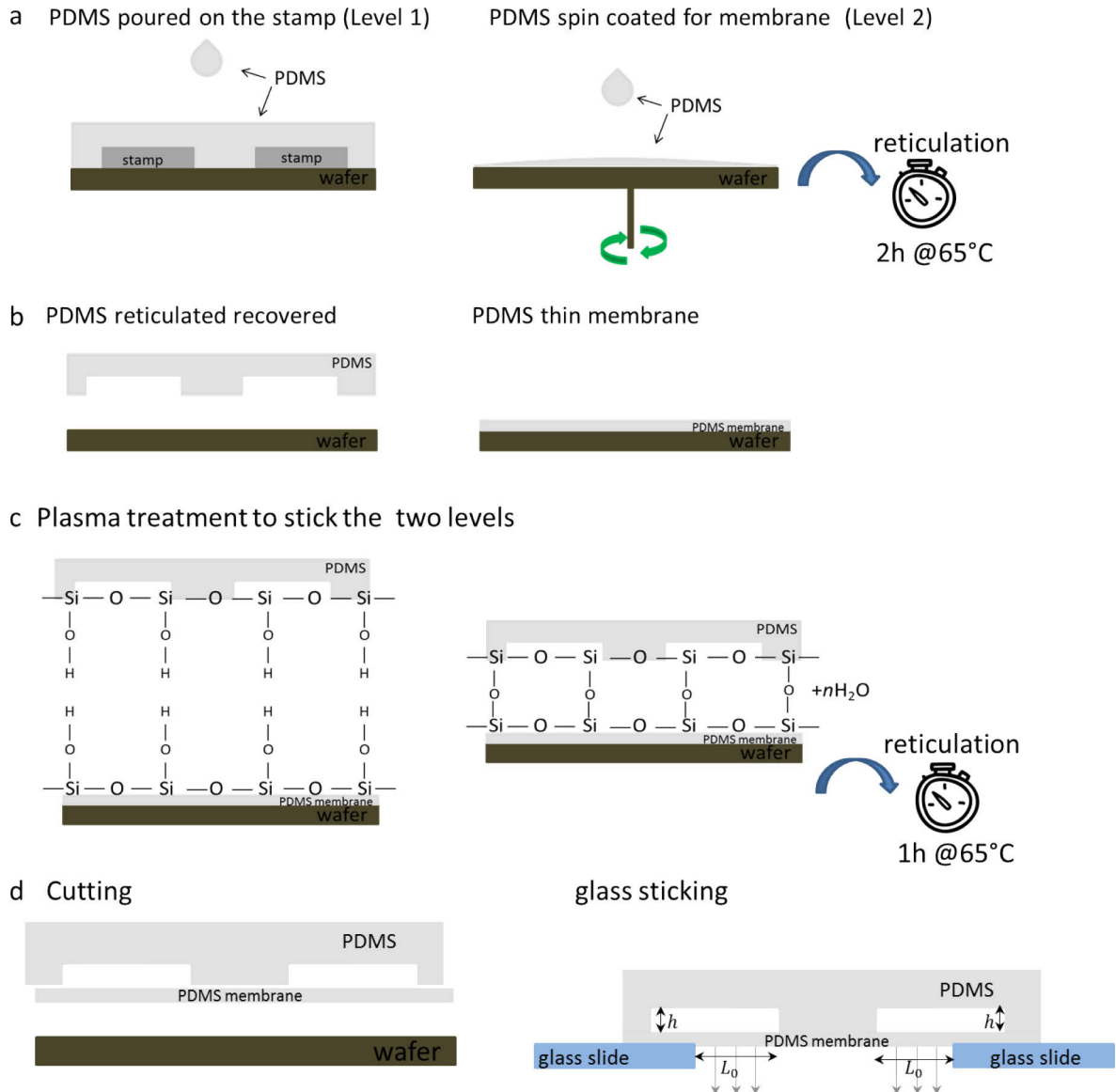


Figure 39 Fabrication protocol of the “Membrane microevaporator”

The PDMS block, after the latter is cut off from the stamp, is sealed using a plasma cleaner on the PDMS membrane layer and put in the oven for 1 h (see Figure 39c). After 1 h, the block sealed by the membrane is again peeled off from the stamp and the reservoir is punched in the PDMS block (Figure 39d). The PDMS device is finally stuck on a glass slide and left in the oven for a night.

The entire fabrication process for the mold in PDMS lasts one day and it is possible to obtain, from 1 to 8 different chips 1 that can be used in the same number of experiments.

## 2.8.2 Chip 2: unidirectional evaporator

The unidirectional evaporator is a “one level” microdevice. In fact, the manufacturing process is fast and simple. As we can see in Figure 40a, PDMS is poured on the wafer with the pattern to make the

mold. The mold is left for 2 hours at 65°C in an oven for reticulating PDMS. Once the PDMS is cross-linked, it is peeled off from the mold (Figure 40 b) and then cut to define an open channel to make possible solvent evaporation in the device (Figure 40 c). Once the reservoir is punched, the PDMS block is simply deposited on the surface of a clean glass slide.

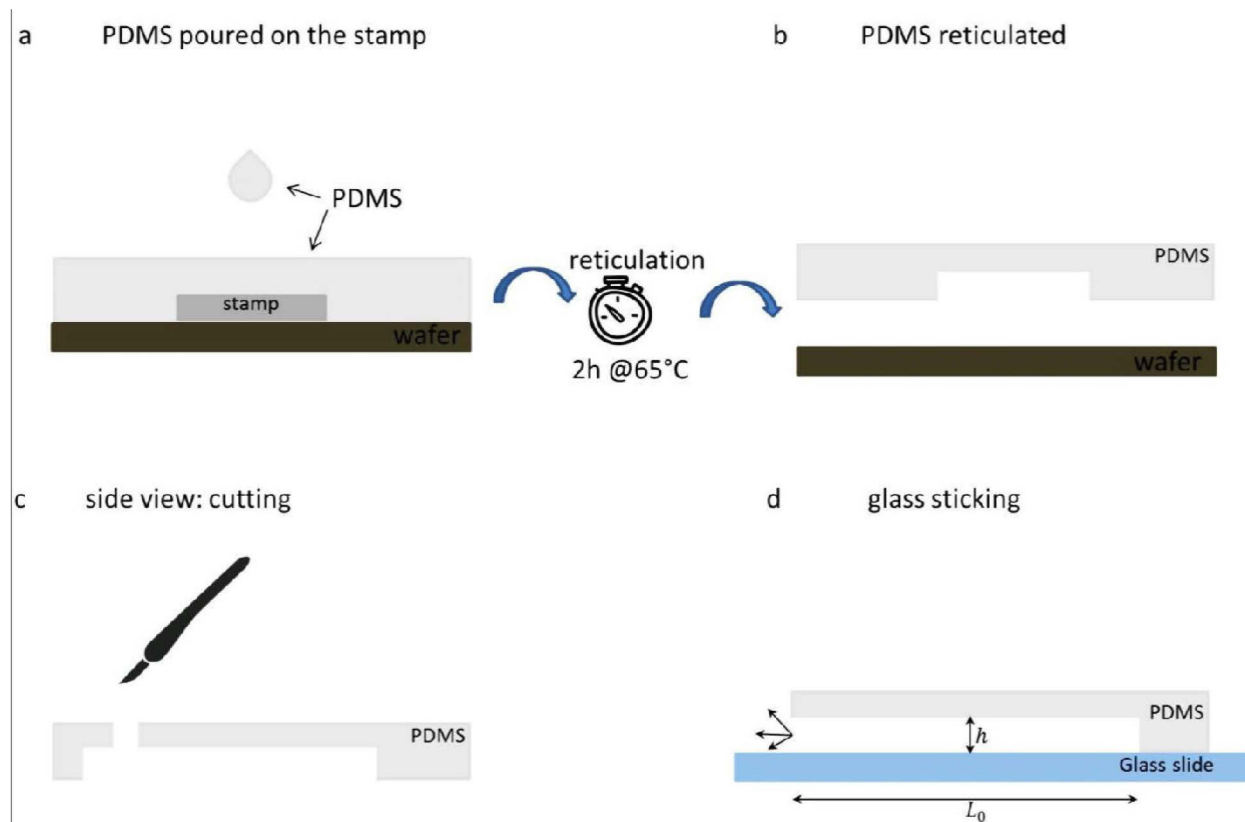


Figure 40 unidirectional evaporator fabrication steps.

### 2.8.3 Chip 3: decoupled microevaporator

The decoupled microdevice, Chip 3, consists of two different levels obtained using classical lithography on two wafers with two different patterns. The first level corresponds to channels for the air flow in order to increase the pump efficiency induced by pervaporation, while the second level is the whole network of the small channels in the pumping area and the “growth” chamber, see Figure 30 page 29. In Figure 41a is shown the first fabrication step, that consists in the fabrication of the PDMS block (level 1) and the thin membrane made by spin coating (level 2).

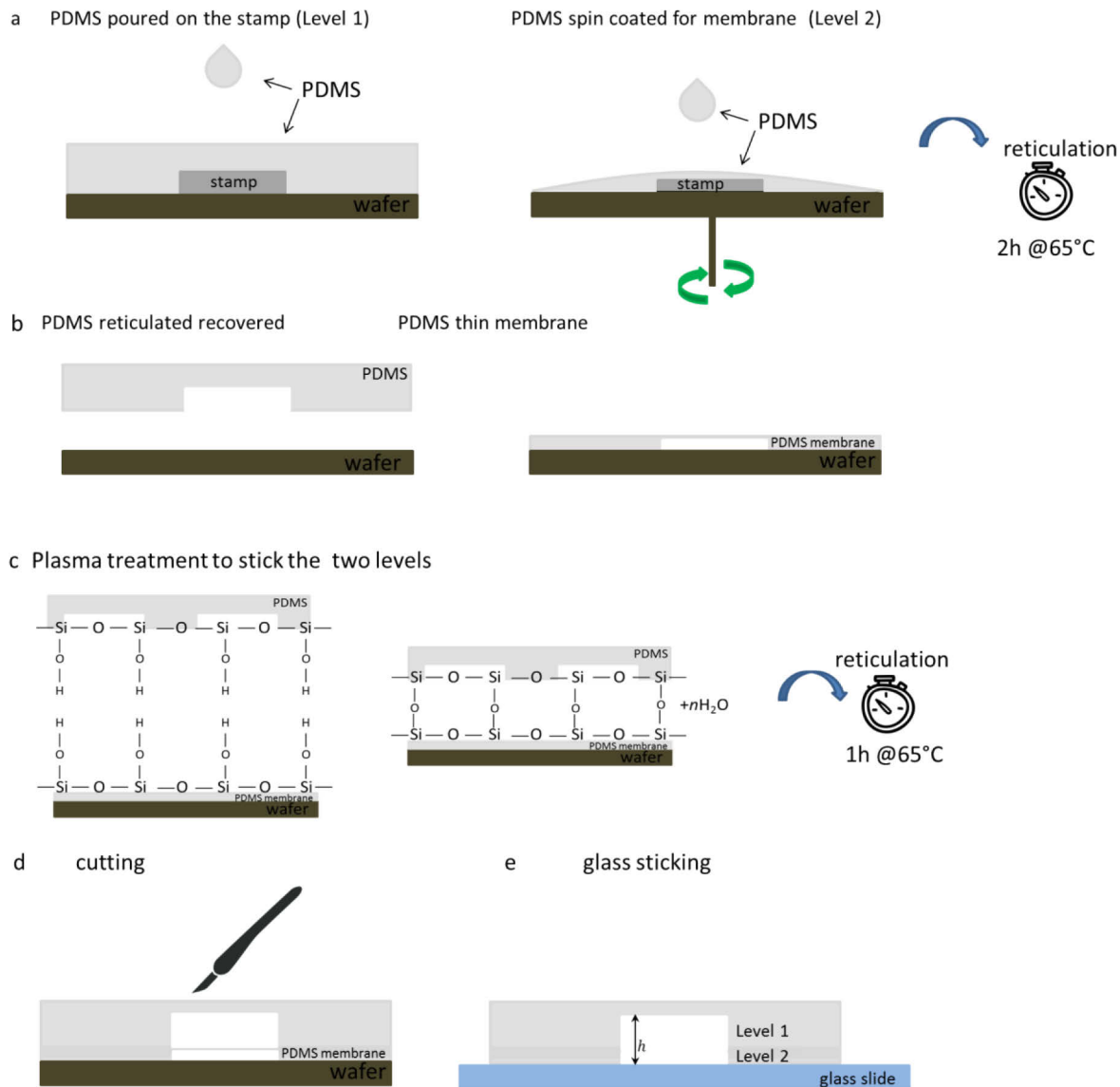


Figure 41 decoupled microevaporator fabrication steps.

The two pieces are left in the oven for two hours to accelerate the cross-linking process. Once the PDMS is crosslinked, the level 1 block is peeled off from the wafer (Figure 41 b) and is bonded together with the membrane by plasma treatment (Figure 41 c). After that, they are left in an oven at 65°C for 1 hour. After 1 h the block is peeled off from the wafer, punched to make the inlets and outlets, and deposited on a clean glass slide (see Figure 41d).

## Chapter 3 – Material assembling

### 3.1 Introduction

In this chapter, we show the different techniques we used to assemble different types of nanoparticles, and how these processes have been improved through the development of different microdevices presented in Chapter 2.

### 3.2 Silicon small scale assembly

Starting from Merlin's work [47], the membrane microevaporator was used for a first self-assembly approach to get an idea of the nanoparticle assembly process inside a microfluidic channel. More precisely, we use the design shown in Figure 39 above.

The microevaporator we used is a membrane microevaporator device made of a series of micro channels of variable length ( $L_0 = 1 \text{ mm} - 1 \text{ cm}$ ,  $w = 100 \text{ }\mu\text{m}$ ,  $h = 15 \text{ }\mu\text{m}$ ). The differences in channel lengths allow us to study the role of the pervaporation-induced velocity  $V_0$  on the self-assembly process.

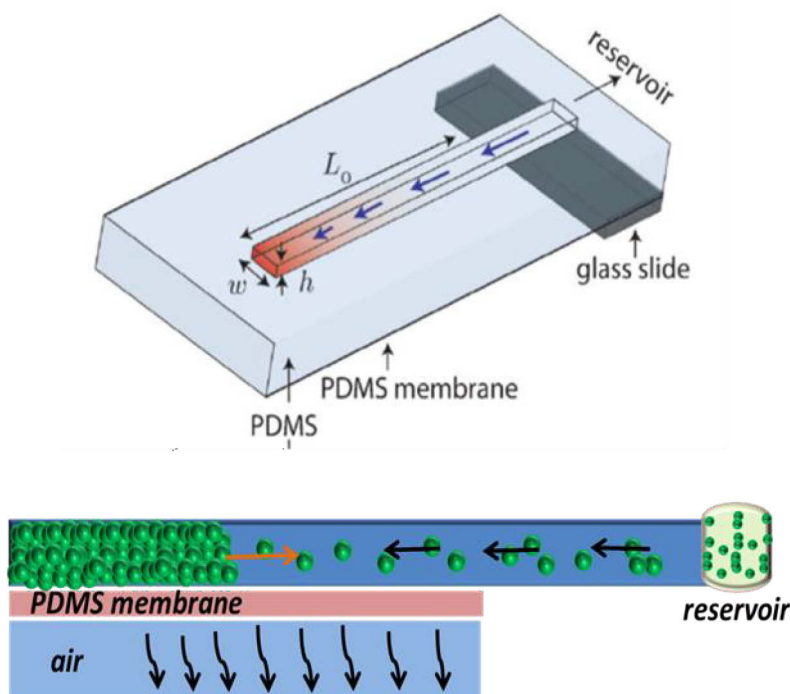
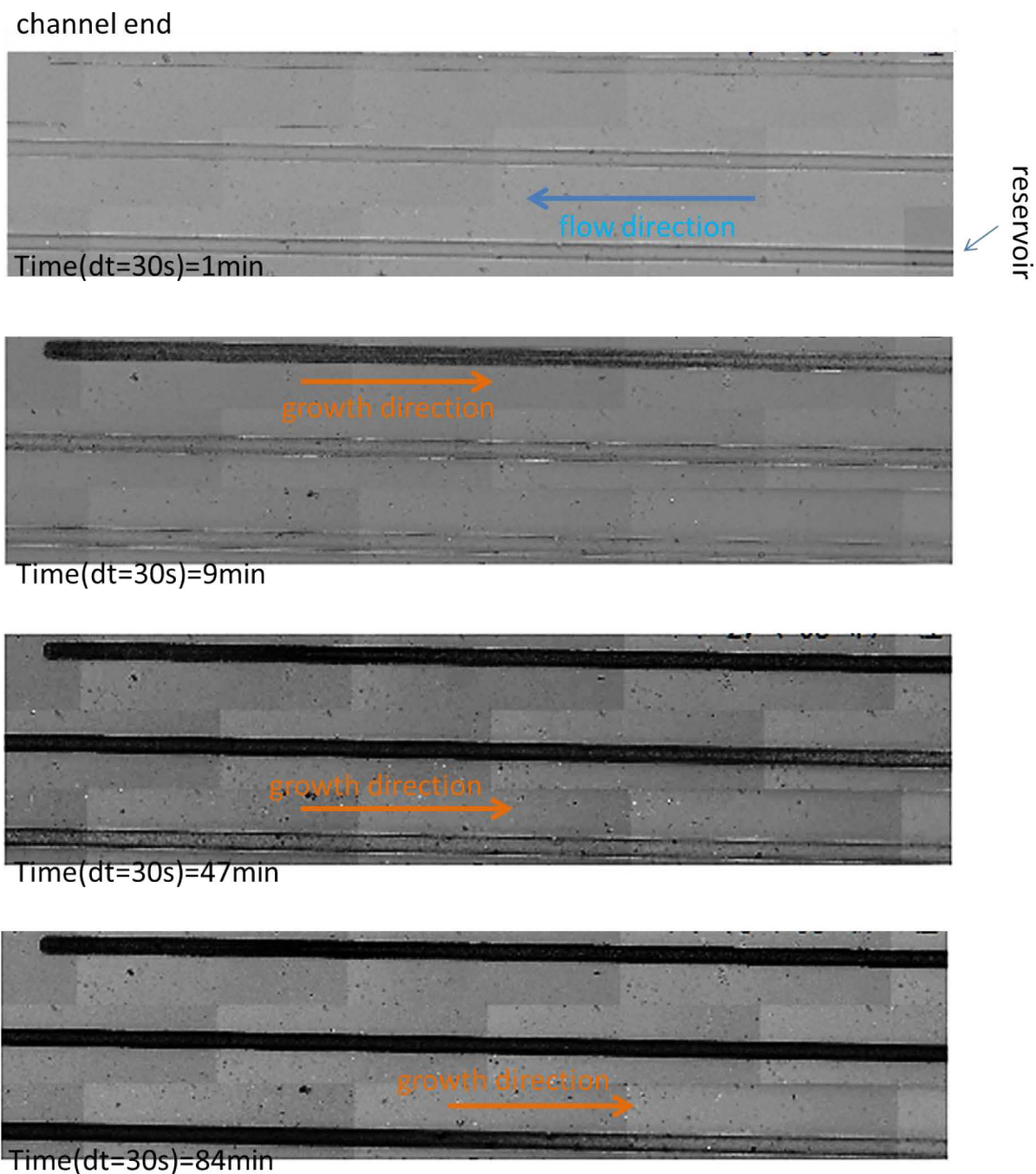


Figure 42 3D Membrane microevaporator Chip 1 (top); channel perspective view of the microevaporation during the accumulation of colloids (bottom).

After manufacturing the device, the silicon nanoparticle dispersion is injected into the channels from the reservoir. Once all channels have been filled with the dispersion of nanoparticles, a small amount of dispersion is left inside the reservoir to ensure a continuous incoming flux of nanoparticles during the pervaporation process.

Using an optical microscope it is possible to observe a specific area of a given sample at a high magnification. The scattered and transmitted light from the sample is collected by an objective lens leading to a magnified image. By using a digital camera, it is possible to acquire images on a computer. Using a programming software (MATLAB), it is also possible to acquire frames in different areas of the sample by coupling the displacement of the motorized stage holding the sample with the image acquisition. Figure 43 shows a top view of the microevaporator after it was filled with a silicon dispersion at a volume fraction 0.7%. The microchannel image consists of the acquisition of three frames at three different locations of the channel. The images are acquired with a time delay of 30 seconds. To simplify the visualization of the images acquired during the experiment, the channel has been divided into three sections (in the lower right corner the tip of the channel and in the upper left corner the reservoir).



**Figure 43** Capture of a single channel during the assembling process in different time after the injection of the silicon nanoparticles. The channel becomes darker in time which is due to the concentration of particles during their assembly.

During the concentration process induced by the pervaporation process, it is possible to follow the formation of the dense material by observing the channel becoming darker due to the concentration of particles up to a point where we can identify a front which we attribute to the growth of a solid phase. Figure 43 shows a single channel during the assembly phase of the nanoparticles at three different stages.

After about 1h from the beginning of the experiment, the silicon nanoparticles are assembled inside the channel. The solvent continues to evaporate until it is completely consumed in the reservoir. After about an hour, dense materials of silicon nanoparticles were thus formed in all channels. Air finally enters into the microevaporators leading to the complete drying of the micro-materials. When the material is completely dry, it can be removed from the device. However, as the membrane is sealed to the PDMS, removal is impossible without breaking the materials. In Figure 44, we managed to extract some parts of the material by using a SEM tweezer (thin tips) for the acquisition of SEM images to get an idea of the micro-structure of the material.

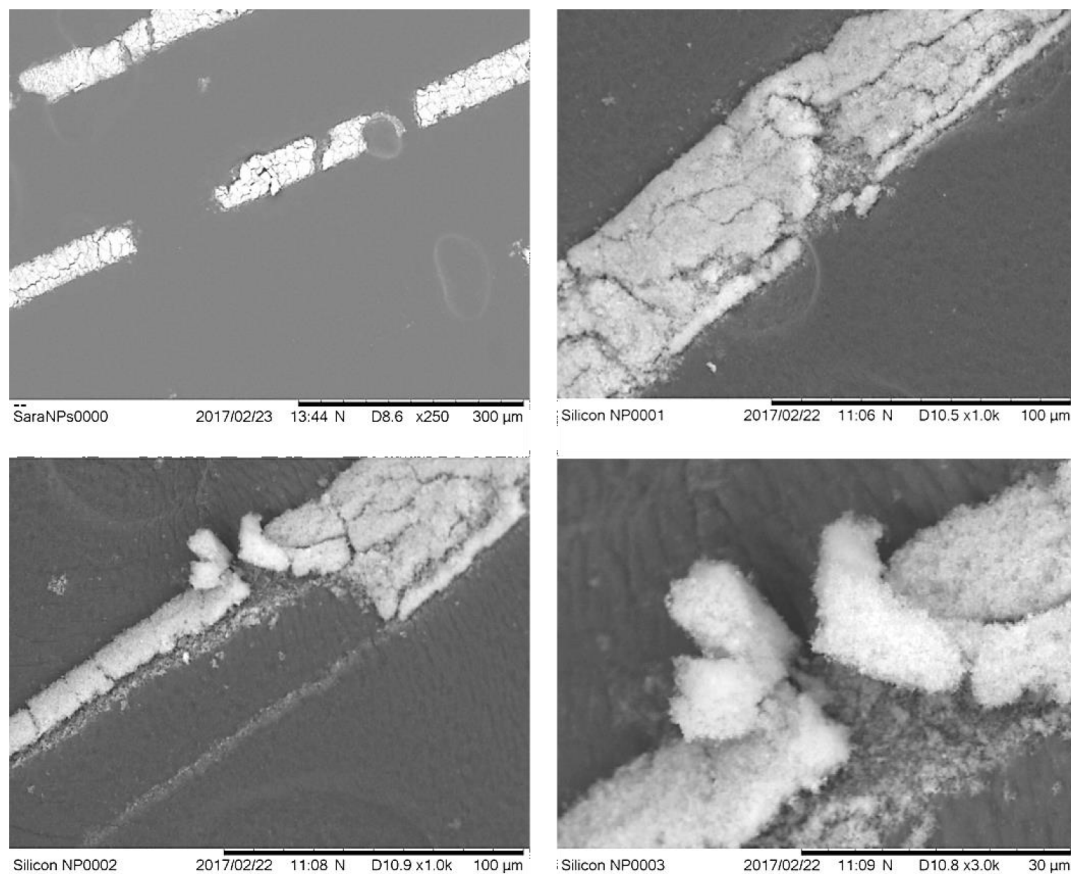


**Figure 44** SEM images of the silicon dense material after the recovering from the PDMS device

From the SEM images we can observe a multitude of fractures in the material and a high surface roughness. Using this kind of microevaporator, we are able to grow a material but the material size is too small and the surfaces are too rough to make possible any optical characterization with standard ellipsometry. For this reason, we decided to increase the surface area of the material and at the same time to get the possibility to easily extract the material from the PDMS mold in order to avoid cracks during this critical step.

## 3.2 Unidirectional evaporator

Considering the problems with the previous design of microevaporators (small surfaces and difficulty to recover the membranes due to the sealed membrane), we developed a new device, the unidirectional evaporator. The device consists of a single large channel ( $L_0 = 15$  mm,  $w = 3$  mm,  $h = 6$   $\mu\text{m}$ ) molded into a block of PDMS and placed on a glass slide. The microchannel has only one location for evaporation, the tip of the channel. This is because the tip of the canal is cut in such a way that it remains open to air, leading to solvent evaporation in the ambient air.

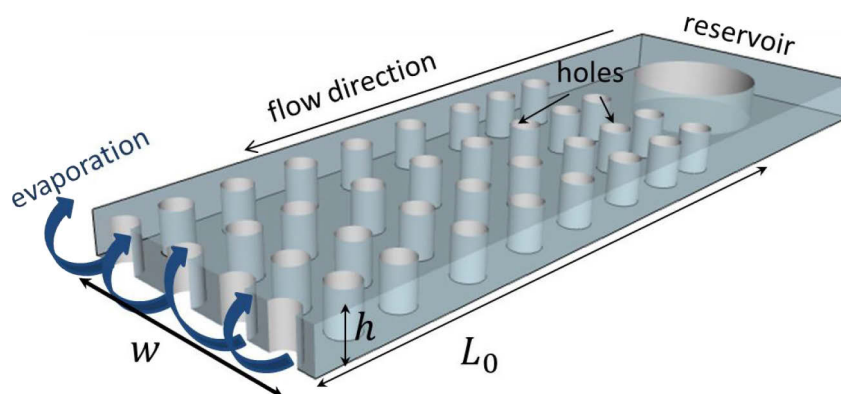


Figure 45 3D unidirectional evaporator device.

After the fabrication process, the dispersion of nanoparticles is injected into the channel up to the opened tip trying to find a stable position for the meniscus to avoid leakages. The big issue encountered during the use of the directional evaporator was the stabilization of the meniscus after filling the channel. The dispersion flowed out of the opening created by cutting the tip of the channel. A pressure controller was used to find the equilibrium point for which the meniscus remained inside the channel (MFCS Fluigent). Once the dispersion flows inside the channel and arrives at the evaporation opening, by using the pressure controller, we tried to tune the inlet pressure to stabilize the meniscus. Once the meniscus is stabilized, and because solvent evaporates, the silicon nanoparticles start to concentrate at the tip, up to the formation of a dense material.

### 3.2.1 Holes evaporator

The assembly process by evaporation of the solvent using the device shown above can take several days. As in the previous case, an optical microscope was used to follow the assembly process of the nanoparticles and visualize the front between the liquid phase and the dense phase. In the following images, it is easy to observe the growth of the material inside the channel as a function of

time. Each image is taken using a digital camera using a programming software (MATLAB). The time delay between each image was about 5 minutes.

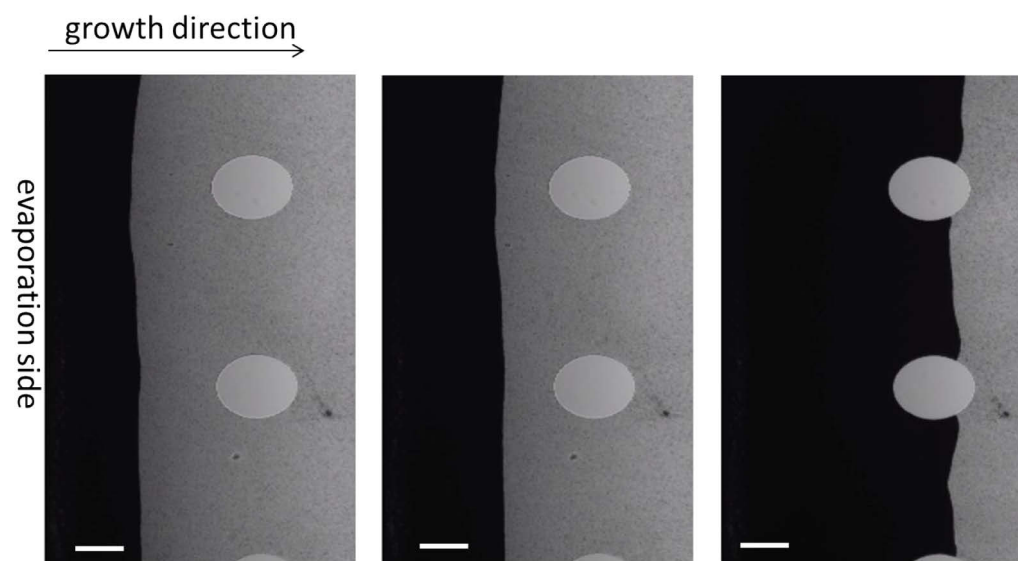


Figure 46 Capture of the channel during the evaporation process and the silicon nanoparticles assembly. The front between the liquid and crystal phase is sharp (in black the dense phase in gray the liquid phase; scale bar 100  $\mu\text{m}$ )

### 3.2.1.1 Material characterization

After being completely dried, the PDMS block is removed and the material is recovered on the glass substrate, see Figure 47. After the material has been recovered, the sample is characterized by optical profilometry to check its thickness and by ellipsometry to extract the optical characteristics of the dense material.

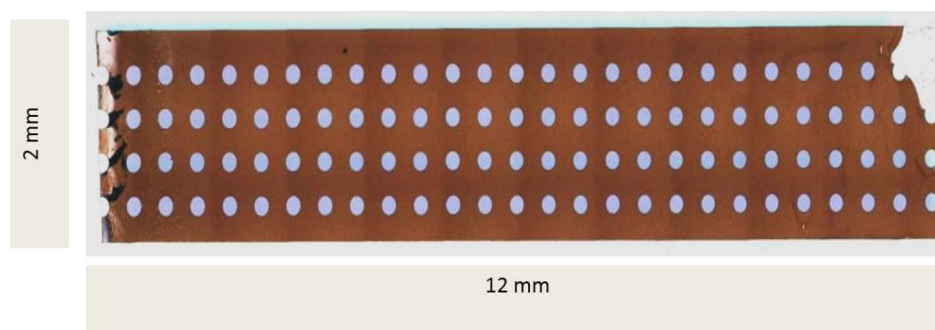


Figure 47 Optical profilometry acquisition of the silicon assembled material

To obtain information on the material height and roughness, optical and mechanical profilometry were used. Profilometry is a technique used to obtain topographic information from a structured material. The goal is to obtain, by a point, a line or a three dimensional reconstruction, the step heights and the surface roughness of a material.

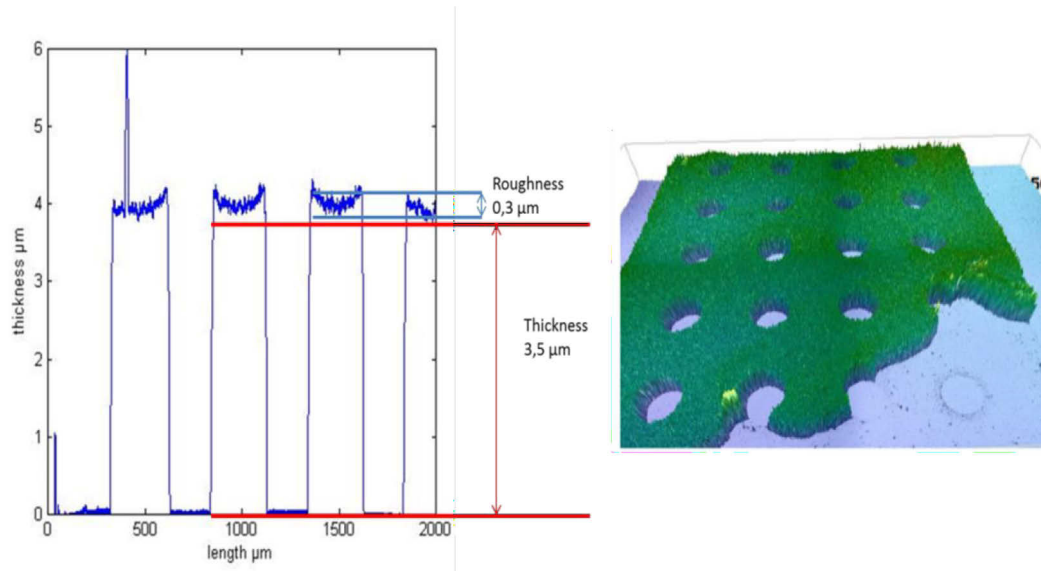


Figure 48 Height profile (left) and 3D topography image of the dense material

A scan of the sample surface was also carried out using a tactile profilometer. As shown in Figure 48, the final material has a height of about 3.5-4  $\mu\text{m}$  (the initial height of the mold from obtained by photolithography was 6  $\mu\text{m}$ ) and a roughness of 0.3  $\mu\text{m}$ , of the same order of the nanoparticles size. Finally, a three-dimensional topographic image of the material was acquired using optical profilometry, see Figure 49, right. It is possible to see that the difference encountered between 3.5-4  $\mu\text{m}$  (the material thickness) and 6  $\mu\text{m}$  (the height of the initial channel) is due to the deformation of the PDMS matrix during the drying of the material that induces mechanical stresses.

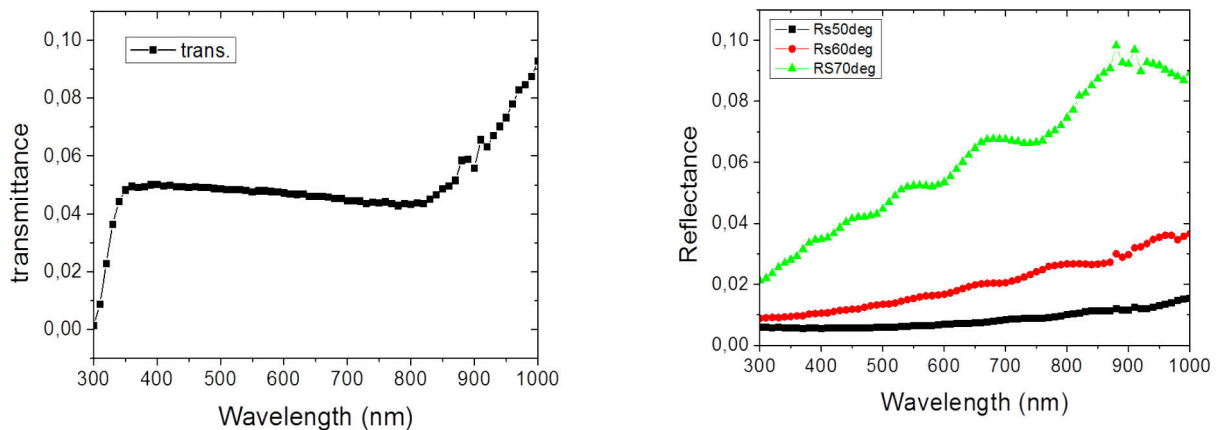


Figure 49 Ellipsometry results. Transmittance (left); Reflectance (right).

Micro-spot ellipsometry measurements carried out on the final dense material were performed by the group of the Department of Physics & CNR - Nanotec, University of Calabria, LICRYL (Liquid Crystal Laboratory), since the beam spot of the ellipsometer used by the group of the AMADeUs project has larger dimensions than the surface area to be characterized. From Figure 49 the silicon

dense material does not transmit at all the incoming light. Also by reflectance measurements, for different incident angles (50 to 70 degree), light is not reflected, just a low signal for the incident angle of 70 degree. These results suggest that the sample is able to absorb almost all the incident light on it.

### 3.2.2 Multichannel evaporator

As in the previous assembly using the unidirectional evaporator (Chip 2), we tried to assemble the silicon nanoparticles with the same technique but by changing the design of the channel. In this case the evaporator we used had a series of channels with the same length and thickness ( $L_0 = 7\text{mm}$ ,  $w_{\text{channel}} = 270\mu\text{m}$ ,  $h = 4\mu\text{m}$ ). We managed to obtain a well-organized material without any fracture in the dense material.

Using an optical microscope and the MATLAB software, we acquired every 5 minutes, images of the process of the assembly of the silicon nanoparticles within the individual channels. In fact, in Figure 50 we can see a clear and sharp front between the dense phase (black) and the liquid phase (gray).

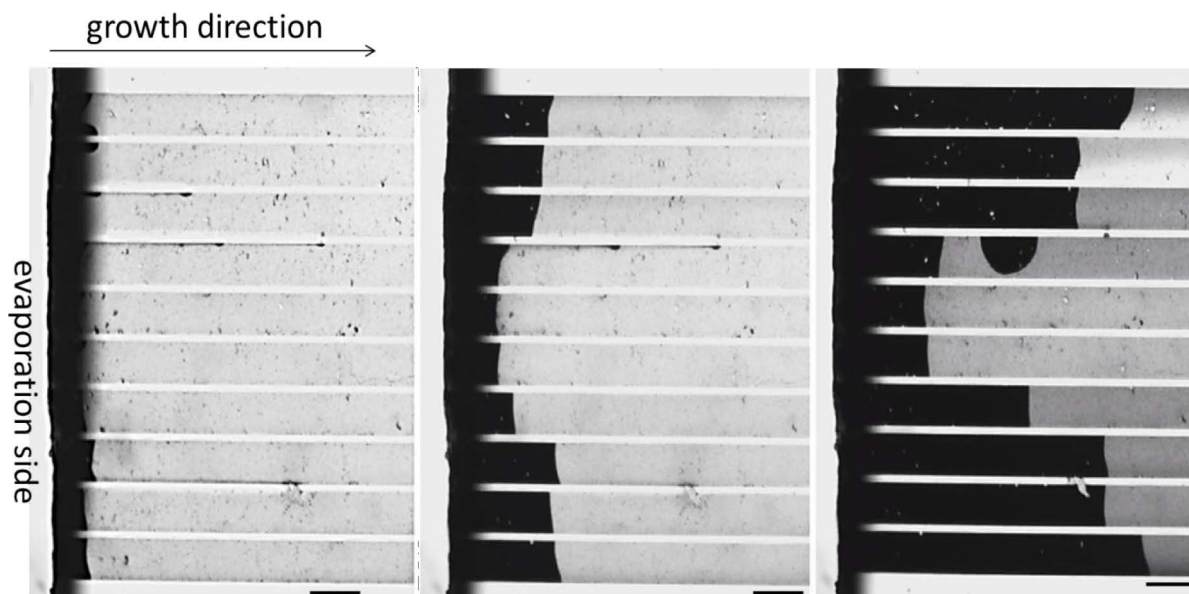
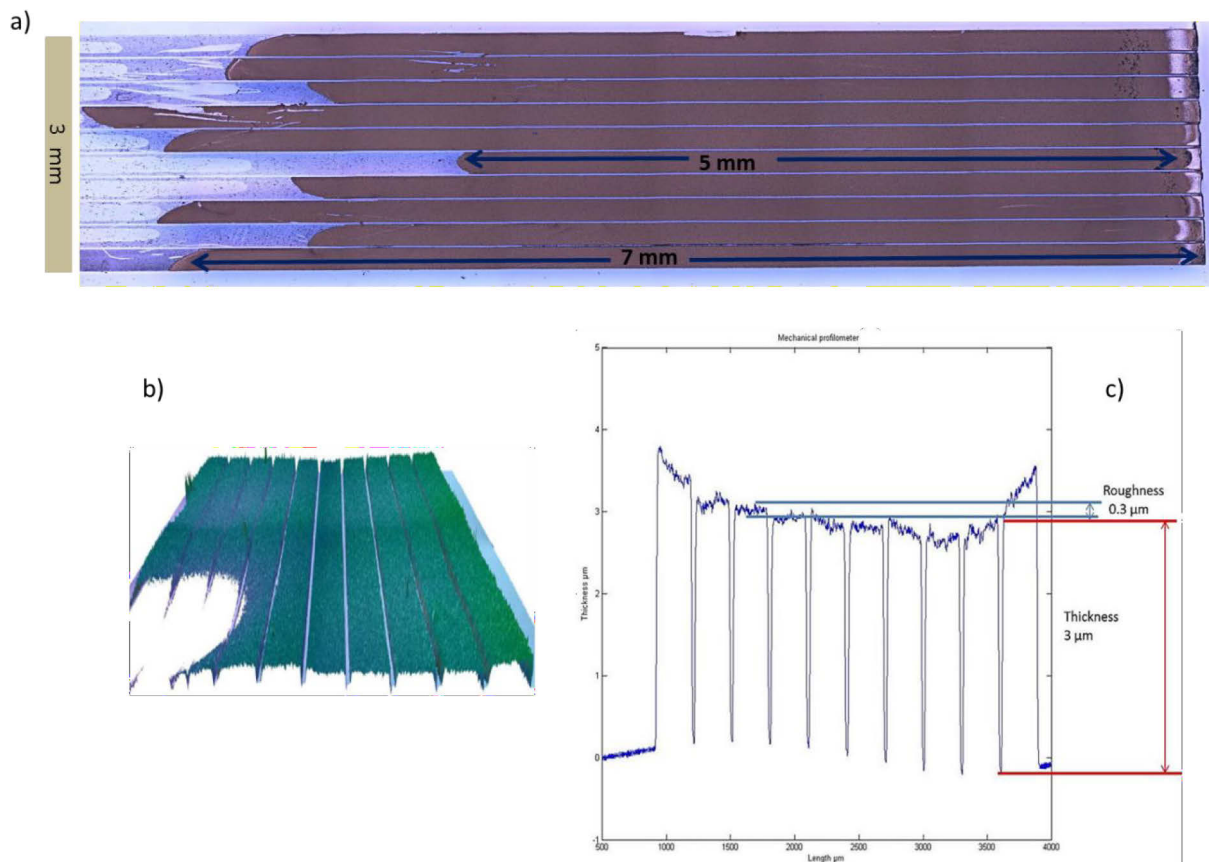


Figure 50 frame capture of the material front direction (scale bar  $300\mu\text{m}$ ).

After about 2 hours the silicon nanoparticles were assembled inside the channels. When the dense material was completely dry, it was then possible to remove the PDMS mold to recover the material and get its morphological and optical characteristics.



**Figure 51 optical profilometry. A) top view of the final material; b) 3D structure of the material; c) height profile**

In Figure 51 are shown the measurements using profilometry. Figure 51(a) shows an image of the final dense material by using optical profilometry and a 3D image showing the topography of the material (Figure (b)). Then it was possible to measure the height and roughness of the material (figure (c)):  $3 \pm 0.3 \mu\text{m}$ .

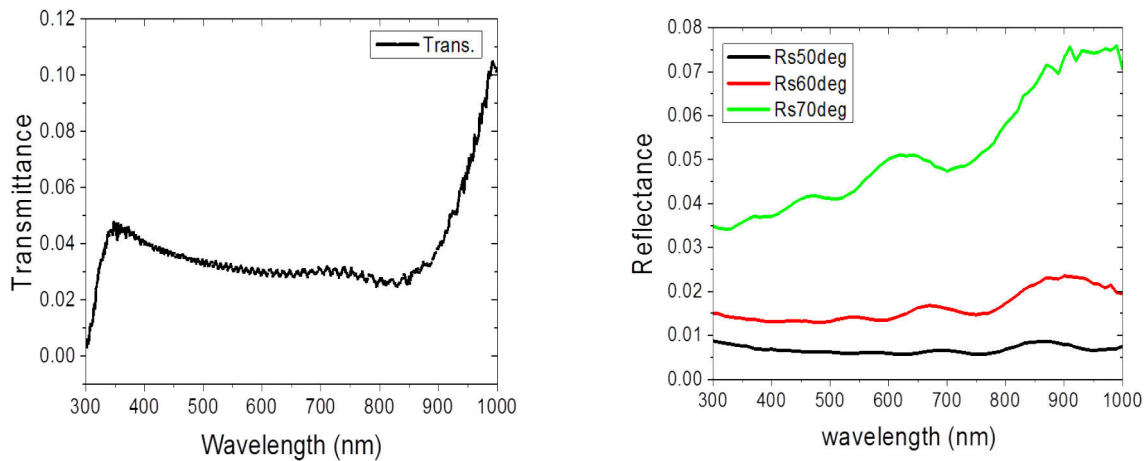


Figure 52 ellipsometry measurements, on the left the transmittance values in function of the wavelength; on the right the reflectance values obtain in function of the wavelength at different angle degrees.

From ellipsometry measurements, as in the case of the evaporator with holes, the material does not transmit and reflects almost all the incident light. In the following Figure 53 is reported the total absorbance (A) measured for both assembled materials.

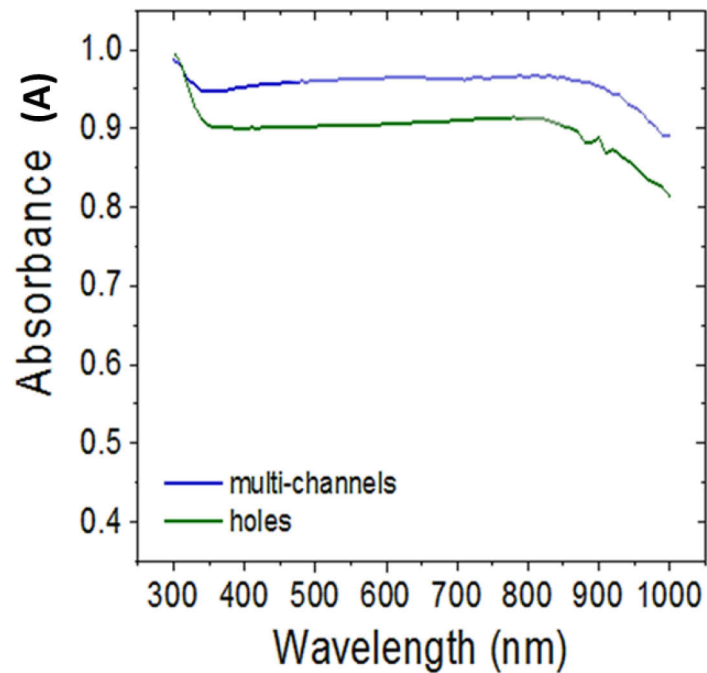


Figure 53 Total Absorbance in function of the wavelength for the silicon multi-channels and holes dense materials

The values of absorbance calculated by considering  $A = 1 - T - R$  are approximately equal to 1 in the UV-Vis region of the spectrum. So it means that the materials we obtained are able to absorb almost all the incident light.

### 3.3 Chip 3: Decoupled microevaporator

Although we have obtained well-assembled micromaterials with the above techniques, they do not fully satisfy the features initially listed like a large surface to perform optical characterization using standard ellipsometry, and bulk defect-free materials. So, we used the decoupled microevaporator (Chip 3) already described in chapter 2. By developing and using chip3 we are able to obtain a larger surface material and to control the materials failures. Figure 54 shows an image of the microdevice captured during the nanoparticles assembly showing the two zones, the pumping zone and the growth zone (top image) and the schematic side view of the microdevice.

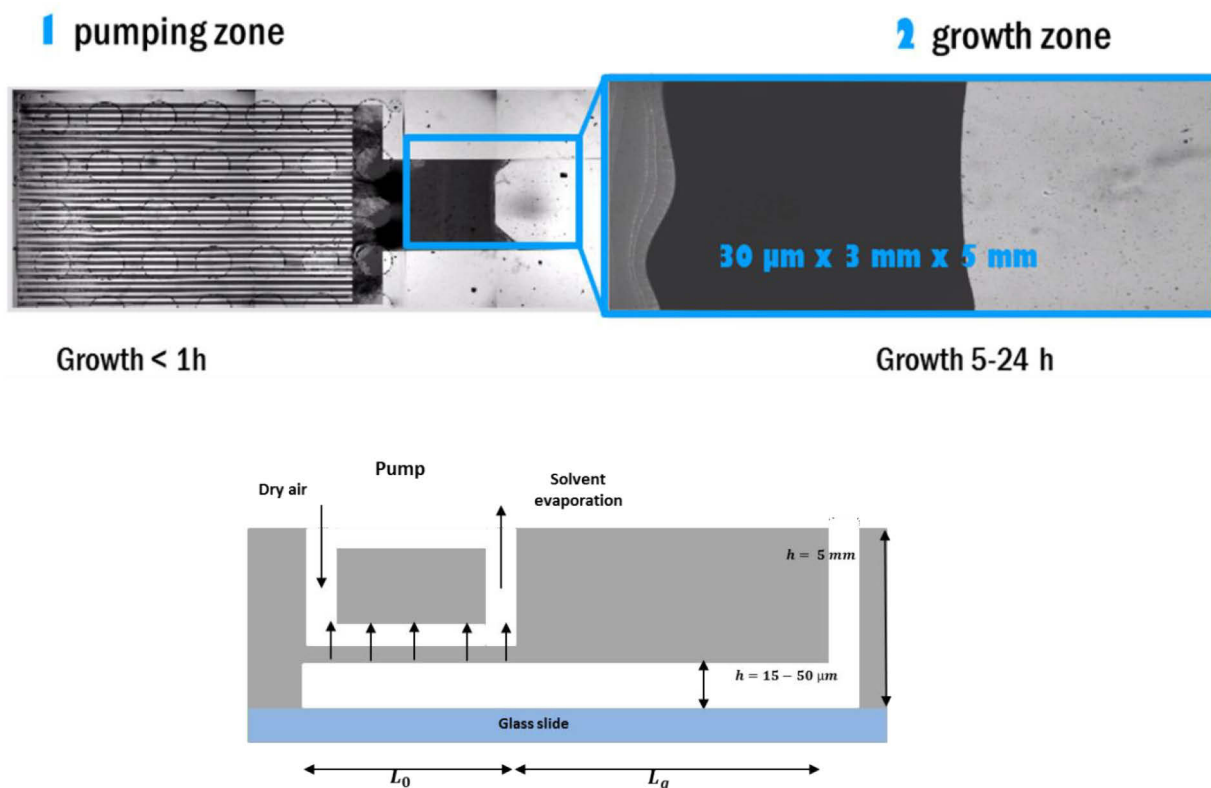


Figure 54 On the top the microfluidic device used for the nanoparticles assembling with the two different zones (pump and assembling chamber); above the schematic side view of the decoupled microdevice.

As mentioned previously in Chapter 2, this device consists of a series of thin channels ( $L_0 = 2\text{ cm}$ ,  $w = 100\ \mu\text{m}$ ,  $h = 25\ \mu\text{m}$ ) that are used to form a “filter” when filled by large colloidal particles, and a larger chamber for assembling the nanoparticles of interest ( $L_g = 1.6\text{ cm}$ ,  $w = 3\text{ mm}$ ,  $h = 25\ \mu\text{m}$ ). The filter made of latex particles ( $0.6\ \mu\text{m}$  in diameter) is assembled in the pumping zone of

the microdevice by using pervaporation. The formation of the filter with the large latex particles makes a dense material with a porosity smaller than the size of the nanoparticles of interest that will be assembled later. The fact that the interstitial pores are slightly smaller than the nanoparticles allows the solvent to continue to flow through them and then be extracted by a third element called “pump” using pervaporation through a thin PDMS membrane (right image in Figure 54). The pump is connected to a pressure controller that constantly injects dry air into the device to allow a fast extraction of the solvent, thus reducing the assembly time.

After the drying, the material can undergo fractures, due to the air entering inside the assembling chamber, causing mechanical stresses within the dense material. But in some cases, the fractures are due to the stresses imposed during the recovering step when the PDMS block is removed.

The device is initially connected to a pressure controller (Fluigent) by a tube connected to a syringe filled with the dispersion of nanoparticles, as shown in Figure 55. The tube connecting the dispersion to the chip is plugged to the inlet which, applying a constant pressure  $P_1$  of 50 mbar, allows the entire device to be filled with the dispersion and to extract any air bubbles inside it. The 50 mbar pressure is kept constant throughout the experiment to prevent a collapse of the membrane when a pressure of about 150 mbar is applied in the chip pumping area to induce a flow of dry air on top of the membrane.

When we apply the lower pressure, the latex dispersion starts to flow inside the microevaporator until it fills the channels and the chamber of assembly. Once the device has been filled, a second pressure  $P_2$  of about 150 mbar is set in the outlet of the pumping area. In this case dry air is injected and the evaporated solvent is pumped out of the device. In this way the assembly time is considerably reduced.

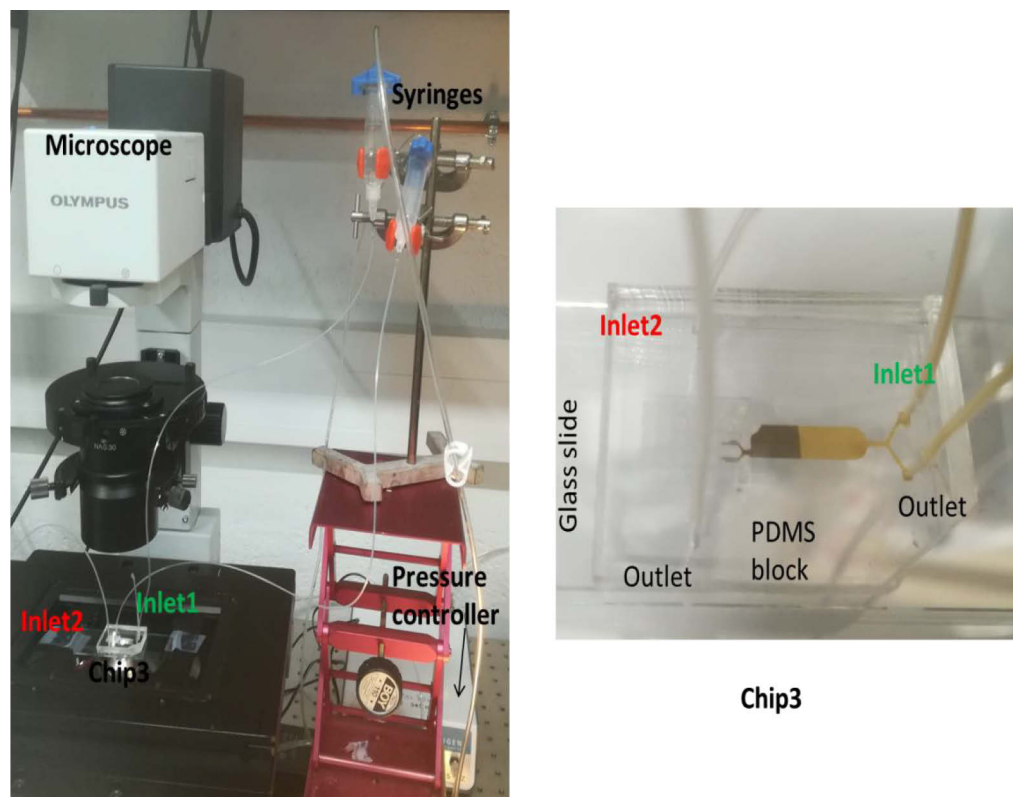


Figure 55 working setup; on left a photo of all the instruments used during the experiments with the chip3; on the right a zoom of the tubing connection between the chip3 and the pressure controller.

Using the optical microscope, we followed the concentration process of the latex colloids and of the nanoparticles.

First, we need to create a filter inside the pumping area. The filter is created by assembling latex nanoparticles of diameter about  $0.6 \mu\text{m}$  at an initial concentration 8% w/w. The formation of this filter takes about 2 hours.

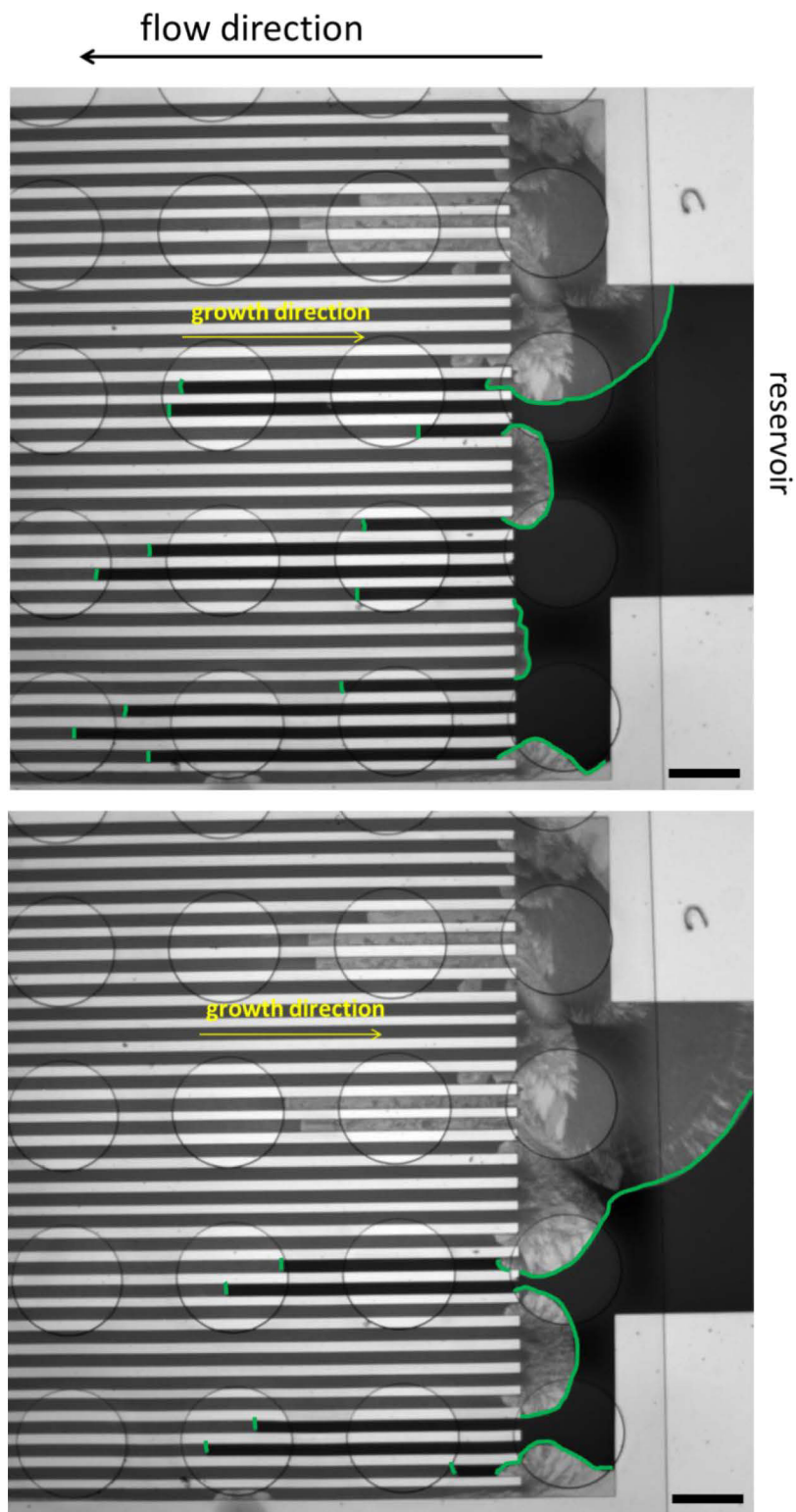


Figure 56 Capture of the channel during the evaporation process and the latex nanoparticles assembly. The front (green lines) between the liquid and crystal phase is sharp (in black the liquid phase in gray the solid phase). Scale bar 500 $\mu$ m

In Figure 56, the crystallization phase of the latex is shown over time. When the filter reaches the growth zone, the dispersion inside the device is replaced with the dispersion of interest. With this device the silicon nanoparticles and the N-podes presented in Chapter 2 have been assembled.

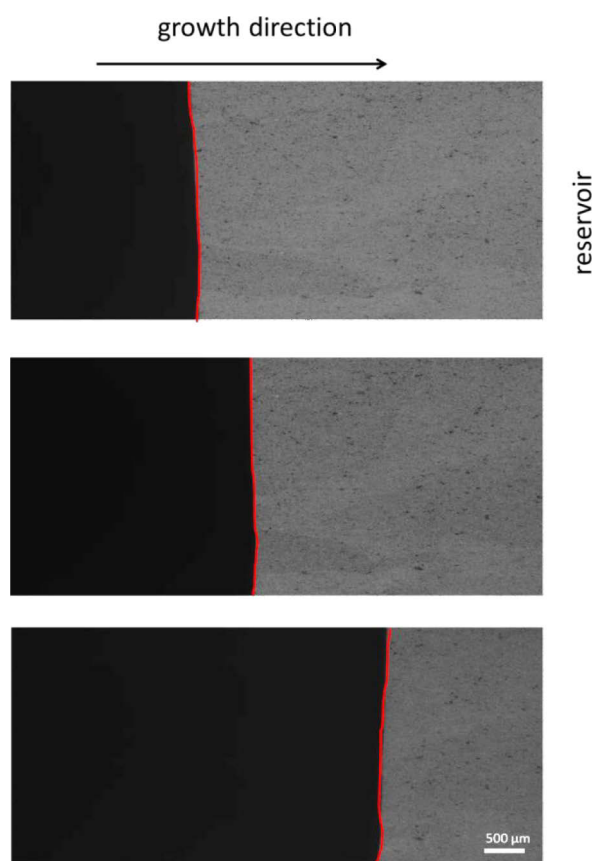


Figure 57 Capture of the channel during the silicon nanoparticles assembly. The red line shows the front between the liquid and dense phase inside the channel.

In Figure 57 are shown the silicon nanoparticles assembly inside the growth chamber. It is possible to observe the formation of the dense material during time. In fact to obtain this material the experiment lasts around about 10 hours. Once the dense material is dried it is finally recovered for a detailed characterization.

### 3.3.1 Characterization

Using the decoupled microevaporator Chip 3, we obtained two different dense materials. For both materials it was possible to obtain a complete characterization (profilometry and optical characterization).

### 3.3.1.1 Silicon dense material

After the assembly of the silicon nanoparticles, the final, dense material was recovered from the mold in PDMS. Figure 58 shows the material left inside the mold in PDMS (on left) and an optical microscope acquisition (on right). As can be seen from the optical microscope acquisitions, the material displays several cracks inside its bulk. Even though inside the mold in PDMS and the several fractures the sample presented, it was possible to characterize the material. Micro-spot ellipsometric measurements were also performed by LICRYL, although the characterization surface is significantly reduced by the presence of fractures that occurred during the drying process.

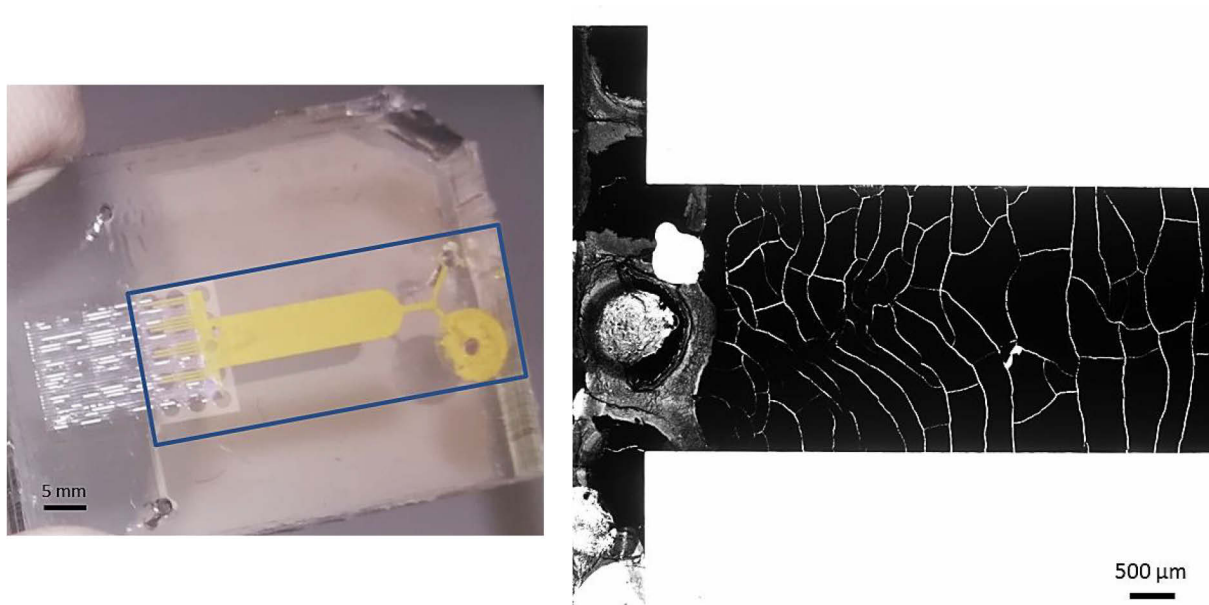


**Figure 58** Material recover after the assembled process (left); optical microscopy acquisition of the material after it has been recovered full of cracks appears during the drying step.

Successively the material inside the PDMS mold was characterized by profilometry to measure the final height of the assembled material and its surface roughness. Figure 59 below shows that the final material has a thickness of about  $16 \pm 1.5 \mu\text{m}$ .

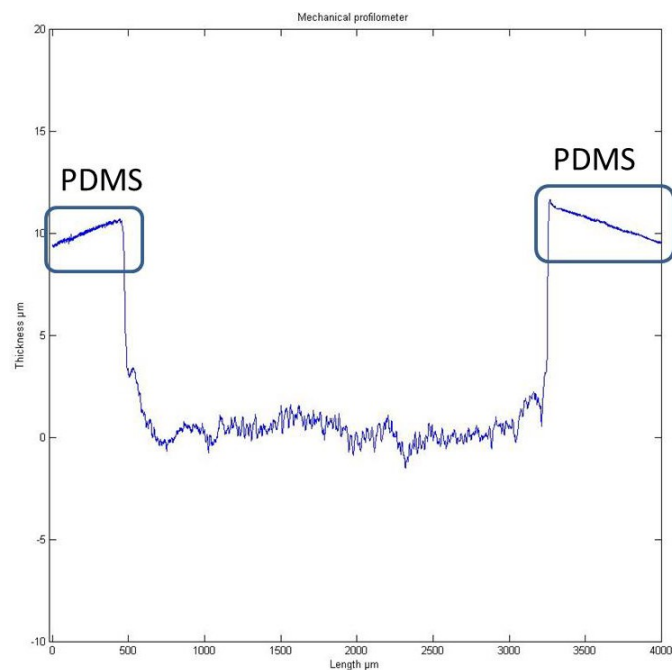


**Figure 59 Profilometry acquisition.**

The final height of the material was obtained by subtracting from the initial height from the lithography channel ( $h_i = 26 \mu\text{m}$ ) and the distance between the surface (roughness) and the edge of the PDMS mold. A small portion of the material was used to acquire SEM images and get an idea of the structure of the dense material after assembly.

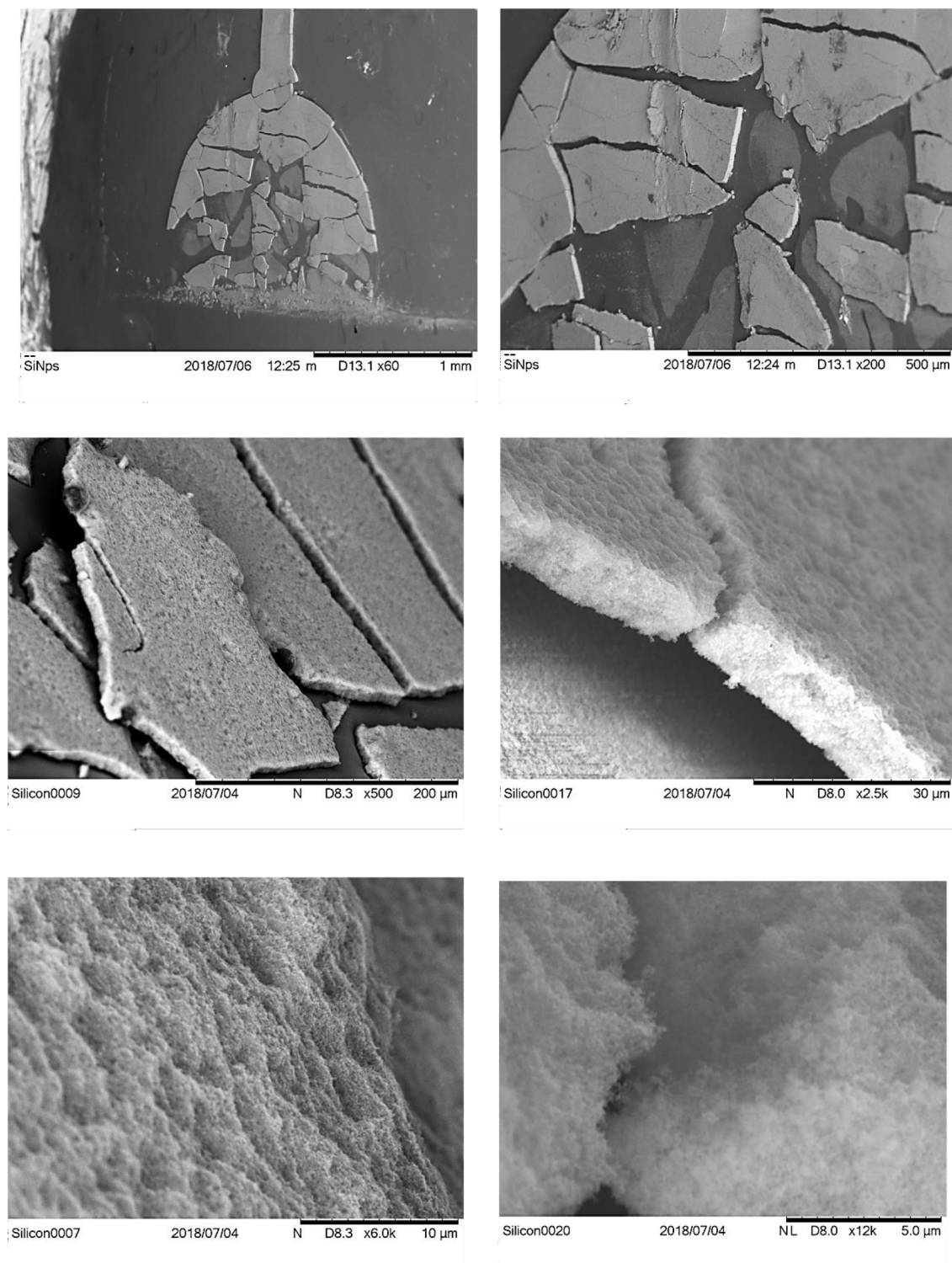


**Figure 60 SEM images of the PDMS mold cross section.**

From the SEM images it can be seen that the material has a homogeneous and dense structure even if many fractures appeared during the drying process and also during the PDMS mold cutting. In

addition, it can be noted that the surface roughness is high, as confirmed by the previous profilometry measurement.

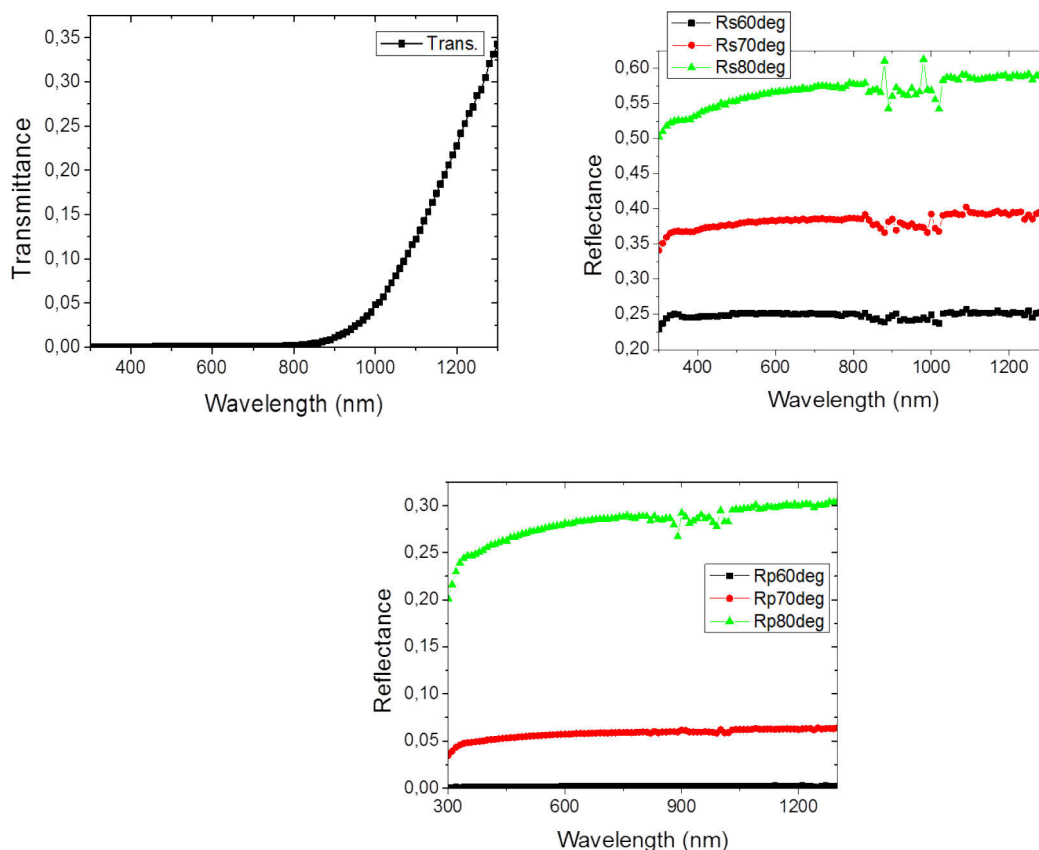


Figure 61 ellipsometry characterization.

From the ellipsometric measurements of the silicon material it can be seen that the material does not transmit light up to a wavelength of about 800 nm. For higher wavelength, the material displays a slight increase in transmission (top left). The reflectance is very low for different angles with perpendicular incidence ( $R_s$ ) and parallel incidence ( $R_p$ ) light. This may indicate that the material consisting of silicon nanoparticles absorbs almost all the incident light.

Due to the fractures in the material, it was not possible to carry out any other measurements in order to prove that the assembled material could be considered as a metamaterial. In fact, a new material was assembled.

So, after the assembly of the silicon nanoparticles, the material was removed from the PDMS block. On the dense material, profilometry and SEM measurements were carried out. In Figure 63 is shown the final material after the silicon nanoparticles assembly.

### 3.3.1.2 Optical microscopy and SEM

After the assembly and the removal of the final material, the material was observed with an optical microscope and SEM images were acquired.

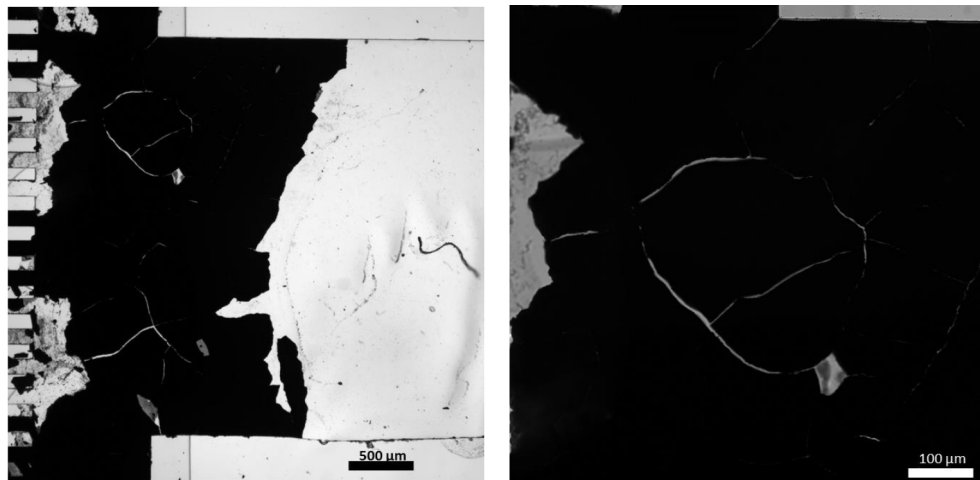


Figure 62 Images acquired by optical microscope

In the figure above (optical microscope) it is observed that the sample presents some fractures. The fractures are large enough to do not preclude any further optical characterization. During the final material recovery, most of the material remained in the PDMS mold. Thanks to a portion remaining on the glass substrate, it was possible to observe the material from the point of view of the internal organization of the nanoparticles during the assembly process by using SEM.

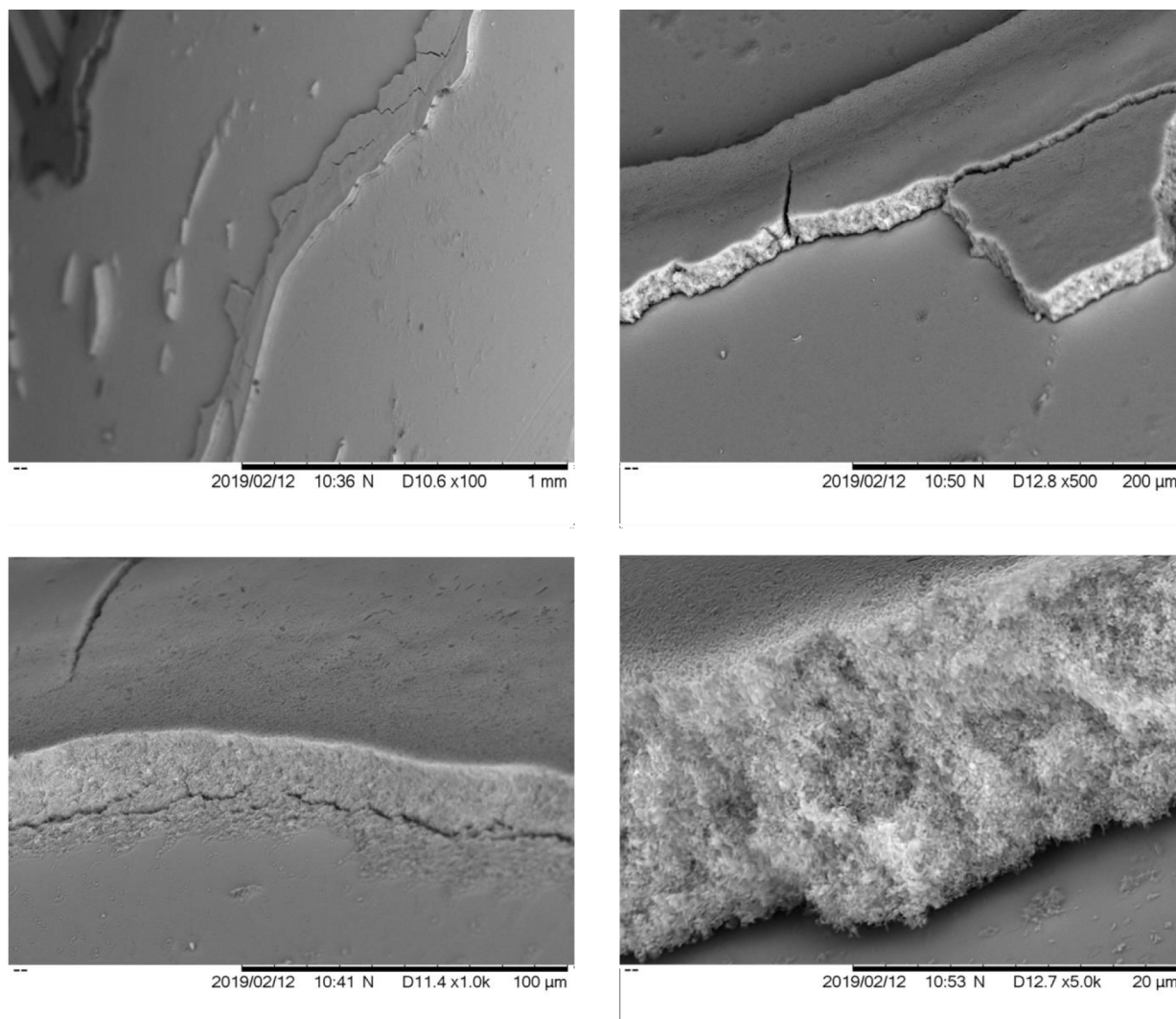


Figure 63 SEM images at different magnifications

As can be seen in Figure 63, the final material has a very smooth surface and a compact and dense structure. The low surface roughness is confirmed by profilometry. The final material obtained shows a final height of about  $25 \pm 0.3 \mu\text{m}$ , i.e. a roughness of about the particle size. For this sample it was not possible to run optical characterization for some technical issues due to the PDMS thickness that was thicker than the ellipsometer stage.

The same experiment can be reproduced using different types of nanoparticles. In the next paragraph, we show the results for the N-podes assembly using the “decoupled microevaporator” Chip 3 described before in 2.8.3 Chip 3: decoupled microevaporator.

### 3.3.3 Large scale N-podes

The same assembly procedure was used for the hexapodes nanoparticles. Initially, the filter in the pumping zone was formed using again large latex colloidal particles. Once the filter was assembled,

the dispersion was changed to the nanoparticles of interest. Still using the optical microscope and the Matlab image acquisition software, it was possible to follow the progress of the assembly inside the microchannel.

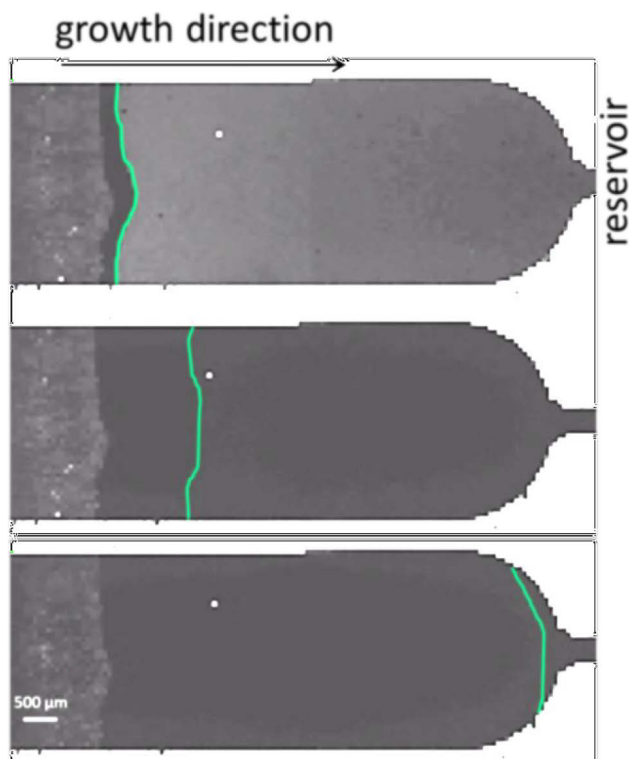


**Figure 64** images acquired during the hexapodes particles assembly. The grey zone (left) next to the black front is the latex particle filter already assembled. The green line shows the particles growth front during the pervaporation process inside the microfluidic channel.

In Figure 65 it is possible to see the displacement of the front of the assembled nanoparticles at the interface between the liquid and dense phase. The image is composed by an acquisition of two frames at two different locations of the device with a time delay of 15 minutes between one composite image and the other. In the figure we can distinguish the filter composed of the latex nanoparticles (left), the hexapodes that begin to assemble in the dense phase (front indicated in green) and in light grey the liquid phase of the dispersion (right). The assembling time was about 1 day.

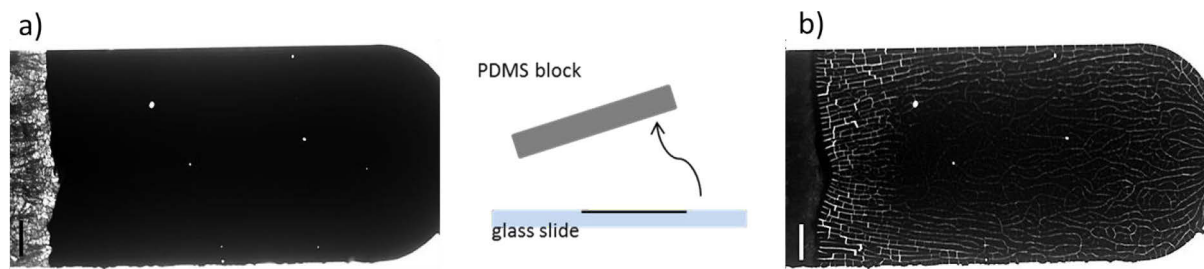


**Figure 65** Images of the dense material a) inside the microchannel after the assembly and the drying step; b) final material recovered after the PDMS block removing. After the recovery material many failure appears in the material bulk (scale bar 500  $\mu\text{m}$ ).

When a sufficient length of material is reached inside the assembly chamber, the pressure is set to zero and the tube is disconnected from the inlet. In this way, air invades the entire chamber and dries the dense material, which is then ready to be removed from the PDMS block (Figure 65). The image above shows that there were no fractures in the material after the assembly process. After the device has been opened, the material, observed at the microscope, displays a lot of fractures, which may have been created during the mechanical action of removing the PDMS mold.

### 3.3.3.1 Profilometry, SEM

Even if the final result did not allow us to carry out the necessary ellipsometric characterizations, the material was still characterized by measuring its roughness and thickness and also SEM images were acquired to observe the state of assembly of the nanoparticles.

The following Figure 66 shows the results of the optical profilometer. In figure a and c are shown the topographies of the material, while figure c is a full width scans of the material. The profilometer measurements show that the material has a height of  $(14 \pm 1) \mu\text{m}$  and that the surface is not perfectly flat, which implies that the material undergoes surface deformations. Such deformations, sometimes large, could lead to problems for further optical characterization. The final height of the material is  $14 \mu\text{m}$  with a roughness equal to  $1 \mu\text{m}$ .

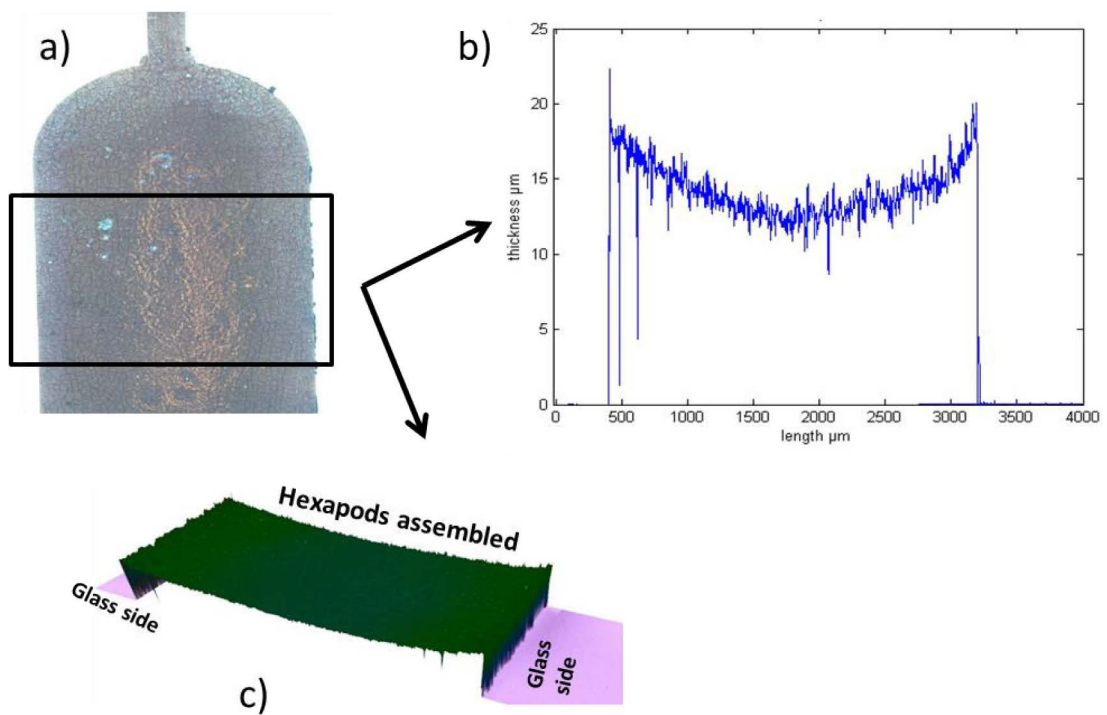
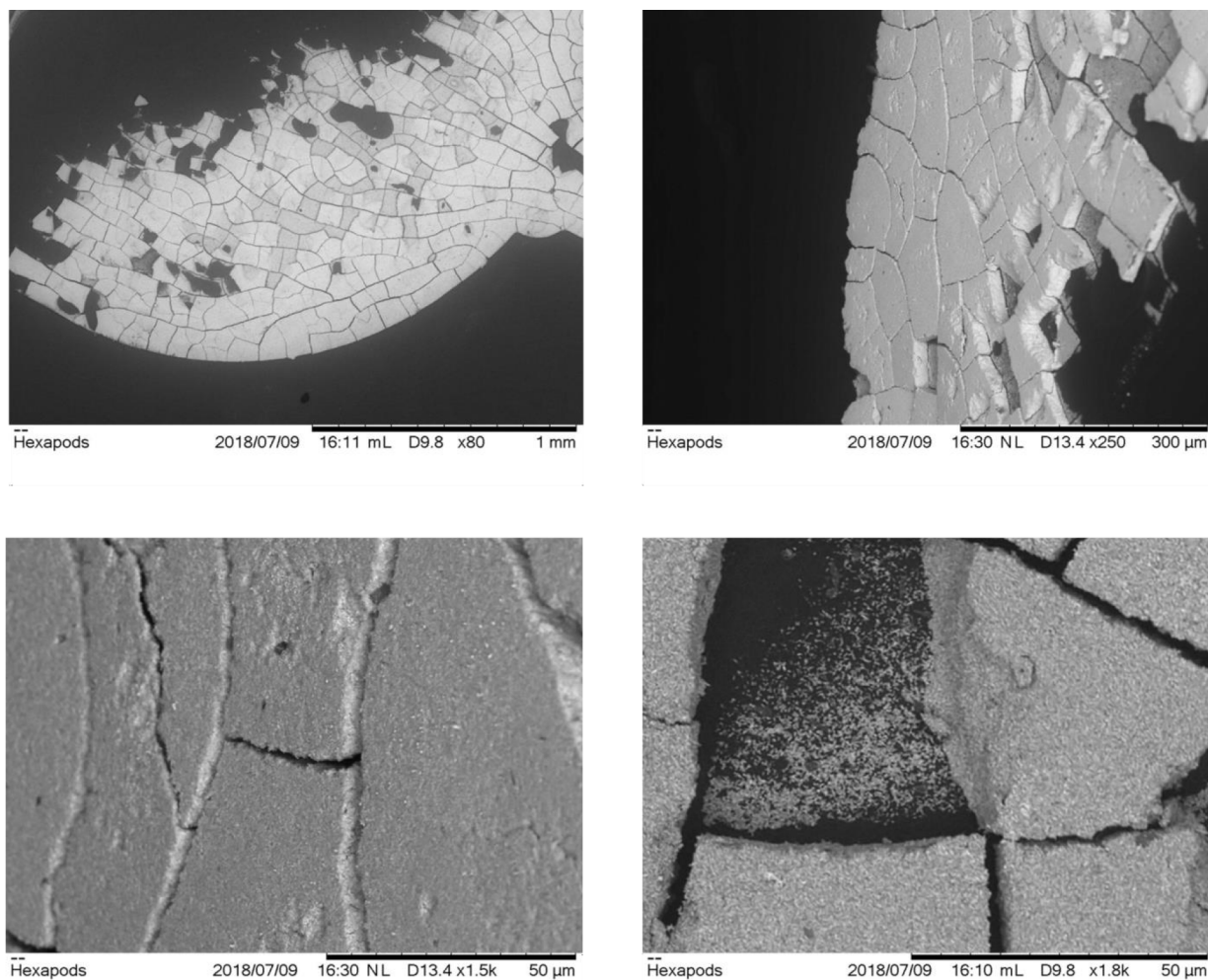


Figure 66 Profilometry acquisition. a) Real image of the dense material; b) height acquisition and c) 3D representation on a portion of the material.

From the SEM images we can see that the material is well organized and has a smooth surface. This gives us a further confirmation of the data acquired by the profilometer, and that it is possible to assemble different kinds of nanoparticles.



**Figure 67 SEM images acquired for the hexapode dense material**

The same assembly technique was used with the dodecapode nanoparticles. In the Figure 68 below, the entire assembly process is shown, starting from the constitution of the filter using latex nanoparticles and then switching it with the dispersion of dodecapodes. Using the MATLAB software, it was possible to obtain a complete video of the assembly phase of the filter and the dodecapodes up to the drying phase.

The following Figure 68 shows an image of the growth zone during the assembly phase of the nanoparticles. Starting from the time  $t = 0$  until the end of the process. The assembly process can last from 5 hours to one day.

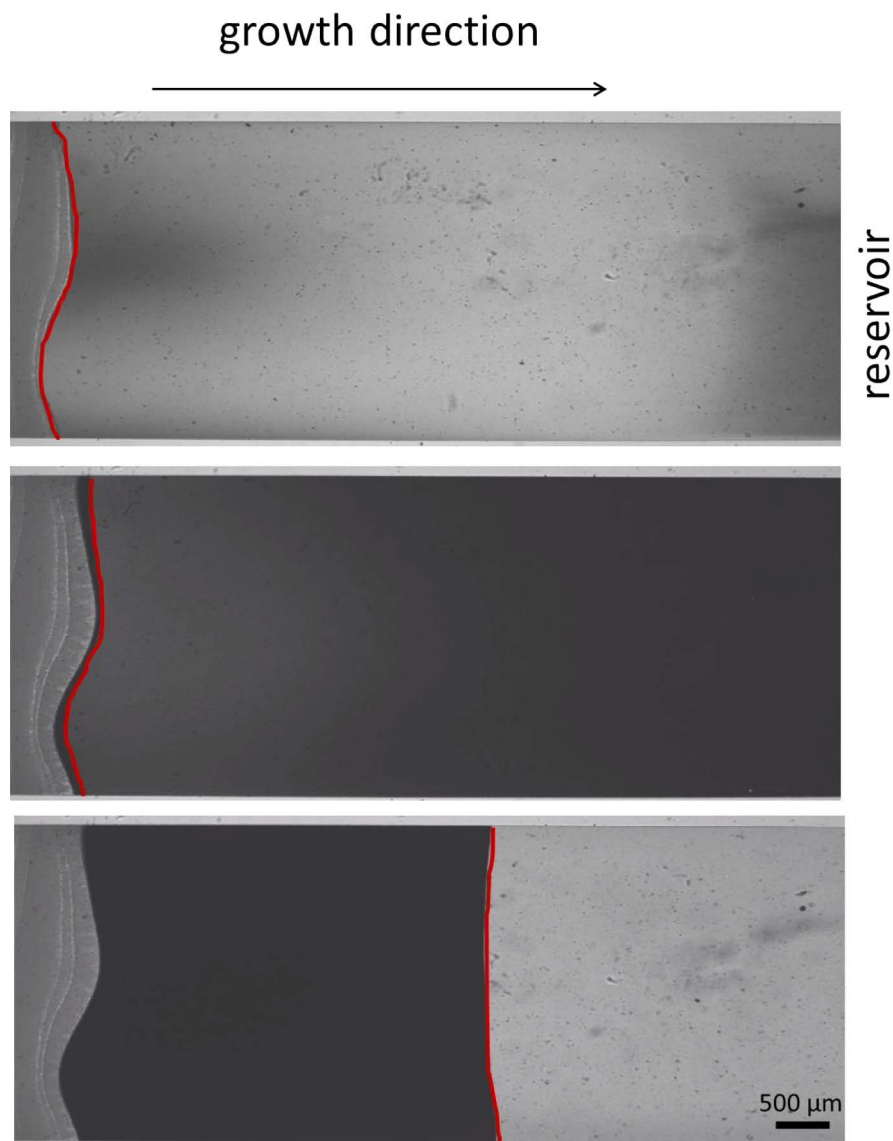


**Figure 68 Acquisition of a single channel captured during the assembling process. With the red line it is define the front between the solid phase and the liquid phase**

When the material dried out, it was recovered and observed using SEM techniques. During the removal of the PDMS block, the material remained inside the PDMS mold. It also displayed numerous fractures. From the SEM images, one can see the high degree of packing of the nanoparticles.

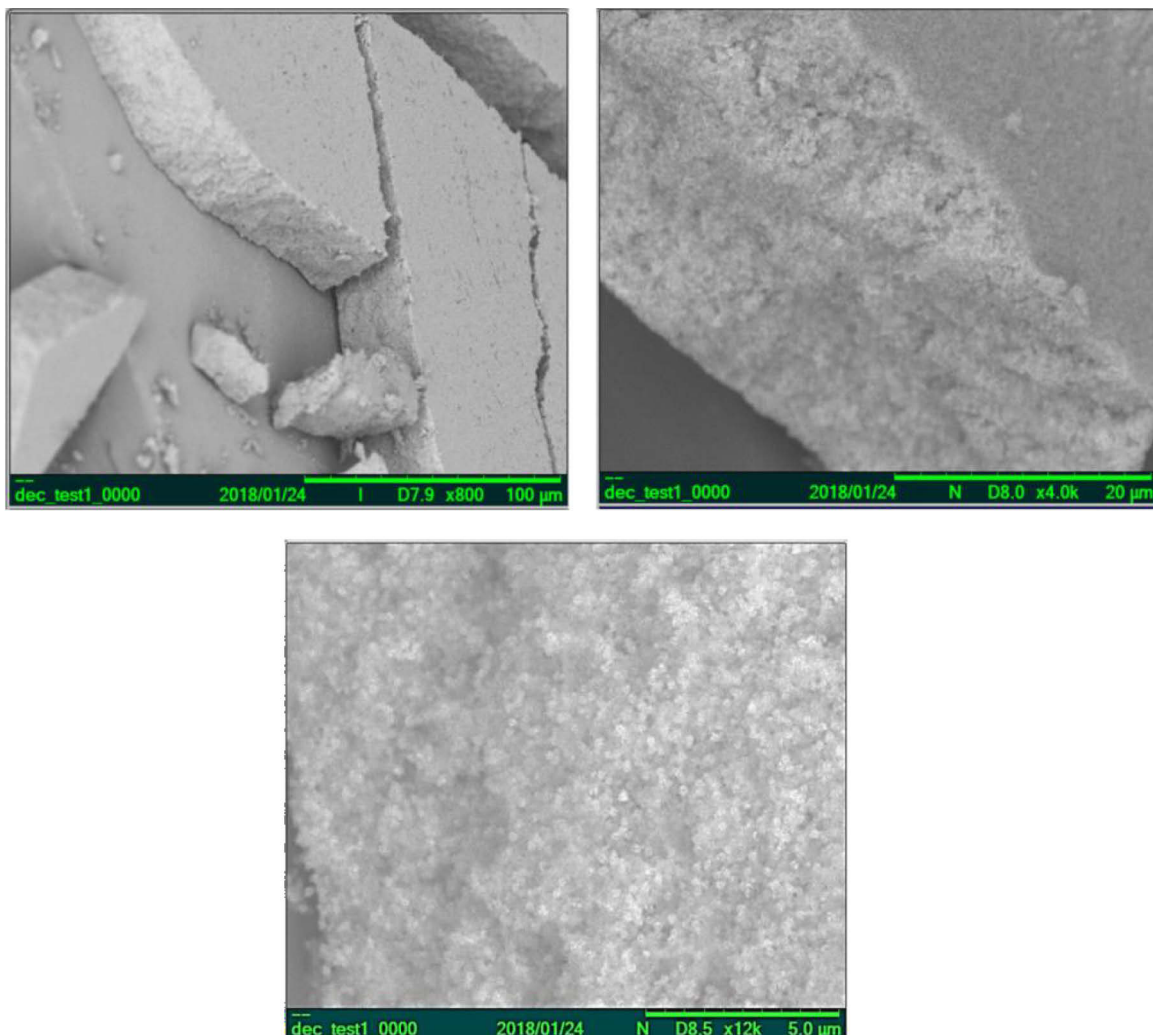


Figure 69 SEM images of the dodecapodes dense material after been recovered.

The final material was measured to have a height of  $20 \pm 1 \mu\text{m}$ .

Until now we have seen that it has been possible to fabricate different materials, with different types of geometries. Using the decoupling microfluidic device it is possible to obtain materials with dimensions of 3 mm x 2 cm, the only problem that has occurred in each experiment is the formation of cracks in the material before and during the removal of the mold of PDMS. To overcome this problem, we have tried to infiltrate the material with different types of polymers to avoid fractures.

### 3.4 Infiltration

The infiltration process was used to prevent the formation of fractures in the solid material. As already mentioned in Chapter 2, the nanoparticles cannot be covered by the polymer, as they would slow down or completely block the flow of solvent inside the channel, therefore preventing the growth of a material by pervaporation. The strategy we propose is to make the material (filter made of latex particles and the micromaterial made of the nanoparticles of interest, as in Figure 69

above) by the method described above, and then inject a dilute polymer solution into the microchannel. The polymer is transported along the entire length of the channel as the solvent is pumped out, therefore filling the pores of the colloidal material, and preventing hopefully the formation of fractures. However, the refractive index of the polymer must not in any way affect the optical properties of the final metamaterial. The three polymers we tested were polyvinylpyrrolidone (PVP,  $n = 1.52$ ), polyvinyl-alcohol (PVA,  $n = 1.48$ ) and di-acrylate polyethylene glycol (PEG-DA,  $n = 1.47$ ).

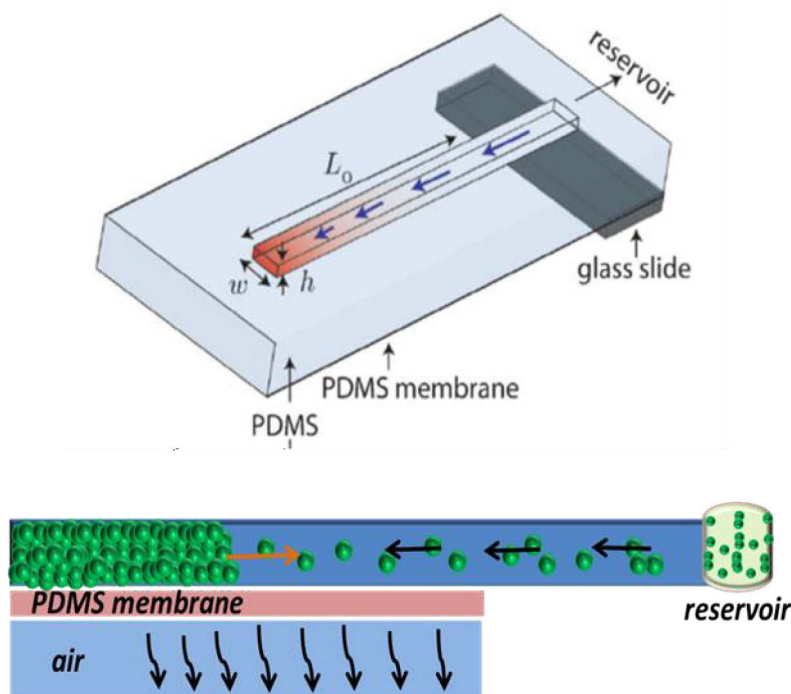


Figure 70 3D reproduction of the membrane microevaporator (top); channel side view of the microevaporation during the pervaporation (bottom).

These three polymers were tested using a membrane microevaporator having 5 different channels (Figure 70) with the same length but different width ( $L_0 = 1$  cm;  $w = 30 \mu\text{m}-60 \mu\text{m}-90 \mu\text{m}-120 \mu\text{m}-300 \mu\text{m}$ ;  $h = 30 \mu\text{m}$ ). In the following paragraphs we will show some of the results obtained during the trials using the three different polymers. The aim of the test is to reproduce the conditions of the chip including the filter zone and the growth zone of the nanoparticles under study, see page 49, and also to obtain shorter evaporation times.

### 3.4.1 PVA

PVA is a biodegradable imitation of natural polymers used in paper coating and textile sizing. It is used for various industrial applications to enhance the mechanical properties of films because of its compatible structure and hydrophilic properties. It is ductile but strong, and flexible.

Knowing the properties of PVA, we started with preliminary tests and see if it could infiltrate the solid material. Initially, we tried to infiltrate only the material consisting of latex nanoparticles. As for the previous experiments, all channels were initially filled with a latex dispersion. After the formation of the dense material, a 1% polymer aqueous solution of PVA 13k Mw was injected as shown in Figure 71 .

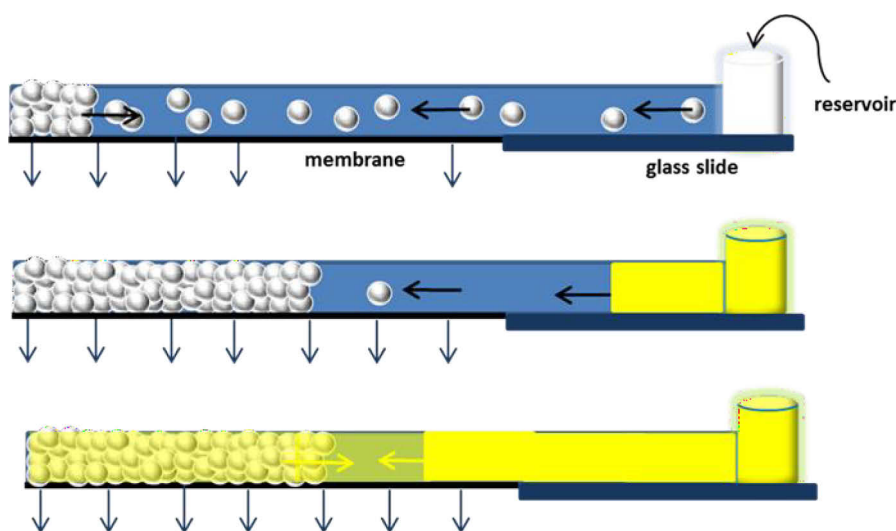


Figure 71 sketch of the assembly phase of the latex nanoparticles and the later step of polymer infiltration

As in the previous case, an optical microscope was used to follow the assembly process of the nanoparticles and make simpler the visualization of the front between the liquid phase and the dense phase. By stitching two frames acquired by using a digital camera using programming software (MATLAB) the colloidal assembly inside the channels was monitored. The time delay between each image was about 5 minutes. As the channels were smaller and the dispersion was highly concentrated, it was difficult to initially identify the front between the liquid phase and the solid phase. To overcome this problem, the image acquisition was carried out in the dark and by placing a lamp parallel to the microdevice, thus collecting only the scattered light from the latex nanoparticles.

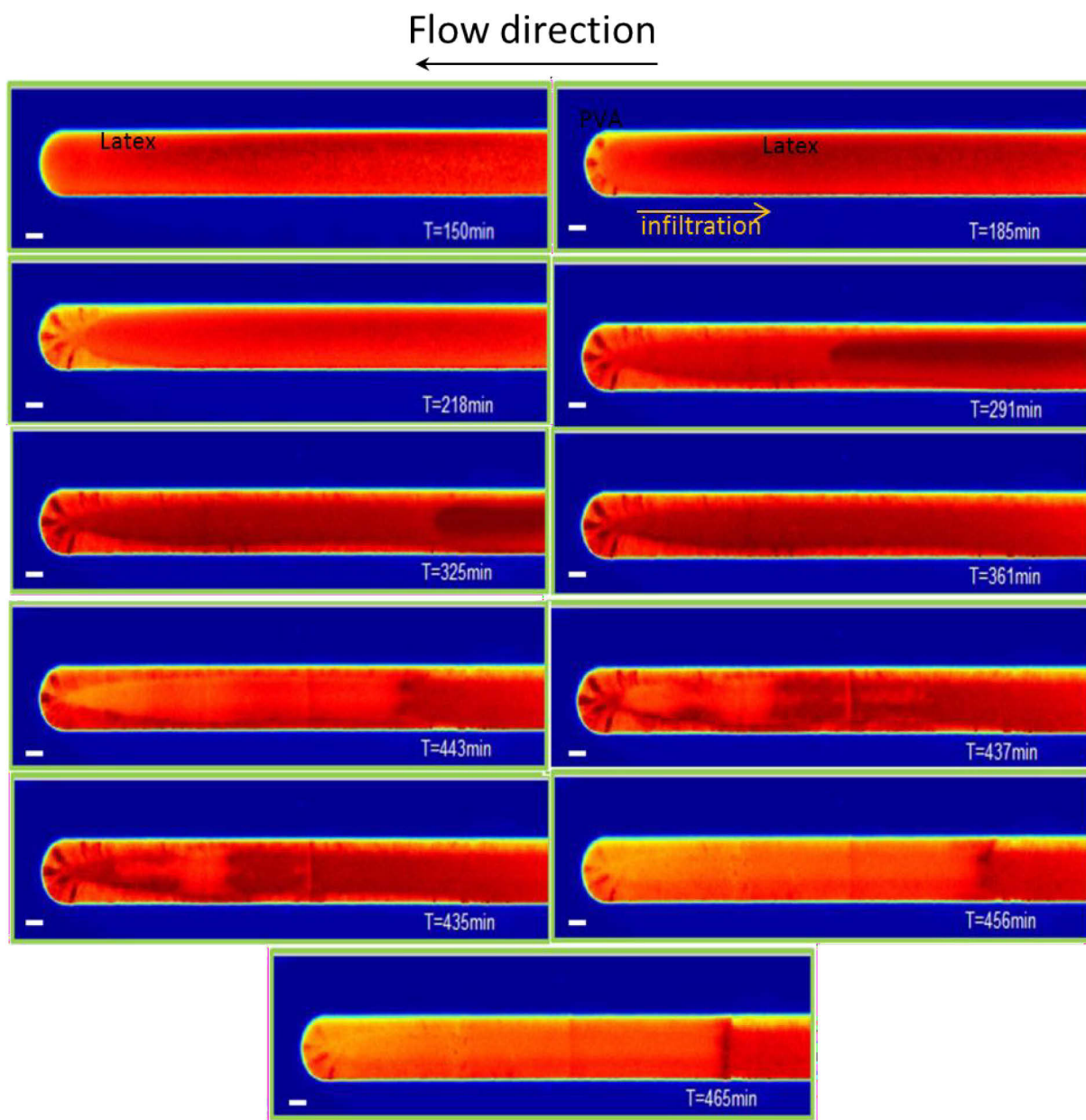


Figure 72 Single channel zoomed in to follow the particles assembly and the infiltration process (scale bar 100  $\mu\text{m}$ ).

To get a better view of the assembly and infiltration process inside the channels, we zoomed in on a single section of the larger channel. Figure 72 shows the assembly of the latex nanoparticles and in the following images the moment when PVA enters in the porous structure formed by the latex and it's spreading inside the array of latex particles. In the last image we can see a front moving towards the reservoir. The front represents the interface between the solid made by the latex particles and the PVA that infiltrates into the solid material.

Again using the MATLAB software we have converted the grey scale to a color scale to enhance the contrast because the high latex concentration, making possible to follow the front between the

dense and liquid phase during the particles assembly. In fact, as we can see from Figure 73 below, we can follow the formation of the dense latex material and the growth inside the channel and then the infiltration process of the PVA. When the PVA begins to flow through the porous matrix, made by the latex nanospheres assembly, the refractive index of the material changes. As the refractive index of the PVA is close to the PDMS refractive index, the channel seems to disappear completely where the channel is only filled with the polymer solution (Figure 73).



**Figure 73** Images acquired at the end of the experiments. All the channels are filled with the latex assembled particles (in white) and infiltrated with the PVA solution.

At the end of the assembly and infiltration experiment we did a cross section of the micro evaporator to see if the polymer had infiltrated the structure made by the latex colloids. In this way it was possible to acquire several images for each channel by using SEM.

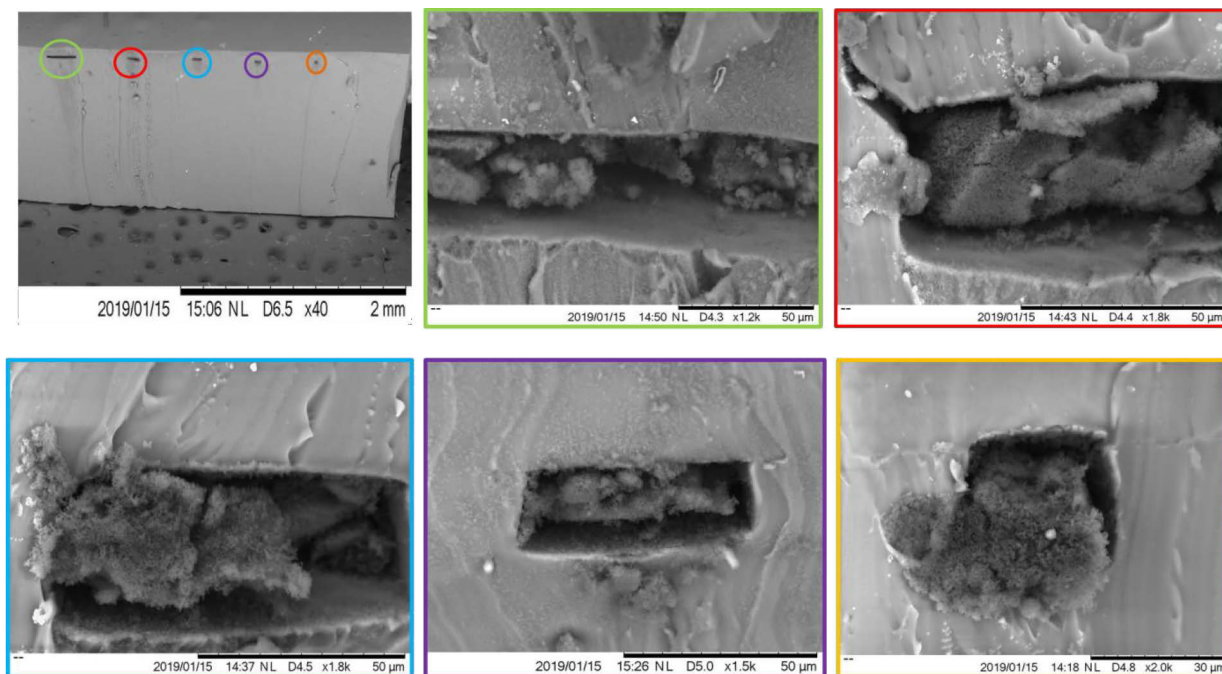


Figure 74 SEM images of the channels cross section.

From the SEM images one can observe that the material is infiltrated but at the same time it was more fragile, in fact each material displays fractures. Some of the fractures were already present after the final drying stage before the device was cut.

### 3.4.2 PVP

PVP in solution has excellent wetting properties and readily forms films, which makes it a good candidate for coatings or as additive to coatings.

Knowing the properties of PVP, we started with the preliminary tests. As above, all channels were initially filled with a dilute latex dispersion. After the formation of the dense material, the 1% polymer solution of PVP (10k  $M_w$ ) was injected as shown in Figure 75.

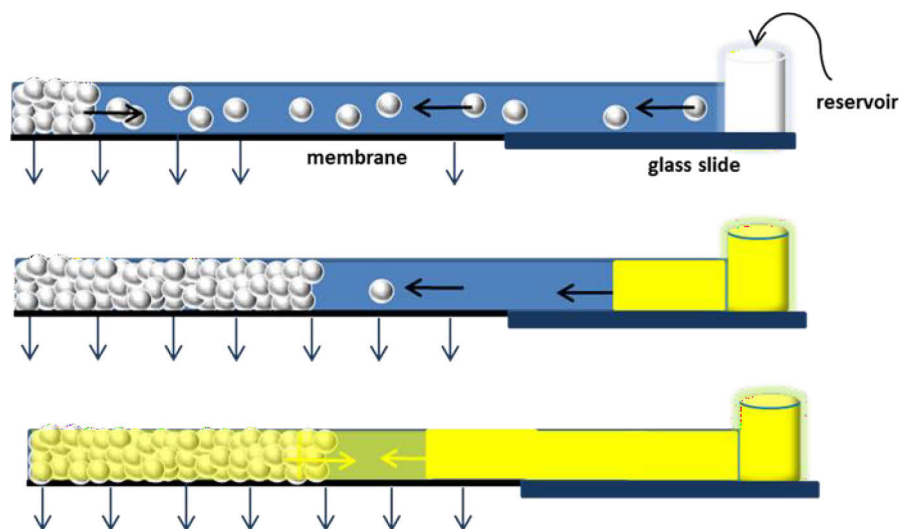


Figure 75 sketch of the assembling and infiltration process inside the microchannel

As in the previous case, an optical microscope was used to follow the assembly process of the nanoparticles and visualize the front between the liquid phase and the dense phase. The image acquisition during the experiment was made by acquiring two frames acquired by using a digital camera and using a programming software (MATLAB). The time delay between each image was about 5 minutes.

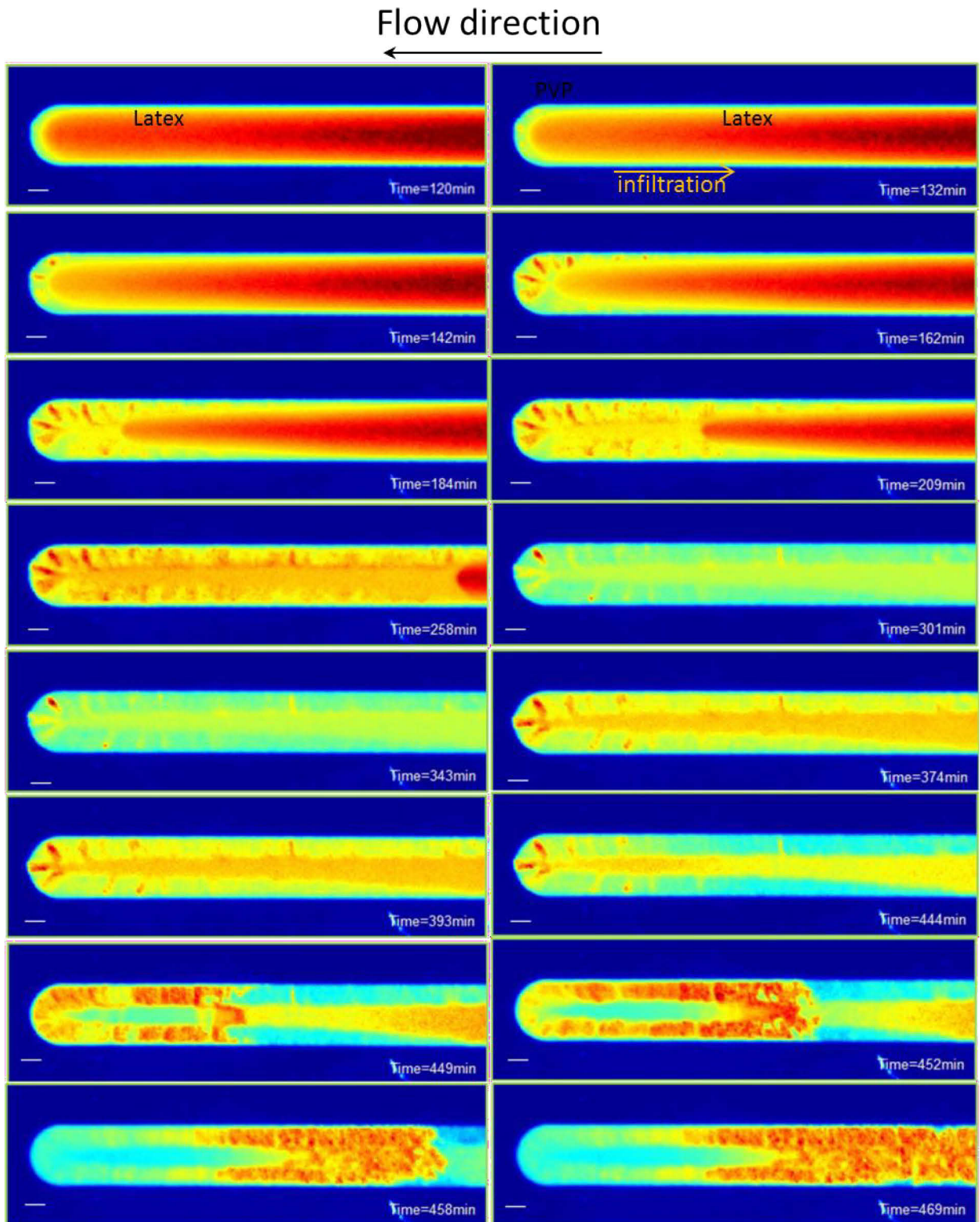


Figure 76 Single channel zoomed in to follow the particles assembly and the infiltration process (scale bar 100 $\mu$ m).

Figure 76 shows a zoom of the largest channel showing in the first image the assembly of the latex nanoparticles and in the following three images the moment when PVP enters the porous structure

formed by the latex and its spreading inside the array of latex particles. In the last image we can see a front moving towards the reservoir. The front represents the interface between the solid made by the latex particles and the PVP that infiltrates into the solid material.



**Figure 77** Capture of the end of the infiltration experiment. The white part is the latex material assembled and the dark part represents the filling of the channels by PVP.

Also in this case, when PVP infiltrates into the solid material, there is a considerable difference in the refractive indices of latex, PDMS and polymer. In fact, as shown in Figure 77 at the end of the assembly and infiltration processes, the solid channels only with PVP are transparent, as the refractive index of PVP is close to that of PDMS. This confirms that PVP has infiltrated the solid material. For further confirmation, also in this case we made a cross section of the device to observe each channel using SEM.

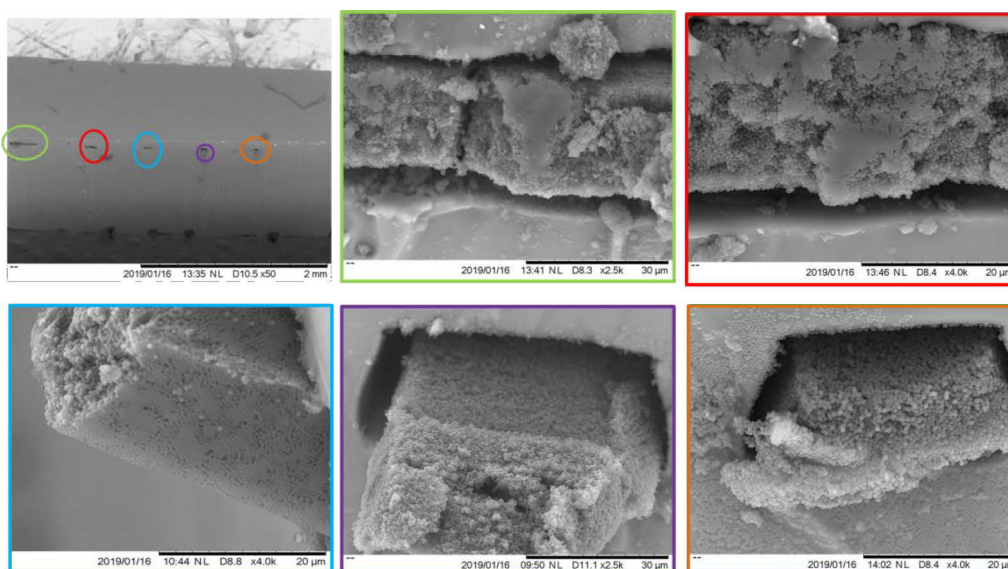


**Figure 78** SEM images acquired for each channel after the cross section of the microdevice.

From the SEM images, it is possible to see that the material displays a better organized structure. Not all channels have been infiltrated with the polymer solution. But in the case of the larger channels, the presence of PVP covering the latex particles is clearly visible. The nanoparticles are probably covered by a very low amount of PVP compared to other channels. One reason may be that during the exchange between the dispersion of nanoparticles and the polymer solution, air entered into the microdevice, thus causing a drying of the dense material and consequently also stopping the infiltration of PVP.

### 3.4.3 PEG-DA

Hydrogels are three-dimensionally cross-linked networks of polymers that can be swollen by large quantities of aqueous solutions. Some of them have also shown abilities to respond to various external stimuli such as temperature, pH, solvent, ionic strength, and electric field, or to combinations of these stimuli. One polymer commonly used to form hydrogels by photopolymerization is PEG-DA. Recent studies have been shown that high purity PEG has can be crystalline without forming hydrogels or gels. In our case we used PEG-DA in its pure state to avoid any changes into the final dense material optical properties.

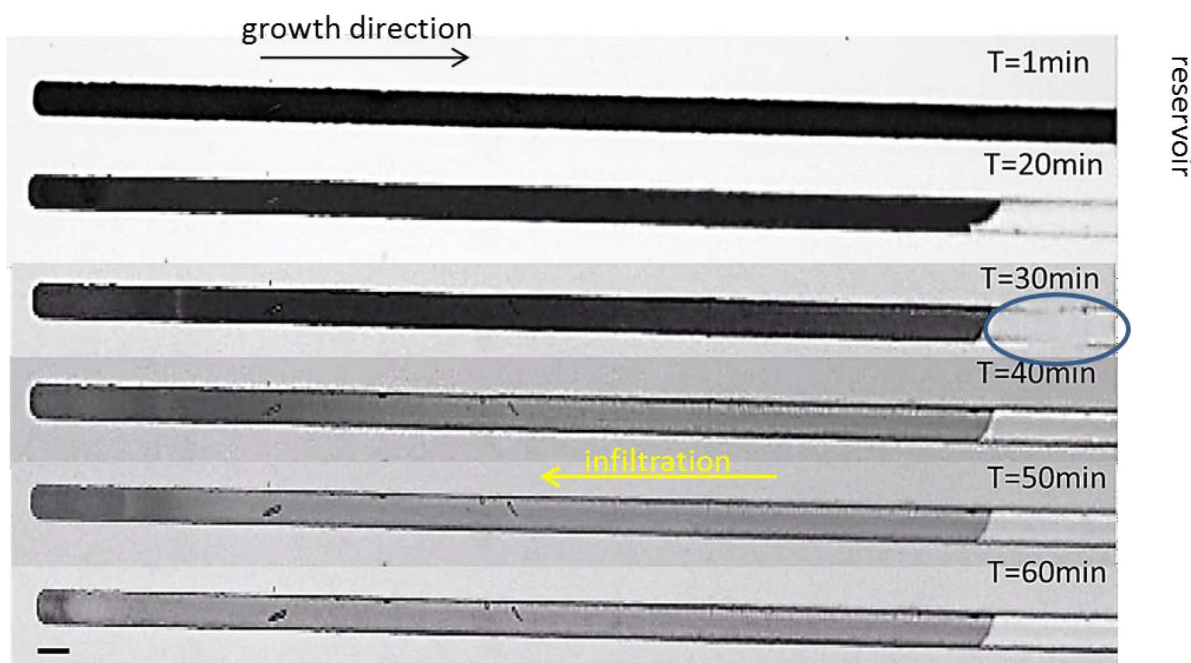


**Figure 79** Capture of the latex assembly and the PEG-DA infiltration through the latex lattice. The blue circle shows the moment when the PEG-DA enters the microchannel.

From Figure 79 we can observe that the latex spheres have filled the channel and after 20 minutes the latex particles are assembled inside the microchannels. Once the latex particles are assembled, pure PEG-DA (700  $M_w$ ) is injected inside the channel. After 30 minutes from the beginning of the

experiment it is possible to see the PEG-DA invasion inside the channels until it enters the dense colloidal material. Also in this case we see a change in the refractive indexes between the polymer, the latex and the PDMS confirming that the polymer goes inside the assembled material. In this case, it was really difficult to open the membrane device to recover the materials inside the channel. We also tried to make a cross section of the channel to have a look inside it as we have done in the previous tests, but without any success due to the low SEM resolution and also during the PDMS block cutting part of the material was no longer inside the channels.

### 3.6 Reproduction of the decoupled system

Until now, it has been possible to grow different materials with different lengths and thicknesses. We have also seen that it is possible to infiltrate different types of polymers into the assembled dense structures, reducing considerably the fractures in the final material. But now we want to try to infiltrate not only the latex structure but also the structure of the silicon-based materials and n-podes. By simulating the process inside the decoupled microevaporator, we used the membrane microdevice. At first, the filter was formed with latex particles, then changed with silica or silicon nanoparticles, and finally infiltrated with the polymer solution.

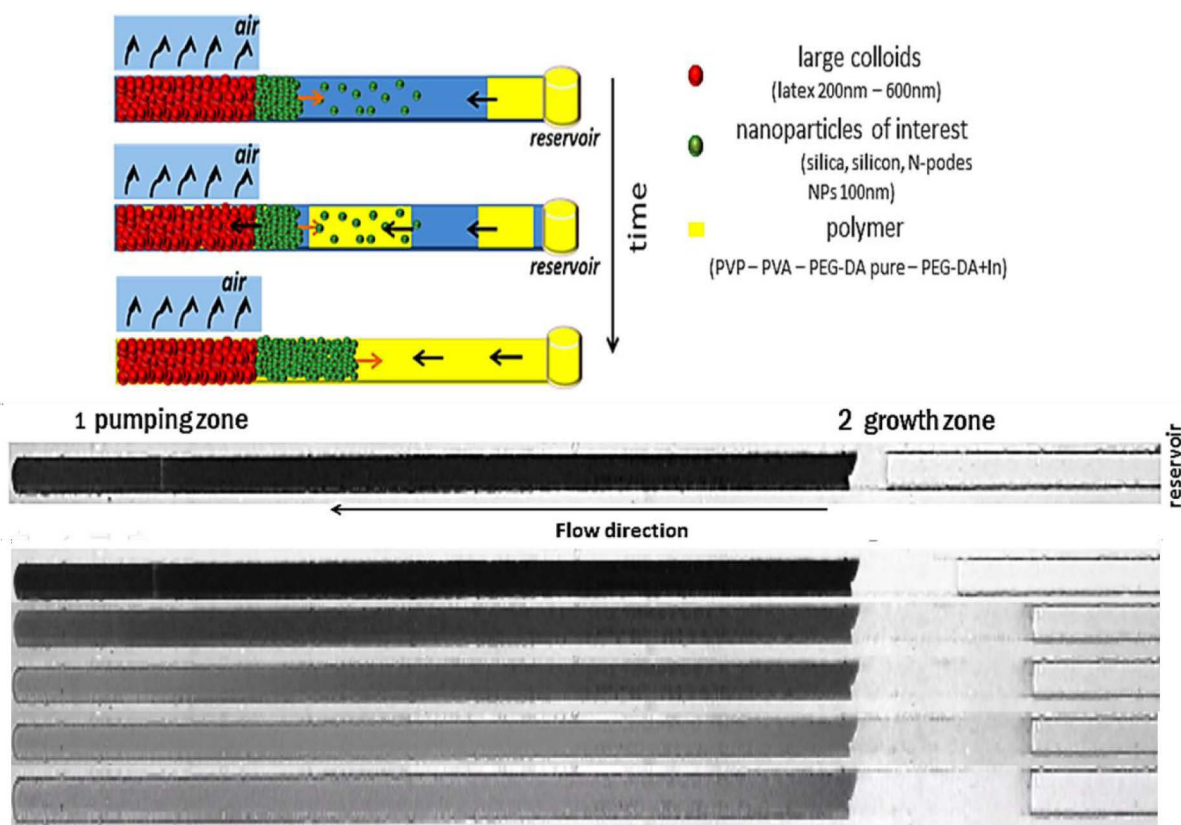
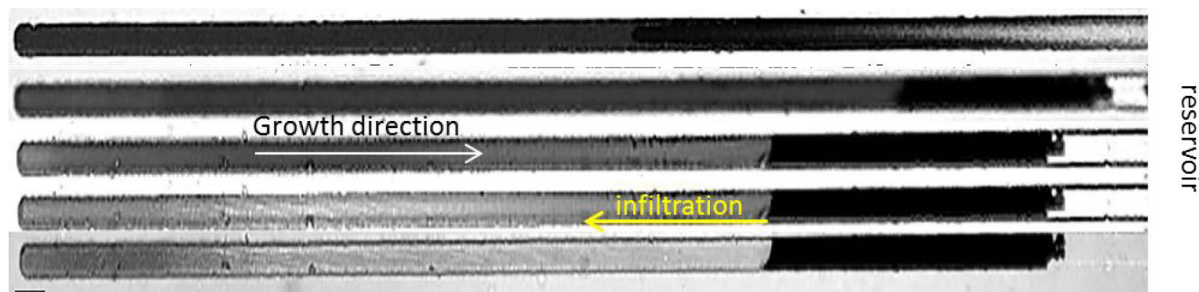


Figure 80(a) diagram of the decoupled microevaporator functioning; (b) single channel magnified and observed during the formation of the latex filter in black and white the dense material composed of silica nanoparticles. Over time the channel changes its refractive index after being infiltrated with the polymer solution (bottom). Scale bar 100  $\mu\text{m}$ .

The first test was carried out by assembling the 600 nm latex particles to create the filter, then switching with a 7% vol dispersion of silica nanoparticles with a diameter of 120 nm and then infiltrating the material assembled with 1.3% vol PVA. In figure (b) above, the mechanism of the decoupled microevaporator (Chip 3) has been reproduced using the membrane microevaporator (Chip 1). Using an optical microscope, an image of the zoomed channel was taken every 5 minutes to observe the assembly process. Initially, the latex dispersion was injected and after about 20 minutes we switched the latex dispersion with the silica dispersion. After 5 minutes we switched the silica dispersion with the PVA polymer solution. After about 5 minutes from the beginning of the infiltration process it is possible to see a front that formed between the dense phase of the dense silica material and the liquid phase of the PVA. As the polymer begins to flow into the porous structure of the assembled dense material, the entire material begins to change its refractive index. The change in the refractive index as reported above indicates that the polymer has infiltrated the entire length of the material.

After the infiltration process of the silica assembled nanoparticles, we tried to reproduce the same experiment using the silicon nanoparticles and then infiltrate them with the polymeric solution of PVP at 1.3%. As in the previous case, we acquired different images every 5 minutes to follow the growth of the material and the infiltration through it. After the formation of the latex nanoparticle filter, the latex dispersion was replaced by the silicon dispersion to finally switch with the polymer dispersion.



**Figure 81** Single channel during the assembling process. Filter growth to form the pumping zone, silicon nanoparticles assembly and PVP infiltration through the dense material. The infiltration is visible by the refractive index changing (Scale bar 100  $\mu\text{m}$ )

In the last three images of the channel, a change in the refractive index of the dense material can be seen as it flows inside the microchannel. So it means that the infiltration process is possible even using the silicon nanoparticles.

Using membrane microevaporators it was possible to choose the most suitable polymer for the production of a material that fits the specifications in terms of width and length in order to be able to characterize optically the materials.

### **3.5.1 Latex infiltration with PEG-DA**

To get an idea of how the assembled material changes after the infiltration process, we first formed a material using only latex particles, and then we infiltrate with it PEG-DA-700 with and without the photoinitiator used to activate the polymerization process when the polymer is shined with UV light. In order to reproduce and obtain a dense material using the silicon nanoparticles and N-podes and infiltrated with a PEG-DA solution, we tried to reproduce the infiltration process using the chip 3. In the following paragraph are reported the results of a dense material composed only of latex nanoparticles, a second dense material in latex infiltrated with pure PEG-DA-700 and finally a dense material consisting of latex nanoparticles infiltrated with PEG-DA-700 and its photo initiator.

#### **3.5.1.1 Latex dense material**

The assembly of the latex particles was formed using the pressure controller imposing an input pressure of 50 mbar and an input air pressure in the pumping area of 100 mbar. After the assembly process, the dense latex material is recovered to acquire SEM images and make profilometry characterization to estimate the height and roughness of the material. In Figure 82 are shows SEM images of the latex particles assembled. As the images shows the material does not show cracks formed during the fabrication process or during the material recovery.

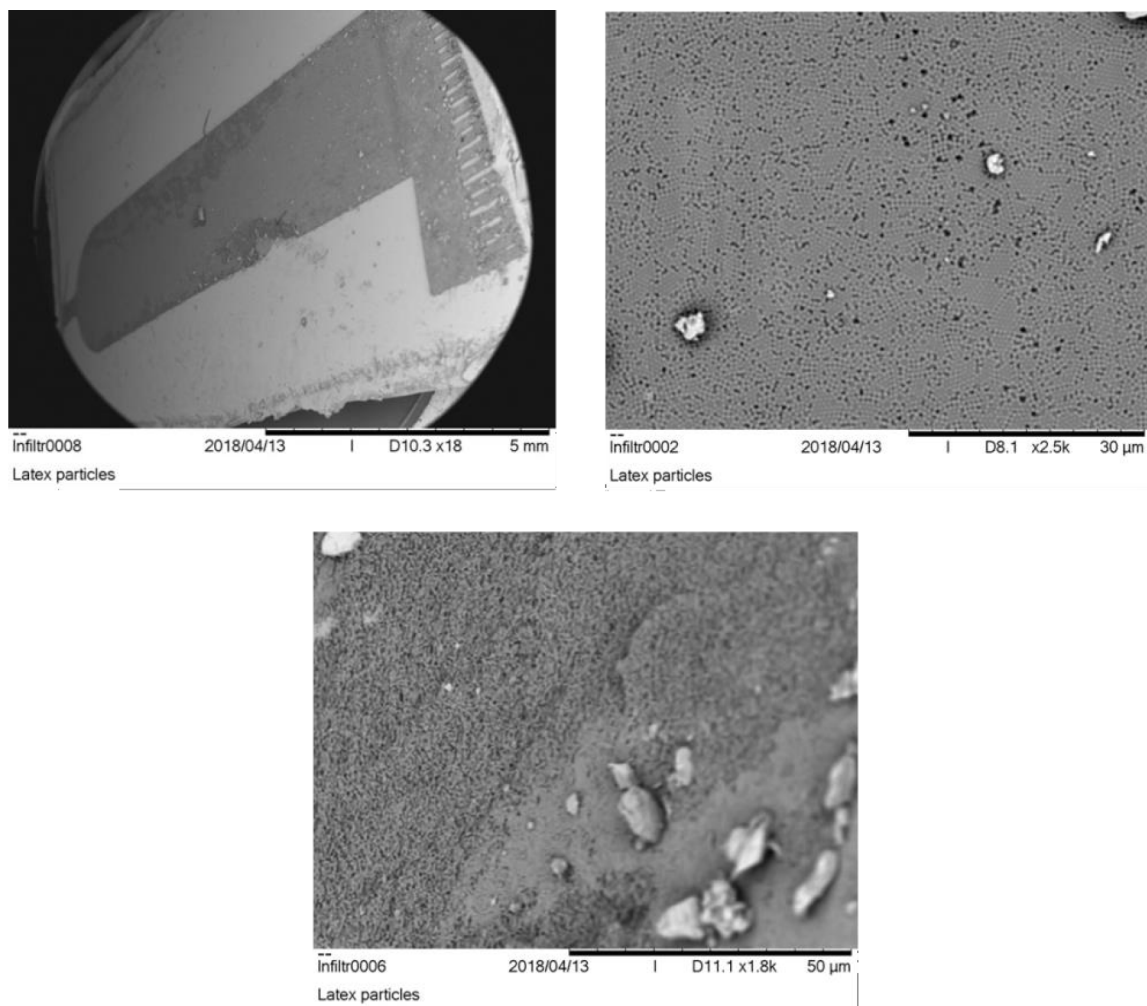


**Figure 82 SEM images of the latex dense material at the end of the assembling process**

From a profilometer analysis the surface of the material has a roughness of  $1.5\ \mu\text{m}$  with a height of  $18.5\ \mu\text{m}$ . Even if the material doesn't have any failures in the structure, the roughness is high and as already said in the previously chapter the high roughness can affect the optical measurements.

### 3.5.1.2 Latex infiltrated with PEG-DA

After forming the material with the latex particles, we tried to infiltrate the material with pure PEG-DA. After being infiltrated, the material was removed and observed using SEM to see the differences between the material infiltrated and the material not infiltrated with PEG-DA.

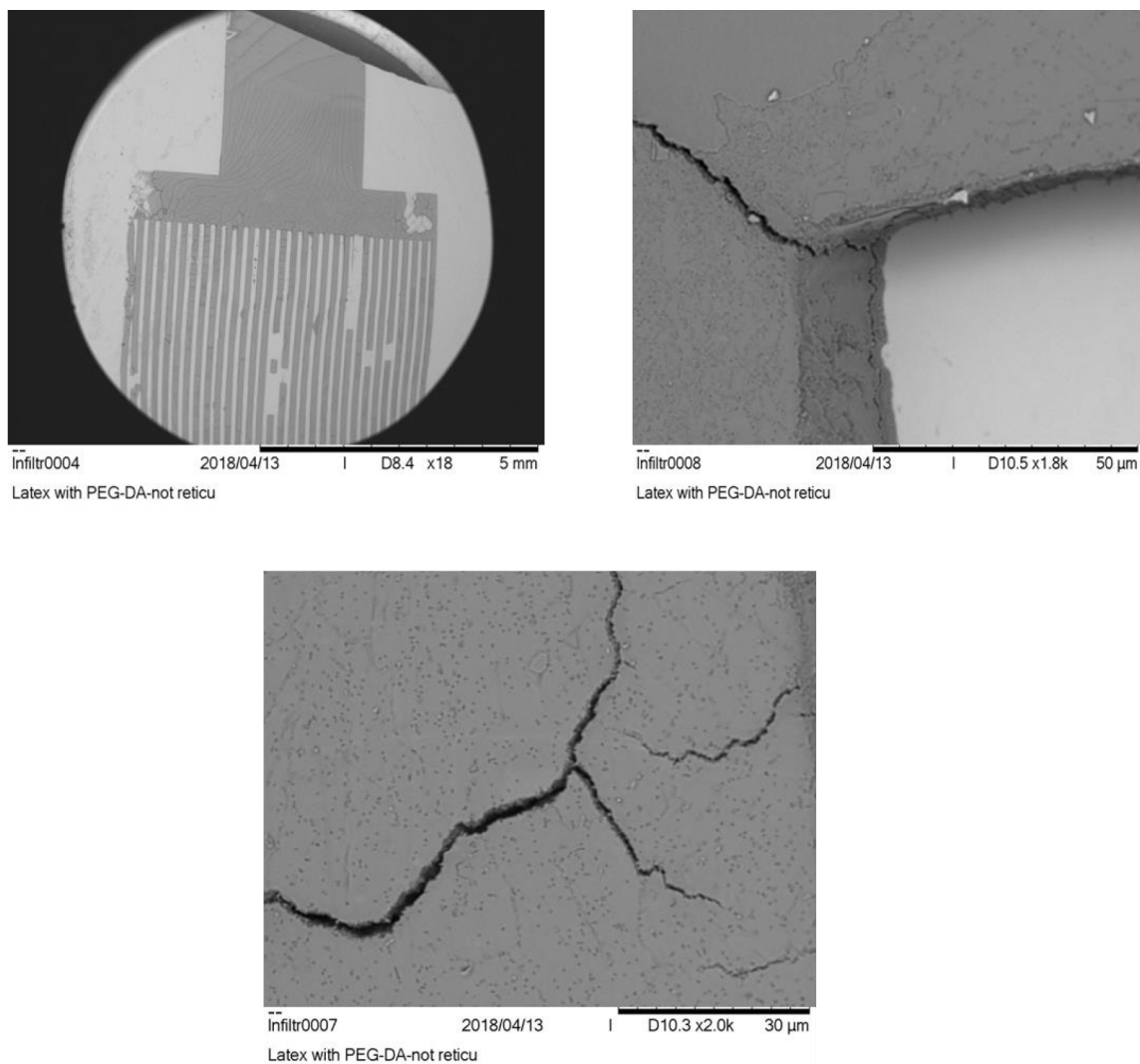


**Figure 83 SEM images of the latex dense material infiltrated with the pure PEG-DA**

The material in this case is more compact and the surface roughness is reduced. In fact, the final material thickness is  $20 \mu\text{m} \pm 1 \mu\text{m}$ , measured using a profilometer. But differently from the case precedent case with only latex, the dense material shows up cracks in the structure. That's why in the next experiments we tried to photo-polymerize the polymer to see if it was possible to avoid cracks.

### 3.5.1.3 Latex infiltrated with PEG-DA+In

The last comparison is to use a polymer solution based on PEG-DA (molar mass 700 Mw) plus a photoinitiator (2-Hydroxy-2-methylpropiophenone (HMP) at 1% vol.), sensitive to UV light. Once the PEG-DA has been infiltrated into the latex formed by the latex particles, the PEG-DA+HMP has been illuminated with ultraviolet light to facilitate cross-linking and to obtain a solid material but at the

same time being able to change the mechanical properties of the material. Subsequently, the material was characterized.

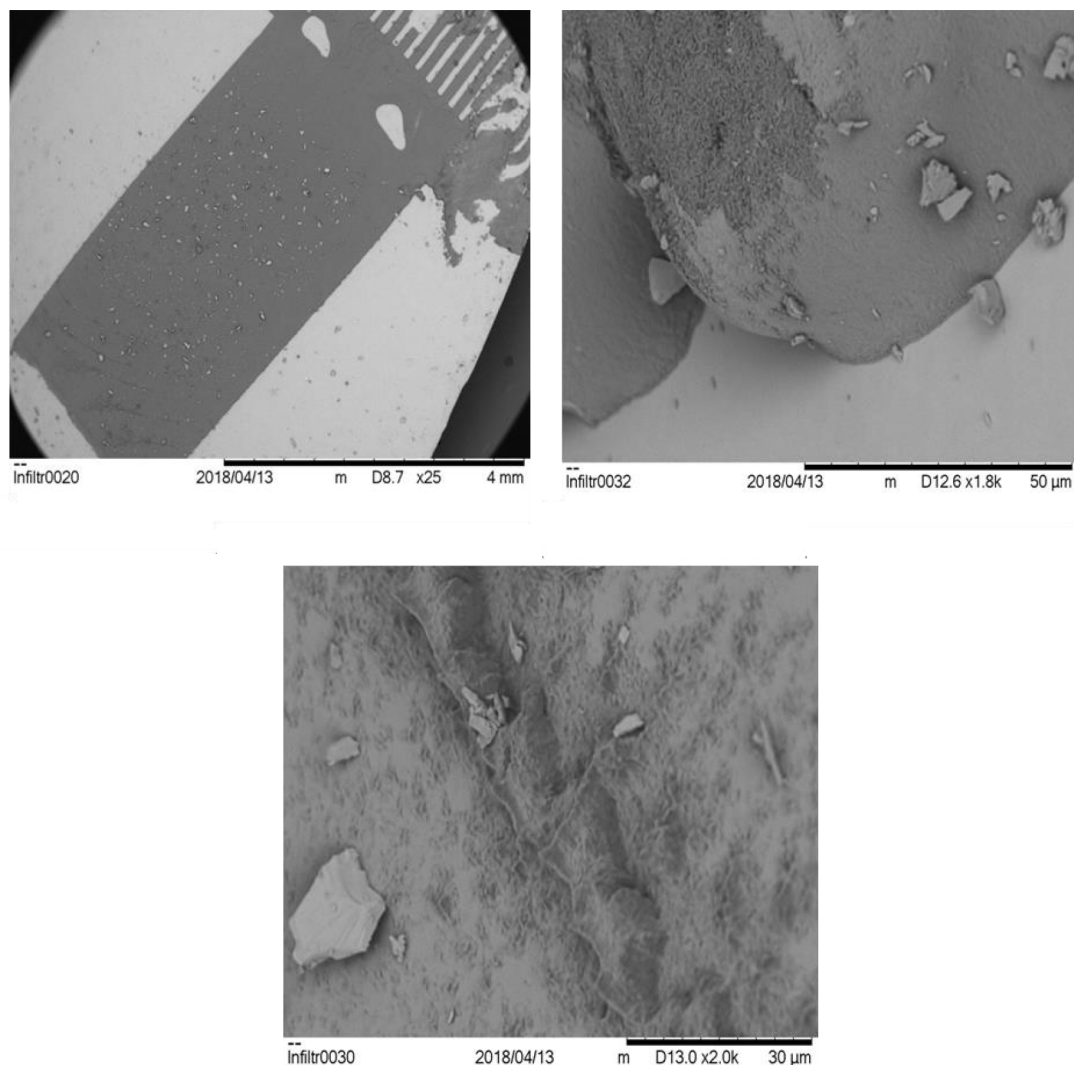


**Figure 84 SEM images of the latex dense material infiltrate with PEG-DA+HMP and reticulated**

The material is more compact and smooth. In fact, the surface roughness of the material is considerably reduced as shown by the profilometer measurements: the thickness of the final material is indeed  $18.5 \pm 0.3 \mu\text{m}$ .

In a final step, we made a material that was made up only of PEG-DA+HMP and then cross-linked to get an idea of the structure of the pure polymeric material after being cross-linked. Figure 85 shows a SEM image of the pure PEG-DA cross-linked at a very high resolution.

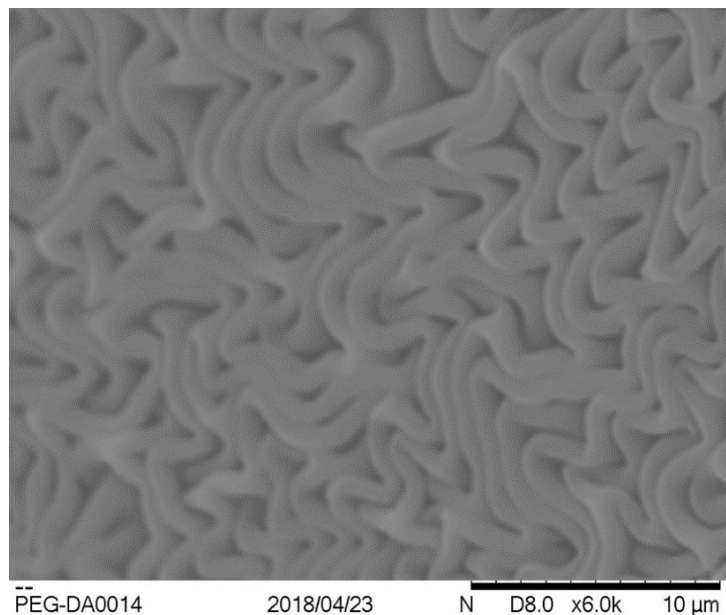
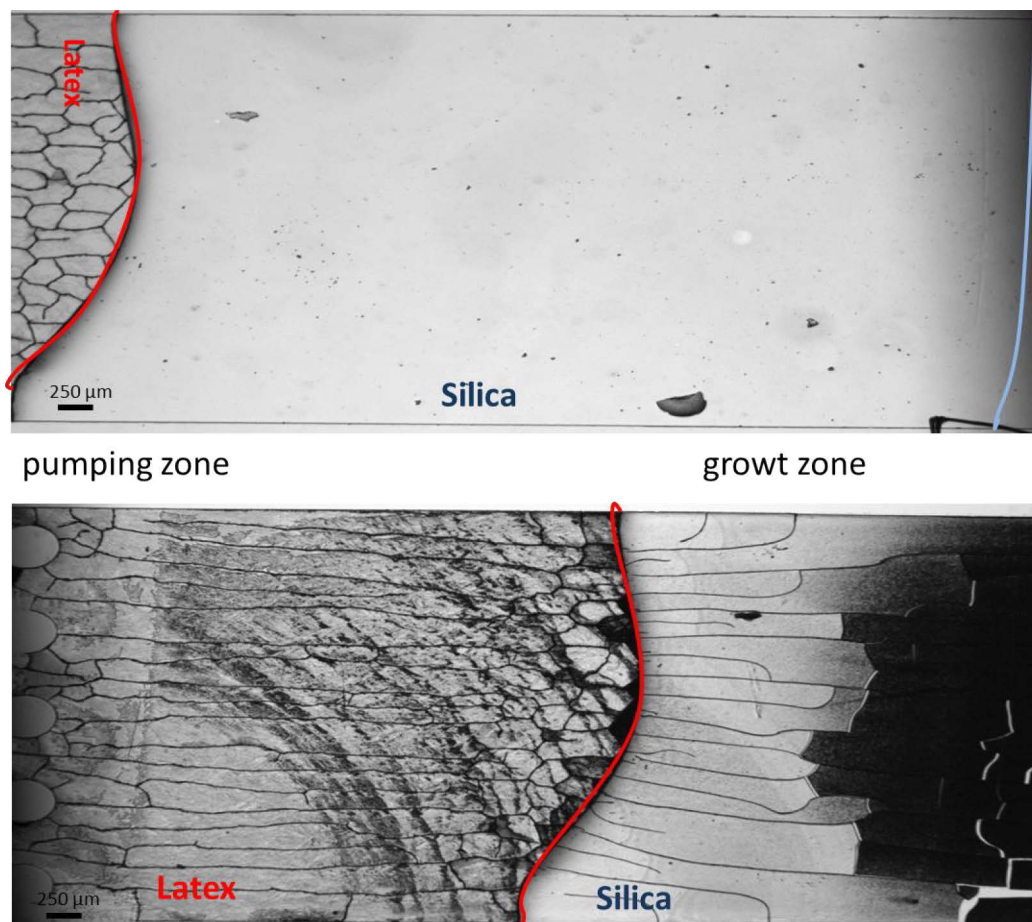


Figure 85 SEM images of the pure PEG-DA+HMP reticulated

The particular structure of the PEG-DA material after the photo polymerization, in our case is due to the shrinkage of the long polymer chain formed during the process. The wrinkles occur when the residual stresses exceed a critical value, which can be induced by heating, solvent swelling, mechanical stretching/compression and capillarity from bilayer thin films of dissimilar mechanical properties and crosslinked gels [51].

### 3.5.3 Silica infiltration

To check that the polymer can be infiltrated with two different types of nanoparticles with different diameters, a material with silica nanoparticles was assembled. As previously described, the pumping area was formed using latex nanoparticles and after its formation the dispersion was switched to the silica dispersion. After about 3 hours from the beginning of the assembly process of the nanoparticles, the dense material had already formed. So we proceeded with the infiltration of the dense material using PEG-DA-700+HMP at 1%. The polymer infiltration lasted about 5 hours, after which the dense material was photo-polymerized to induce cross-linking.



**Figure 86** Silica dense material infiltrated with PAG-DA+HMP1% before (top) and after (bottom) the photopolymerization. The red line indicates the front between the latex dense material and the silica dense material.

Once the polymer had been cross-linked inside the microdevice, it was possible to remove the PDMS mold to recover the final material. As shown in Figure 86, the material inside the mold had no visible fractures before being removed but after the polymerization multiple fractures appeared.

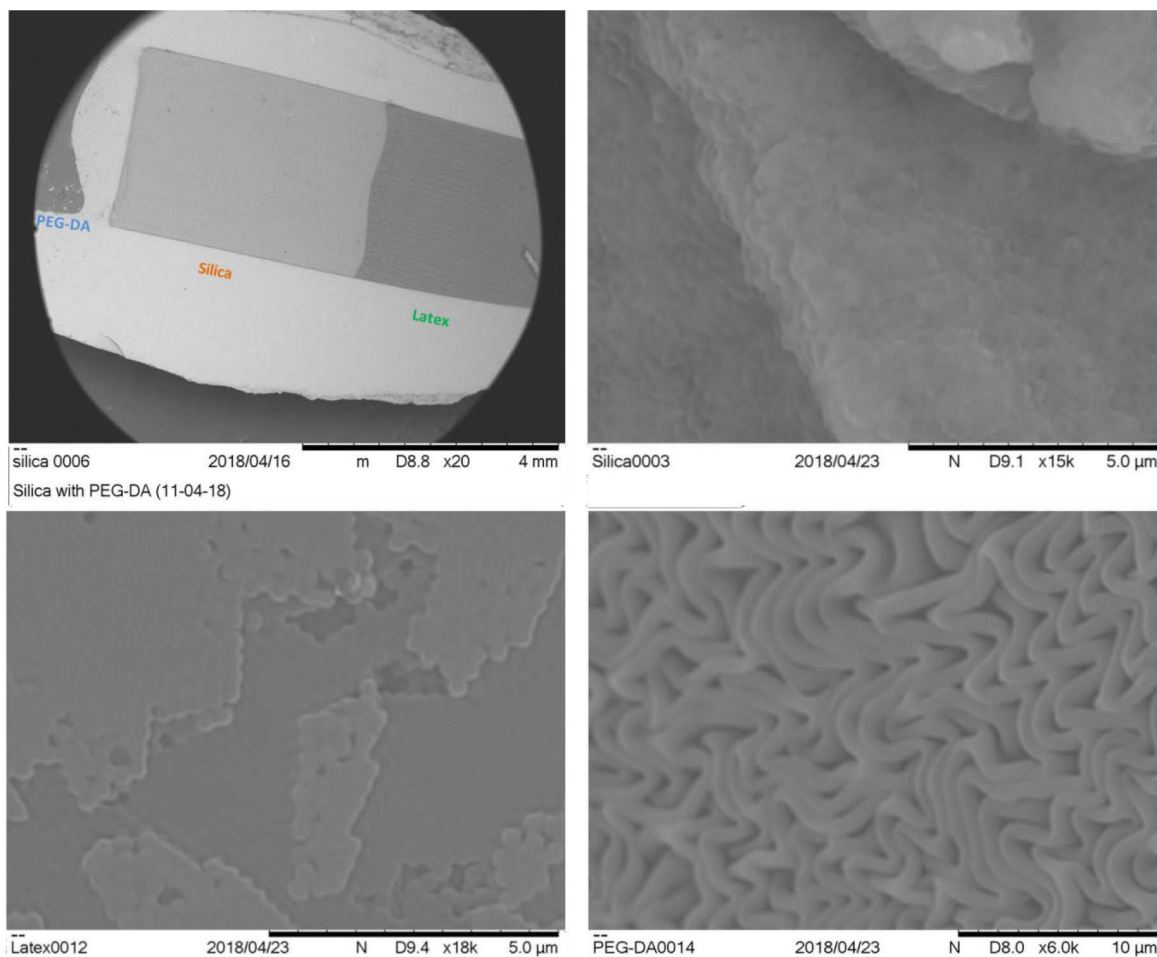


**Figure 87** SEM images of the dense material. a) silica nanoparticles covered with the PEG-DA reticulated; b) latex nanoparticles covered with the PEG-DA reticulated; c) PEG-DA reticulated

From the SEM images we can see that the polymer has infiltrated into the dense material formed by latex and silica.

### 3.5.4 Silicon infiltration

Once we observed the differences of the several stages of infiltration and of the nature of the crosslinked and not crosslinked polymer, we tried to repeat the experiment using the nanoparticles of interest. In this paragraph we show the assembly of the nanoparticles of decapodes at 0.7% v infiltrated with pure PEG-DA (molar mass) through the addition of the photoinitiator 2-Hydroxy-2-methylpropiophenone (HMP) at 1%. In Figure 88 is shown the final dense material obtained by assembling the silicon nanoparticles and after that the polymer photopolymerization.



**Figure 88** Silicon dense material recovered after been infiltrate with PEG-DA+HMP1% and reticulated.

We proceed by infiltrating a material formed by silicon nanoparticles assembled inside the growth zone of the microdevice. As before, the pumping zone was formed by assembling the latex nanospheres. After the formation of the dense material, PEG-DA+HMP 1% was injected into the assembled material and then cross-linked with a UV lamp.

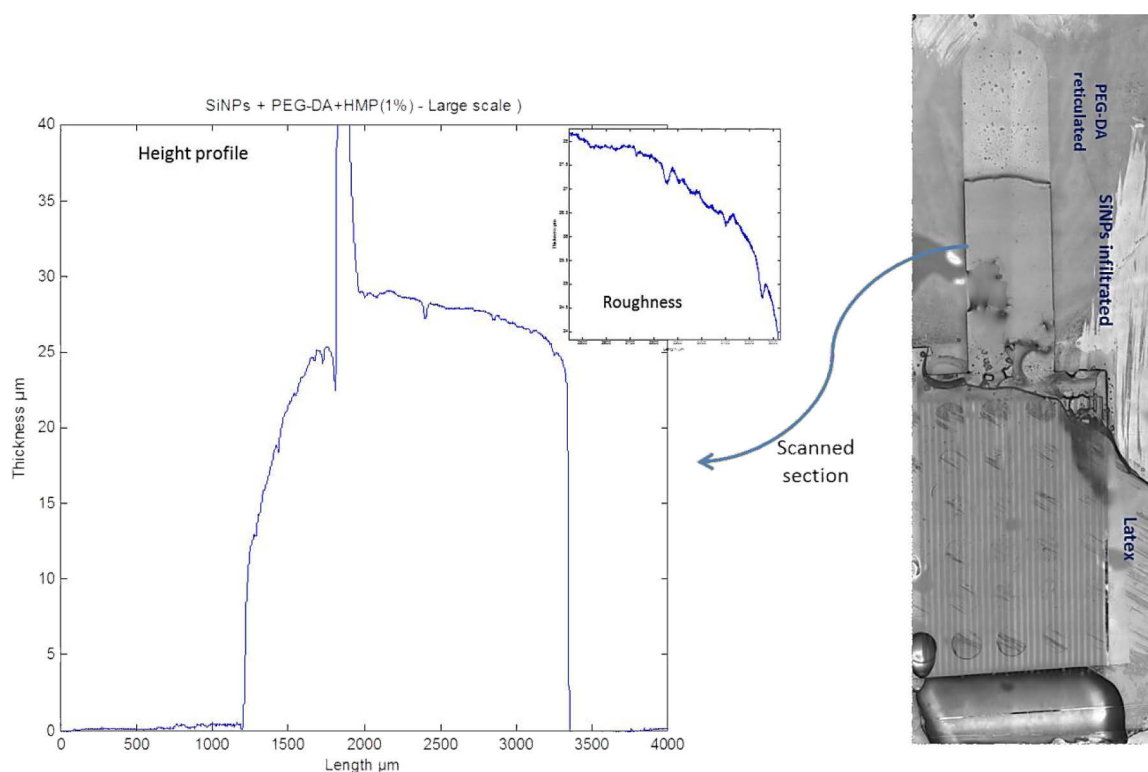


**Figure 89** Optical profilometry acquisition. The height profilometry scan of a dense silicon material section (left); image acquired by optical profilometry (right)

Once the material had been recovered, the surface of the assembled material was scanned using an optical profilometer. From Figure 89 it can be seen that the final material has a height of about 25  $\mu\text{m}$  and the surface roughness is of the order of the size of the silicon nanoparticles, about 0.2  $\mu\text{m}$ . This suggests that PEG-DA is able to create a mesh all around the assembled nanoparticles, thus reducing fractures and the surface roughness.

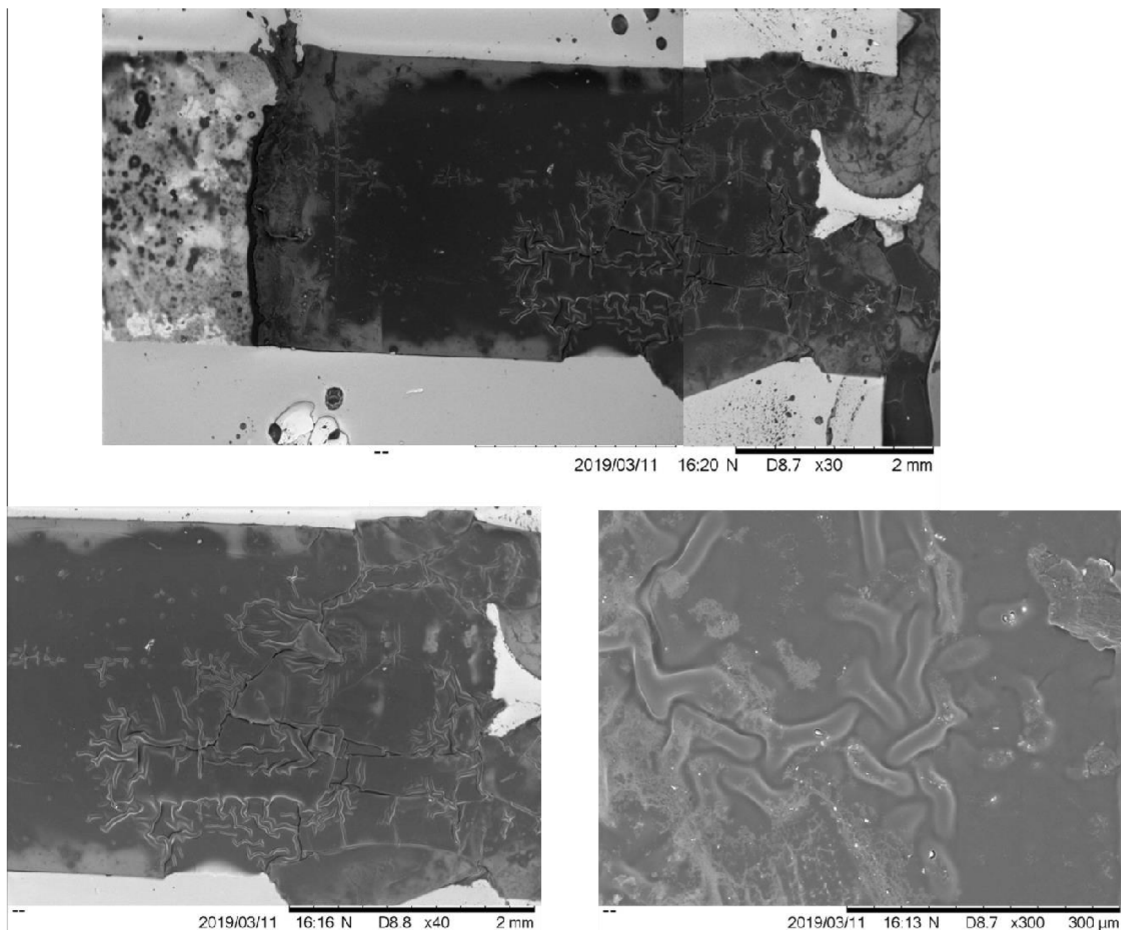


Figure 90 SEM images of the infiltrated silicon dense material after the photopolymerization process.

Also we were able to acquire some SEM images of the material to better see the surface of the material, see Figure 90. In fact, as can be seen from the SEM images, in some points of the material, the photo-polymerized PEG-DA has shrunk due to the mechanical properties of the polymer.

### 3.5.5 Decapodes infiltration

The Figure 91 shows four frames of the assembled material. In grey the assembled latex particles and in black the nanoparticles of decapodes.

In Figure 91, the PEG-DA+HMP is injected into the channel, where it begins to flow through the porous cavities of the material. As PEG-DA is pure, its viscosity is very high and the absence of water

inside the solution avoids that it flows through the entire material. To overcome this problem, the material is flushed before with water and as the water pervaporates the polymer is dragged into the system. In this way PEG-DA creates a network all around the dense material.

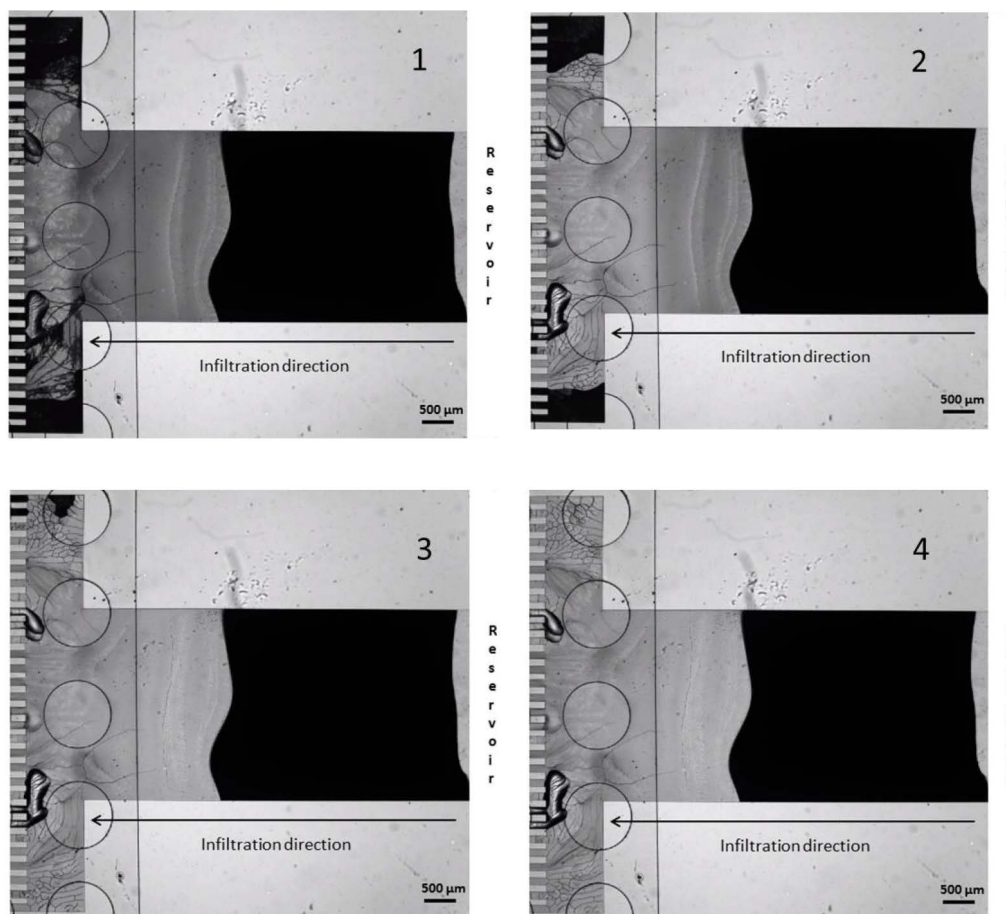


**Figure 91** four different moments of the infiltration process after the dodecapodes assembling.

In fact in images 2 to 4 we can see how the refractive index of the latex changes in light intensity. And as already observed previously, this means that the polymer has infiltrated the porous colloidal assembly.

Once the polymer has covered the entire material, it has been shined with UV light to allow the PEG-DA to form a more compact and homogeneous structure.

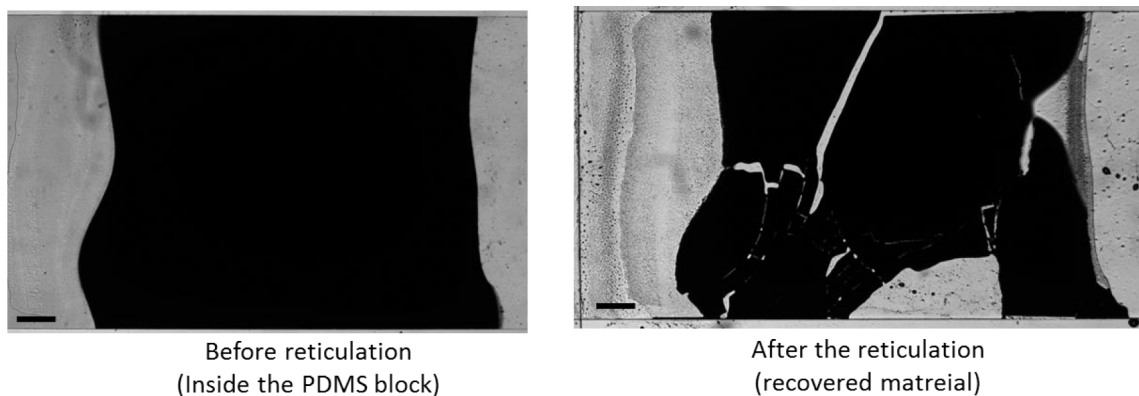


**Figure 92** Images captured before and after the reticulation by the UV light (scale bar 500  $\mu\text{m}$ ).

After crosslinking and PDMS block removal, several fractures appeared, probably due to mechanical stresses during the removal of the PDMS mold. After recovering the material, it was possible to measure its thickness and its roughness. The final material was  $(18 \mu\text{m} \pm 0.2) \mu\text{m}$ . By using PEG-DA+HMP we were able to reduce the fractures in the material but also the surface roughness, reaching about the same order of size as the nanoparticles used. In addition, it was possible to acquire SEM images and compare them with the previously assembled material where no polymer was present.

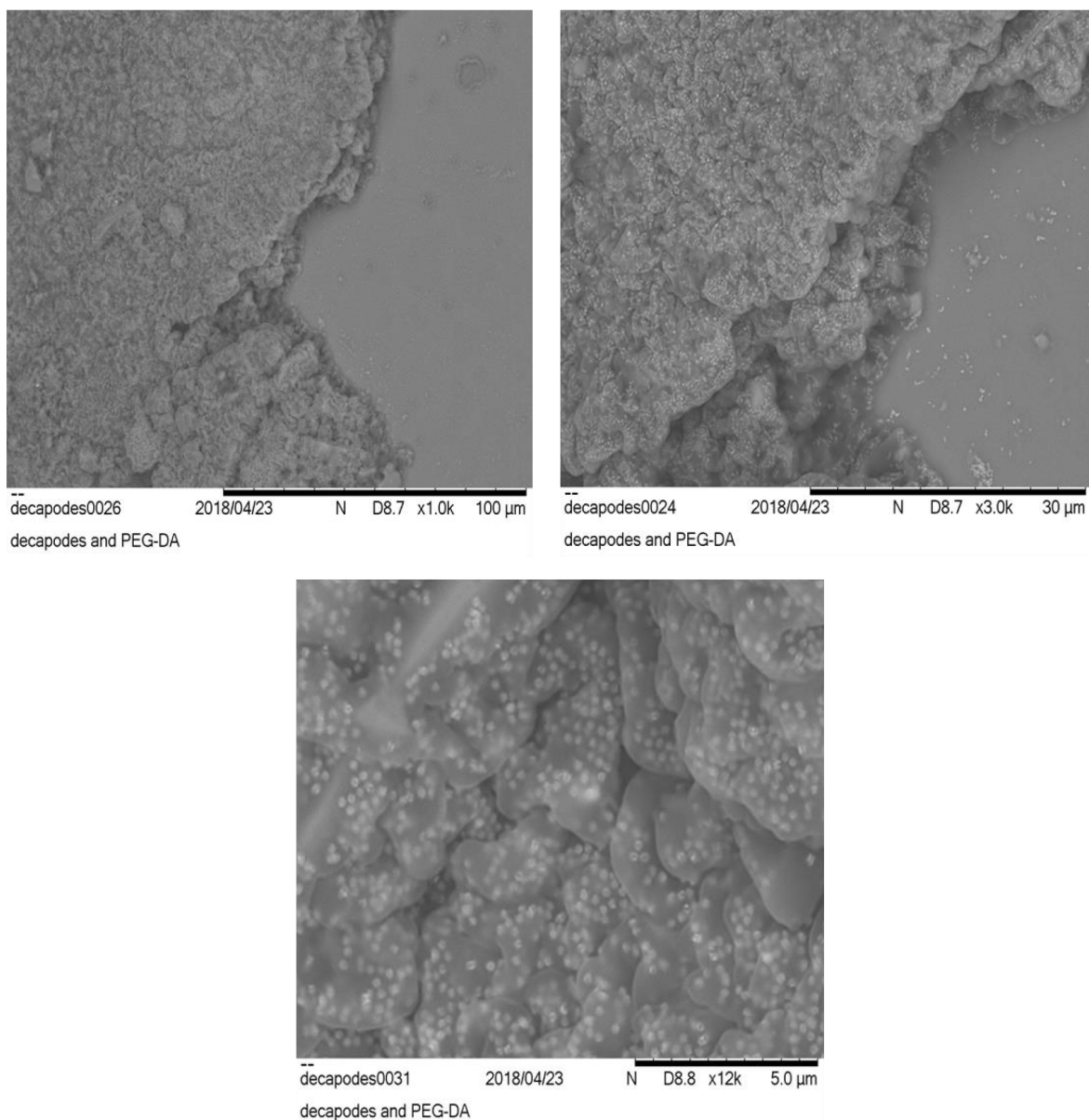


**Figure 93 SEM images of the infiltrated dense dodecapodes dense material.**

From the SEM images we can clearly see that the polymer after being cross-linked has created a network all around the pre-assembled material. In the images, it is also possible to see the nanoparticles trapped inside the polymeric matrix. On this sample it was possible to run optical characterization to extract the  $n$  and  $k$  values but the results obtained were not as expected since the dispersion used presented some problems with the gold satellites related to the synthesis process.

# Conclusions

---

During this work we were able to fabricate dense materials starting from diluted solution, using different types of microfluidic devices, already used in the previous works carried out at LOF and developing of a new microfluidic device able to decouple the pumping area from the growth zone obtaining a dense material with a larger surface area (from few micrometer surface size to a few millimeter). We also try to prevent mechanical fracture during the drying process after the particles concentration into the microfluidic channel. We used the polymer infiltration technique and in some case we reduced the amount of cracks but in other cases the fractures didn't formed inside the dense assembled structure. When particles do not deform viscously, the capillary pressure produces elastic deformation that stores energy in the packing and, therefore, is capable of generating cracks in the films. William B. Russel [52] demonstrate that viscous deformation increases the capillary pressure necessary for cracking, as does reducing the film thickness. That could be an explanation for thin materials assembled using chip 2. In fact the materials obtained by using chip 2 they had a thickness of about  $4\mu\text{m}$ . On the other hand, the thicker dense materials showed fracture or before or after the PDMS peeling and as we already showed in Chapter 3 we were able to reduce the fractures using the polymer infiltration.

Furthermore, due to the nature of the materials and the ellipsometric microspot, it was difficult to obtain clear optical characterizations and in particular the extrapolation of the effective  $n$  and  $k$  values. Because of this difficulty encountered during the development of the thesis work, it has been decided in future experiments to use alternative ellipsometric characterization methods. Two ideas have been developed. The first one concerns the characterization through the 3 mm thick glass blade, through which the ellipsometric beam is able to neglect the interactions with the glass given by the reflection of the symmetrical planes. The second idea is to perform an optical characterization during the assembly process of the nanoparticles. This type of measurement is therefore a measurement during the assembling process inside the microfluidic device where the material is not dried but it is still in the liquid phase. In this way it is possible to play on the concentration factor of the final dense material.

The optical properties of particles in close proximity are different than individual particles [53], thus, we cannot predict in advance exactly how these materials will interact with light.

That's why the assembling of these sub-units can be used in other field with different application. For examples, the photonic crystal, defined as periodic composites of dielectric material that can be used for controlling propagation and emission of light. They offer a flexible way to control emission and propagation of light and the light-matter interaction strength can be tailored by varying, for example, the lattice constant of the structure. Photonic crystals were originally proposed for suppressing spontaneous emission of light that potentially may improve devices such as solar cells or lasers [54].

By micro-fluid assembly it is possible to fabricate dense materials in other in different fields of application. An example could be the assembly of colloidal particles into opals. In fact, due to their periodical structure, they are able to varying scattering potential for the light, giving to the material optical properties similar to the electrical properties of a semi-conductor. The idea of using those materials becomes from the structural property given by the insertion of elements with high dielectric constant between the void formed by the spherical particles during the assembling process to finally remove the particles to obtain a “porous” dense material with extraordinary optical properties [55].

# Bibliography

- [1] V.G Veselago, "Electrodynamics of substances with simultaneously negative," *Sov Phys Usp*, vol. 10, p. 509–514, 1968.
- [2] Pendry, J. B., "Negative refraction makes a perfect lens," *Phys. Rev. Lett*, vol. 85 (18), p. 3966–3969, 2000.
- [3] D. R. Smith, Willie J. Padilla, D. C. Vier, S. C. Nemat-Nasser, and S. Schultz, "Composite Medium with Simultaneously Negative Permeability and Permittivity," *PHYSICAL REVIEW LETTERS*, vol. 84, p. 4184, 2000.
- [4] R. Farzad Zangeneh-Nejad, "Active times for acoustic metamaterials," *Reviews in Physics*, vol. 4, 2019.
- [5] Mike Haberman, Matthew Guild, "Acoustic metamaterials," *Physics Today*, vol. 69, p. 42, 2016.
- [6] Ercan M. Dede, Feng Zhou, Paul Schmalenberg, Tsuyoshi Nomura, "Thermal Metamaterials for Heat Flow Control in Electronics," *Journal of Electronic Packaging*, vol. 140, pp. 1-10, MARCH 2018.
- [7] Gwanwoo Park, Sunggu Kang, Howon Lee & WonjoonChoi, "Tunable Multifunctional Thermal Metamaterials: Manipulation of Local Heat Flux via Assembly of Unit-Cell Thermal Shifters," *Nature - scientific reports*, vol. 7, pp. 1-15, January 2017.
- [8] N. A. Fleck, V. S. Deshpande, M. F. Ashby, "Mechanical Metamaterials and Their Engineering Applications," *Proc. R. Soc. A Math. Phys. Eng. Sci.*, p. 2495., 2010.
- [9] James Utama Surjadi, Libo Gao, Huifeng Du, Xiang Li, Xiang Xiong, Nicholas Xuanlai Fang and Yang Lu, "Mechanical Metamaterials and Their Engineering Applications - review," *Advanced Engineering Materials*, vol. 1800864, pp. 1-37, 2019.
- [10] Shalaev, W. Cai and V., "Chapter 5 - Magnetic Metamaterials," in *Optical Metamaterials - Fundamentals and Applications*, Springer Science+Business Media, LLC 2010, DOI 10.1007/978-1-4419-1151-3 5.
- [11] Wikipedia, "<https://en.wikipedia.org/wiki/Superlens>," [Online].
- [12] Mohamed K. Azizi, Henri Baudrand, Lassaad Latrach and Ali Gharsallah, "Metamaterial-Based Flat Lens:Wave Concept Iterative Process Approach," *Progress In Electromagnetics Research*, vol. 75, p. 13–21, 2017.
- [13] LAMB, WILLIAM HARRIS & ROBERT, "[science.howstuffworks.com/invisibility-cloak2.htm](http://science.howstuffworks.com/invisibility-cloak2.htm)," [Online].

- [14] Wikipedia, "[https://en.wikipedia.org/wiki/Metamaterial\\_cloaking](https://en.wikipedia.org/wiki/Metamaterial_cloaking)," [Online].
- [15] Nicholas Fang, Dongjuan Xi, Jianyi Xu, Muralidhar Ambati, Werayut Srituravanich, Cheng Sun & Xiang Zhang, "Ultrasonic metamaterials with negative modulus," *Nature Materials*, no. 5, p. 452–456, 30 April 2006.
- [16] muamer-kadic, [Online]. Available: <http://members.femto-st.fr/muamer-kadic/>.
- [17] Jacoby, Mitch, "Metamaterials With Unusual Mechanics," *c&en*, vol. 93, pp. 28-29, 2015.
- [18] Josh, Jacobs, "Financial Times," 29 March 2018. [Online]. Available: <https://www.ft.com/content/c6864c76-de7d-11e7-a0d4-0944c5f49e46>.
- [19] "Wikipedia - SRR," [Online]. Available: [https://en.wikipedia.org/wiki/Split-ring\\_resonator#/media/File:Split-ring\\_resonator\\_array\\_10K\\_sq\\_nm.jpg](https://en.wikipedia.org/wiki/Split-ring_resonator#/media/File:Split-ring_resonator_array_10K_sq_nm.jpg).
- [20] Shumin Xiao, Vladimir P. Drachev, Vladimir M. Shalaev, "Loss-free and active optical negative-index metamaterials," *Nature*, vol. 466(7307), pp. 735-8, August 2010.
- [21] Cao, Krzysztofik and, "Metamaterials in Application to Improve Antenna Parameters," in *Metamaterials in Application to Improve Antenna Parameters*, IntechOpen, 2018.
- [22] Cai, Shalaev, "Chapter 5 - Magnetic Metamaterials," in *Optical Metamaterials - Fundamentals and Applications*, Springer-Verlag New York, 2010.
- [23] Kroll, D.R. Smith and N., "Negative refractive index in left-handed," *Phys. Rev. Lett.*, vol. 85, p. 2933, 2000.
- [24] Granaa, "Hierarchical self-assembly of a bulk metamaterial enables isotropic magnetic permeability at optical frequencies," *Materials Horizons*, pp. 1-6, 2016.
- [25] A. Alù, A. Salandrino, N. Engheta, *Opt. Express*, p. 14, 2006.
- [26] What is nanotechnology?, "nanowerk," [Online]. Available: [https://www.nanowerk.com/nanotechnology/introduction/introduction\\_to\\_nanotechnology\\_1.php](https://www.nanowerk.com/nanotechnology/introduction/introduction_to_nanotechnology_1.php).
- [27] Galstyan et al., , "Metal Oxide Nanostructures in Food Applications: Quality Control and Packaging," *Chemosensor*, vol. 6, p. 2 of 21, 2018.
- [28] H. Victor, 2016. [Online]. Available: <https://www.slideshare.net/HaraVictorIyerHara/lithographic-techniques-including-x-ray-lithography>.
- [29] George M. Whitesides, et al., "Self-Assembly at All Scales," *Science*, vol. 295, p. 2418, 2002.

- [30] N. R. Council, *Biomolecular Self-Assembling Materials: Scientific and Technological Frontiers*, Washington, DC: The National Academies Press, 1996.
- [31] Shenyu Yang, Yun Yan, Jianbin Huang, Andrei V. Petukhov, Loes M. J. Kroon-Batenburg, Markus Drechsler, Chengcheng Zhou, Mei Tu, Steve Granick & Lingxiang Jiang, "Giant capsids from lattice self-assembly of cyclodextrin complexes," *Nature Communications*, vol. 8, 2017.
- [32] Filion, Laura Christine, "Self-assembly in colloidal hard-sphere systems," Utrecht University, The Netherlands, 2011.
- [33] Liu, Zhang and, "Experimental modelling of single-particle dynamic processes in crystallization by controlled colloidal assembly," *Chemical Society Reviews*, vol. 43, p. 2324, 2014 .
- [34] M. Holgado, F. García-Santamaría, A. Blanco, M. Ibasate, A. Cintas, H. Míguez, C. J. Serna, C. Molpeceres, J. Requena, A. Mifsud, F. Meseguer, and C. López, "Electrophoretic Deposition To Control Artificial Opal Growth," *Langmuir*, vol. 15, pp. 4701- 4704, 1999.
- [35] Pusey et al., "Structures of crystals of hard spheres," *Physical Review Letter*, vol. 65, 1989.
- [36] N.D. Denkov, O.D. Vlev, P.A. Kralchevsky, I.B. Ivanov, H. Yshimura, K. Nagayama, "Two-dimensional crystallization," *Nature*, vol. 361, p. 26, 1997.
- [37] Janne-Mieke Meijer, Fabian Hagemans, Laura Rossi, Dmytro V. Byelov, Sonja I.R. Castillo, "Self-Assembly of Colloidal Cubes via Vertical Deposition," *Langmuir*, vol. 28, pp. 7631-763, 2012.
- [38] Ludivine Malassis Pascal Massé Mona Tréguer-Delapierre Stephane Mornet Patrick Weisbecker Philippe Barois Constantin R. Simovski Vasyl G. Kravets Alexander N. Grigorenko, "Topological Darkness in Self-Assembled Plasmonic Metamaterials," *Advanced Materials*, 18 October 2013.
- [39] *Langmuir-Blodgett Films: An Introduction*, Cambridge University Press: Cambridge University, 1996.
- [40] R. Dangla, F. Gallaire, and C.N. Baroud., "Microchannel deformations due to solvent induced PDMS swelling," *Lab Chip*, vol. 10(21), 2010.
- [41] David Julian McClements, *Food Emulsions: Principles, Practices, and Techniques*, Taylor & Francis, 2004.
- [42] Baron., J. M. Watson and M. G., "The behaviour of water in poly(dimethylsiloxane)," *Journal of Membrane Science*, vol. 110, no. (1), pp. 47-57, 1996.
- [43] E. Favre, P. Schaetzel, Q. T. Nguygen, R. Clement, and J. Neel., "Sorption, diffusion and vapor permeation of various penetrants through dense poly(dimethylsiloxane) membranes - a transport analysis.," *Journal of Membrane Science*, vol. 92, no. (2), p. 169–184, 1994.

- [44] X. Noblin, L. Mahadevan, I. A. Coomaswamy, D. A. Weitz, N. M. Holbrook, and M. A. Zwieniecki, "Optimal vein density in artificial and real leaves," *PNAS*, vol. 105, no. (27), pp. 9140-9144, July 8, 2008.
- [45] E. Verneuil, A. Buguin, and P. Silberzan., "Permeation-induced flows : Consequences for silicone-based microfluidics.," *Europhysics Letters*, vol. 68, no. 3, p. 412–418, 2004.
- [46] J. Leng, B. Lonetti, P. Tabeling, M. Joanicot, and A. Ajdari., "Microevaporators for kinetic exploration of phase diagrams," *Phys. Rev. Lett.*, p. 96 : 084503, 2006..
- [47] Merlin, Aurore, *Cinétiques de concentration de suspensions colloïdales par évaporation microfluidique : de la solution diluée aux cristaux colloïdaux*, Bordeaux: Univertité de Bordeaux, 2010.
- [48] Laval, Cédric, *Fabrication par pervaporation microfluidiques de matériaux composites d'architecture et de composition controlees pour la rfealisation de MEMS organiques*, Bordeaux: Université de Bordeaux, 2015.
- [49] A. Reindl et al., "Dispersing, Stabilizing and functionalizing Silicon Nanoparticles," *PARTEC*, 2007.
- [50] Many, Véronique, "Synthèse et design de nanorésonateurs optiques actifs dans le visible," Université de Bordeaux, Bordeaux, 2018.
- [51] Chi-Mon Chen and Shu Yang, "Wrinkling instabilities in polymer films and their applications," *Polym Int*, vol. 61, p. 1041–1047, 2012.
- [52] William B. Russel, "Mechanics of Drying Colloidal Dispersions:," *AIChE Journal*, vol. 57, pp. 1378- 1385, 2011.
- [53] U. Zywiertz, M. K. Schmidt, A. B. Evlyukhin, C. Reinhardt, J. Aizpurua, B. N. Chichkov , "Dielectric Metamaterials: Fundamentals, Designs, and Applications," *ACS Photonics*, vol. 2, p. 913, 2015.
- [54] Lodahl, P., "All-solid-state quantum optics employing quantum dots in photonic crystals," Woodhead Publishing Series in Electronic and Optical Materials Preface, 2012.
- [55] P. B. Landon, "Self-assembly of colloidal silica into opals with large ordered single crystals," *Colloids and Surfaces A: Physicochemical and Engineering Aspects*, 2005.
- [57] J. Angly, Bordeaux: Université de Bordeaux, 2013.
- [58] C. Jeffrey Brinker, Alan Hurd., "Fundamentals of sol-gel dip-coating," *Journal de Physique III, EDP*, vol. 4, pp. 1231-1242, 1994.
- [59] Doyle, G.C. Randall and P.S., "Permeation-driven flow in poly(dimethylsiloxane) microfuidic devices.," *Proc. Natl. Acad. Sci.*, p. 102 : 10813, 2005.

- [60] Zhoua, Qian, "Study on the sedimentation self-assembly of colloidal SiO<sub>2</sub> particles under gravitational field," *Colloids and Surfaces*, vol. 253, p. 169–174, 2005.
- [61] Takeoka, Yukikazu, "Structural Colored Liquid Membrane without Angle Dependence," *ACS Appl. Mater. Interfaces*, vol. 5, pp. 982–986, 2009.
- [62] Gennady Shvets, Igor Tsukerman, *Plasmonics and Plasmonic Metamaterials: Analysis and Applications*, World scientific publishing Co. Pte. Ltd, 2012.
- [63] E. Verneuil, A. Buguin, and P. Silberzan., "Permeation-induced flows: Consequences for silicone-based microfluidics," *Europhys. Lett.*, no. 68 : 412, 2004.
- [64] II, Cleveland Eugene Rayford, "Optical Properties of Gold Nanospheres," *Nanoscope*, vol. 2, no. 1, 2005.
- [65] Mata, Okesolaa and, "Multicomponent self-assembly as a tool to harness new properties from peptides and proteins in material design," *Chemical Society Review*, no. 10, 2018.
- [66] Frédéric Doumenc, Jean-Baptiste Salmon and Béatrice Guerriery, "Modeling flow coating of colloidal dispersions in the evaporative regime: prediction of deposit thickness," *Langmuir*, pp. 1-19, 2016.
- [67] Linkhorst, John, "Microfluidic colloidal filtration," *Nature*, vol. 22376, 2016.
- [68] N. A. Fleck, R. M. McMeeking and T. Kraus, "Convective Assembly of a Particle Monolayer," *Langmuir*, vol. 31, p. 13655–13663, 2015.
- [69] Shangjr Gwo, Meng-Hsien Lin, Chieh-Lun He, Hung-Ying Chen and Toshiharu Teranishi, "Bottom-Up Assembly of Colloidal Gold and Silver Nanostructures for Designable Plasmonic Structures and Metamaterials," *Langmuir*, vol. 28, p. 8902–8908, 2012.
- [70] Yang, Wenguang & Yu, Haibo & Liang, Wenfeng & Wang, Yuechao & Liu, Lianqing, "Rapid Fabrication of Hydrogel Microstructures Using UV-Induced Projection Printing," *Micromachines*, vol. 6, pp. 1903-1913, 2015.
- [71] Chi-Mon Chen and Shu Yang, "Wrinkling instabilities in polymer films and their applications," *Polym Int*, vol. 61, p. 1041–1047, 2012.
- [72] Christopher A. Grabowski, Scott P. Fillery, Hilmar Koerner, Maxim Tchoul, Lawrence Drummy, Christopher W. Beier, Richard L. Brutchey, Michael F. Durstock & Richard A. Vaia, "Dielectric performance of high permittivity nanocomposites: impact of polystyrene grafting on BaTiO<sub>3</sub> and TiO<sub>2</sub>," *Nanocomposites*, vol. 2, no. 3, pp. 117-124, 2016.
- [73] Universities of Sussex and Bristol, "engineering.com," [Online]. Available: <https://www.engineering.com/DesignerEdge/DesignerEdgeArticles/ArticleID/14395/Shaping-Sound->

with-Metamaterials.aspx.

- [74] QianZhao et al., , "Mie resonance-based dielectric metamaterials," *materialstoday*, vol. 12, no. 12, pp. 60-69, December 2009.
- [75] N. R. F. Farzad Zangeneh, "Active times for acoustic metamaterials," *Reviews in Physics*, vol. 4, November 2019.

